

# Lawrence Berkeley National Laboratory

## Recent Work

### Title

HIGH TEMPERATURE CORROSION OF IRON-CHROMIUM ALLOYS IN SULFUR-CONTAINING ATMOSPHERES

### Permalink

<https://escholarship.org/uc/item/8ts1t1c9>

### Author

Choi, S.-H.

### Publication Date

1985-07-01



# Lawrence Berkeley Laboratory

UNIVERSITY OF CALIFORNIA

## Materials & Molecular Research Division

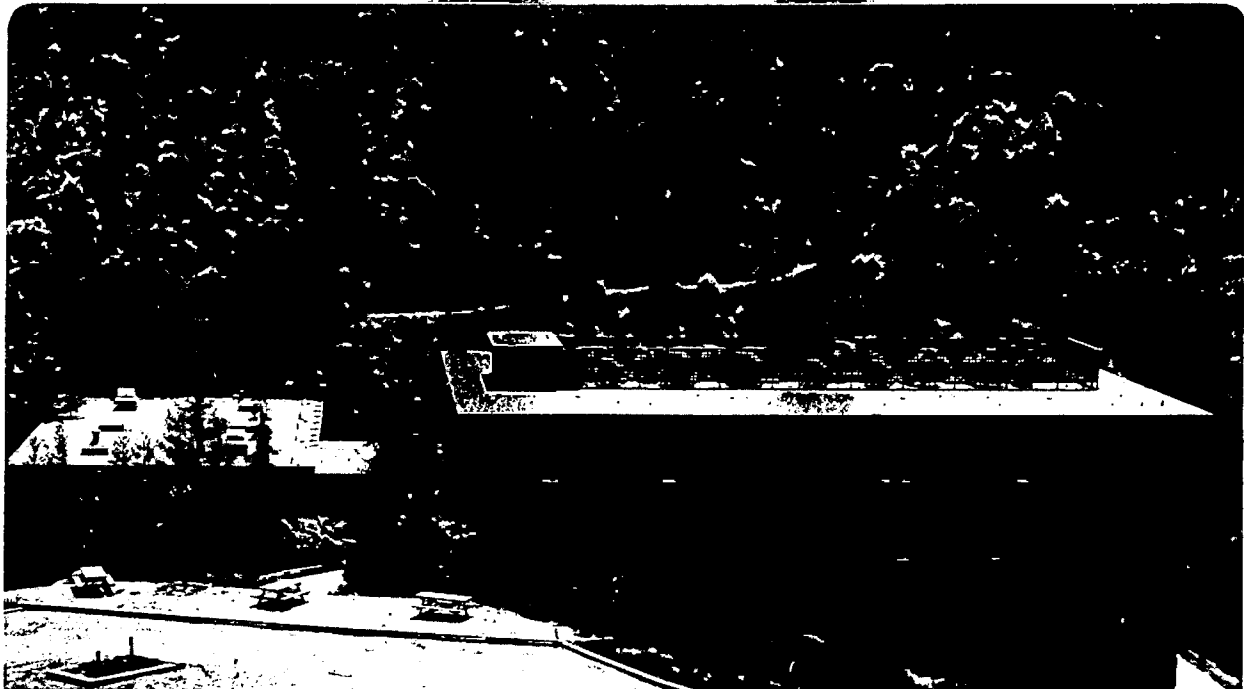
HIGH TEMPERATURE CORROSION OF IRON-CHROMIUM ALLOYS  
IN SULFUR-CONTAINING ATMOSPHERES

S.-H. Choi  
(Ph.D. Thesis)

July 1985

**TWO-WEEK LOAN COPY**

*This is a Library Circulating Copy  
which may be borrowed for two weeks.*



e.j.

LBL-20011  
e.j.

## **DISCLAIMER**

This document was prepared as an account of work sponsored by the United States Government. While this document is believed to contain correct information, neither the United States Government nor any agency thereof, nor the Regents of the University of California, nor any of their employees, makes any warranty, express or implied, or assumes any legal responsibility for the accuracy, completeness, or usefulness of any information, apparatus, product, or process disclosed, or represents that its use would not infringe privately owned rights. Reference herein to any specific commercial product, process, or service by its trade name, trademark, manufacturer, or otherwise, does not necessarily constitute or imply its endorsement, recommendation, or favoring by the United States Government or any agency thereof, or the Regents of the University of California. The views and opinions of authors expressed herein do not necessarily state or reflect those of the United States Government or any agency thereof or the Regents of the University of California.

**High Temperature Corrosion of Iron-Chromium Alloys  
In Sulfur-containing Atmospheres.**

**Soo-Han Choi**

**(Ph.D. Thesis)**

**Materials and Molecular Research Division,  
Lawrence Berkeley Laboratory and  
Department of Materials Science and Mineral Engineering,  
University of California,  
Berkeley, California 94720**

**July, 1985**

**This work was supported by the Director, Office of Energy Research, Office of Basic Energy Science, Materials Sciences Division of the U.S. Department of Energy under Contract Number DE-AC03-76SF00098.**

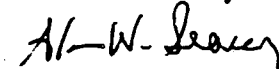
HIGH TEMPERATURE CORROSION OF IRON-CHROMIUM ALLOYS  
IN SULFUR-CONTAINING ATMOSPHERES

Soo-Han Choi

Materials and Molecular Research Division of Lawrence Berkeley Laboratory

Materials Science and Mineral Engineering

University of California



Alan W. Searcy, Chairman of committee

ABSTRACT

The corrosion behavior of iron-chromium alloys in sulfur-containing environments has been studied in controlled oxygen and sulfur partial pressures. The partial pressures were chosen to simulate the sulfur and oxygen activities in low oxygen partial pressure locations such as those in fluidized bed combustors. The high-temperature metal surfaces are covered with a calcium sulfate deposit. It was found that the calcium sulfate coupled with local low oxygen activities induces sulfidation/oxidation corrosion.

Although the sulfur activity in the atmosphere is important in determining whether or not sulfidation/oxidation corrosion took place, the development of the attack is much more sensitive to the actual  $SO_2$  partial pressure. Discrete internal Cr-rich sulfide particles were formed in the underlying alloy below an inner Cr-rich oxide layer. The development of internal sulfides is followed by in-situ internal oxidation of the sulfides, instability of the interface between the scale and alloy, leading to the incorporation of fragments of the more noble metallic constituents in the scale, and finally the destruction of the ability of the alloy to regenerate the protective oxide.

The reaction kinetics associated with this morphological development are of the breakaway type. Sulfidation/oxidation is a breakaway process. After breakaway, the metal oxidizes to form a non-protective characteristic two-layer oxide scale. It is shown that the breakaway can be correlated with the development of a "critical microstructure". The potential benefit of such an identification is that the prospect of breakaway can be identified by microstructural studies of specimens corroded for relatively short times, and may allow for quantitative modelling of breakaway.

## Table of Contents

|   |    |
|---|----|
| 1. Introduction .....   | 1  |
| 1.1. Basis of the present work .....  | 3  |
| 1.2. Scope of present work .....  | 4  |
| 2. Calcium sulfate induced corrosion behavior of<br>iron-chromium alloys .....  | 5  |
| 2.1. Introduction .....   | 5  |
| 2.2. Experimental .....   | 6  |
| 2.2.1. Specimen preparation .....   | 6  |
| 2.2.2. Corrosion experiments .....  | 7  |
| 2.2.3. Analysis of corrosion products .....                                     | 8  |
| 2.3. Results .....  | 9  |
| 2.3.1. Kinetics .....   | 9  |
| 2.3.2. Scale morphology and chemical composition .....                          | 10 |
| 2.4. Concluding remarks .....   | 12 |
| 3. Corrosion behavior of iron-chromium alloys in<br>mixed gas atmospheres ..... | 13 |
| 3.1. Introduction .....   | 13 |
| 3.2. Experimental .....   | 15 |
| 3.3. Results .....  | 17 |
| 3.3.1. Kinetics .....   | 17 |
| 3.3.2. Scale morphology and chemical composition .....                          | 18 |
| 3.3.3. Development of corrosion .....   | 24 |
| 3.3.4. Effect of temperature .....  | 26 |
| 3.4. Concluding remarks .....   | 27 |

|        |   |     |
|--------|---|-----|
| 4.     | Development of microstructure giving rise to<br>breakaway oxidation in mixed oxidant environments ..... | 29  |
| 4.1.   | Introduction .....  | 29  |
| 4.2.   | Transport of sulfur in the protective chromium oxide .....  | 35  |
| 4.2.1. | Experimental .....  | 35  |
| 4.2.2. | Results .....   | 36  |
| 4.3.   | Internal sulfidation .....  | 39  |
| 4.3.1. | Experimental .....  | 39  |
| 4.3.2. | Results .....   | 40  |
| 4.4.   | Oxidation of internal sulfides .....  | 42  |
| 4.4.1. | Experimental .....  | 42  |
| 4.4.2. | Results .....   | 42  |
| 4.5.   | Concluding remarks .....  | 45  |
| 5.     | Discussion .....  | 47  |
| 5.1.   | The corrosive environment within the bed of<br>a fluidized bed combustor .....                          | 47  |
| 5.2.   | Sulfidation/oxidation corrosion .....   | 48  |
| 5.3.   | The development of the critical microstructure .....  | 50  |
| 5.4.   | Breakaway oxidation .....   | 56  |
| 6.     | Conclusions .....   | 61  |
| 7.     | References .....  | 63  |
| 8.     | Appendices .....  | 66  |
|        | Acknowledgement .....   | 71  |
|        | Tables 1-21 .....   | 72  |
|        | Figure captions .....   | 95  |
|        | Figures 1-58 .....  | 104 |



## 1. Introduction

Resistance to high temperature corrosion is an absolute requirement for materials used in any corrosive environment at high temperatures. One of the methods for alloys to protect themselves is to form their own slowly-growing protective *scale*<sup>1</sup>; a continuous, adherent, compact oxide, to reduce their rate of reaction with the environment. A typical protective oxide scale for many high temperature alloys is  $Cr_2O_3$ . Evidently, the clear understanding of the nature and mechanism of breakdown of the protective chromium oxide scale is of vital significance to corrosion engineers both theoretically and practically. The breakdown mechanism of the  $Cr_2O_3$  scale by thermal and mechanical stresses in an oxidizing atmosphere has been studied by Whittle<sup>2-3</sup> et al.

However, in practical situations such as a fluidized bed combustor, alloys are exposed at high temperatures to atmospheres containing oxygen and sulfur. Sulfur is a critical impurity in almost all fossil fuel energy sources used in the chemical, metallurgical and power generation industries. Therefore, a basic understanding of simultaneous oxide and sulfide formation, or of sulfur penetration through a  $Cr_2O_3$  scale and into an alloy, is of technical importance, in order to develop alloy systems capable of resisting an ultimate corrosive degradation in these severe environments. Basically, the protective  $Cr_2O_3$  scale must be able to resist sulfur penetration. An example of current interest is the case of in-bed materials in fluidized bed combustors operating with relatively low excess air to maximize their efficiency. The environment within a fluidized bed combustor is markedly different from that in conventional coal combustion *systems*<sup>4-5</sup>. The bed operating temperature is usually in the range of 1023-1223 K. The oxygen partial pressures within the bed, measured using zirconia probes, fluctuates rapidly with minimum values which may be as low as  $10^{-12}$ - $10^{-14}$  atm<sup>6</sup> at a bed temperature of 1123 K. Limestone may be added as a sulfur dioxide sorbent to bed to

effectively reduce  $SO_2$  emission release from the fuel during combustion. When this is done, calcium sulfate deposits on the hotter metal surfaces of the in-bed heat exchangers and the uncooled support *structure*<sup>7</sup>. The calcium sulfate deposit on the hotter metal surfaces above approximately 823 K, is well-bonded and has a very low porosity.

It has been *shown*<sup>6-7</sup> that under these circumstances, alloys may undergo sulfidation/oxidation corrosion. The sulfidation/oxidation corrosion is of most importance in nickel or cobalt-base alloys. The sulfur is present as sulfides in the metal ahead of the oxidation front: the presence of those sulfides appears to prevent the alloy forming a continuous protective  $Cr_2O_3$  scale, and the alloy oxidizes rapidly. In many cases the sulfides formed are chromium-rich. Nickel-base alloys at temperature above 873 K are very rapidly attacked. High chromium iron-base alloys are relatively resistant, and alumina-forming high chromium Fe-Cr alloys such as Fe-25Cr-4Al-1Y(GE 2541) have excellent corrosion resistance. However, these latter alloys have relatively poor mechanical properties, and would be used only as coatings or claddings. For fluidized bed boilers, chromia-forming stainless steels such as Fe-10Ni-18Cr(type 304 or type 347) have been proposed as materials for high temperature tubing, and alloys such as Fe-25Cr-20Ni or Fe-25Cr are being evaluated for uncooled support members in fluidized bed *combustors*<sup>8-10</sup>.

However, other studies have shown that, under some circumstances, the calcium itself may be a factor in the corrosion process. *Perkins*<sup>11</sup> showed that the preformed  $Cr_2O_3$  layer could be destroyed due to the formation of a compound oxide  $CaO \cdot Cr_2O_3$  which is capable of forming a low melting point eutectic. *Akueze*<sup>12</sup> also demonstrated that the formation of a compound  $CaO \cdot Fe_2O_3$  phase which melts at relatively low temperatures was related to the rapid corrosion. However, both of these laboratory studies were at temperatures somewhat above those encountered in fluidized bed

combustors, and these phases have not been observed in any significant quantities in the corrosion products from actual *combustors*<sup>13</sup>.

Materials testing in a fluidized bed combustor is expensive and time consuming, and it is very difficult to determine the reaction mechanism. Thus, a simple laboratory method which may give comparable results is valuable. The early work to determine the reaction mechanism was done by Stringer and Whittle<sup>14</sup>, using  $\text{CaSO}_4$  powder and graphite in a crucible, and they reproduced the general form of the results in practice in this simple laboratory test. Later on, Stringer<sup>15</sup> et al continued the study using  $\text{CaSO}_4/\text{CaO}$  powder and the  $\text{CO}/\text{CO}_2$  gas mixture to define the oxygen partial pressure. But there was no independent measurement of the sulfur partial pressure.

#### 1.1. Basis of the present work

From the earlier studies described above, it appears that the reaction mechanism is as shown schematically in Figure 1. The unanswered questions relate to the way in which sulfidation can occur beneath the oxide scale, the breakdown of the protective oxide, and the possible role of calcium-containing species in the reaction. To answer these question, three distinct experimental programs were conducted;

- (1) The corrosion behavior of iron-chromium alloys in the presence of calcium sulfate.
- (2) Corrosion behavior of iron-chromium alloys in mixed gas atmospheres.
- (3) Development of microstructure giving rise to breakaway oxidation.

This laboratory scale research project was organized to pass through three phases in proper sequence, by following a postulate based on the previous experimental results, in order to determine the cause of the material degradation processes.

In the first phase, the corrosion type and the attack mode induced by calcium sulfate were examined in environments of controlled oxygen and sulfur partial pres-

tures connected through the  $CaSO_4/CaO/CaS$  equilibria, using  $CaSO_4/CaO$  powder mixture in a crucible and  $CO/CO_2$  gas mixtures to define the oxygen partial pressure.

In the second phase, the mechanism of sulfidation/oxidation corrosion and the breakaway process in the oxygen- and sulfur- containing atmospheres were examined, using a gas mixture rather than  $CaSO_4$  powder.  $CO-CO_2-SO_2$  gas mixtures at one atmosphere total pressure were used to study the specific corrosion phenomena in question. The  $CO-CO_2-SO_2$  gas mixtures have been used to produce the environments of controlled oxygen and sulfur partial pressures ( $P_{O_2}=10^{-14}-10^{-10}$ ,  $P_{S_2}=10^{-6.4}-10^{-4.0}$  atm), without using any Ca-containing species.

In the third phase, the development of microstructural features correlated with breakaway oxidation has been examined. The transport of sulfur-bearing species through the initially formed  $Cr_2O_3$  scale and in the underlying alloy, the mode of internal sulfidation in the alloy with different grain structure, and the oxidation of the internal sulfides i.e. the oxidation of two phase system has been examined. Finally, breakaway oxidation is discussed, correlating the growth kinetics and the microstructural changes.

## 1.2. Scope of present work

A basic understanding of the undesirable degradation of structural materials in fluidized bed combustors is of primary concern in this study. Material degradation involves the breakdown of the protective  $Cr_2O_3$  scale followed by the accelerated loss of metal. Iron-chromium alloys have been tested in a sulfur-bearing environment, attempting to simulate conditions which have been shown to be appropriate for in-bed locations in fluidized bed combustors.

The ferritic binary Fe-Cr alloys were chosen as the  $Cr_2O_3$ -formers in part because alloys of this type are candidates for in-bed components, and in part to avoid the complication of the presence of nickel in the austenitic stainless steel alloys. Iron

and chromium are the major components present in the stainless steels used in applications such as coal combustion. Another reason is that experience has shown alloys of this type to have the best resistance to attack in this environment as well as being more economical than alloys based on Ni or Co<sup>10</sup>.

In the present study, the morphological changes in the scale and the scale-alloy interface, the phase distribution in the reaction product, and the development of corrosion as well as the sulfur distribution in the scale and alloy have been observed, to obtain further metallographic evidence to establish the reaction characteristics more fully. As represented schematically in Figure 1, in addition to the compositional and microstructural changes occurring during the degradation of the protective chromium oxide scale on iron-chromium alloys, the growth kinetics of scales were also observed, by measuring the weight change, the scale thickness and the penetration depth of internal precipitates into the alloy to predict the progress of corrosion reaction. The penetration depth was used as the parameter representing the corrosion rate of alloy to interpret the local corrosion practically.

## **2. The corrosion behavior of iron-chromium alloys in the presence of calcium sulfate.**

### **2.1. Introduction**

The corrosion behavior of binary Fe-Cr alloys in the presence of calcium sulfate has been studied. The calcium sulfate deposited on the hotter metal surfaces in fluidized bed combustor could be decomposed locally at the low oxygen partial pressure atmospheres, and consequently significant sulfur partial pressures would be developed.

It has been *shown*<sup>6-7</sup> that sulfidation of some of the constituents of typical alloys is certainly possible. A simple laboratory crucible experiment to determine the reac-

tion mechanism was performed by Stringer and Whittle<sup>14</sup>, studying commercial alloys such as Incoloy 671 and stainless steel 316, in a  $CaSO_4$ /graphite powder mixture in a crucible. The role of the graphite was to keep the oxygen partial pressure low enough to decompose the  $CaSO_4$ . It was demonstrated that catastrophic sulfidation/oxidation attack of alloys can be induced in calcium sulfate at low enough oxygen activities, having some similarity to the attack observed in practice. Mark, Lin, Stevenson and Stringer<sup>15</sup> continued the study in the environments of  $CaSO_4$ /CaO powder mixtures and CO/ $CO_2$  gas mixtures using commercial alloys such as Type 304 stainless steel and Incoloy 800, and showed that sulfidation/oxidation type attack of the alloys, especially preferential penetration of sulfides along the grain boundaries, is responsible for the rapid corrosion. However, Akuezue<sup>12</sup> demonstrated that the formation of  $CaO \cdot Fe_2O_3$  compound with the spinel structure appeared to be associated with the rapid corrosion of alloys. Various mixtures of  $CaSO_4$ , CaO and graphite powders, and several materials such as pure Fe, Fe-Cr alloys, stainless steel, Incoloy etc were used in this laboratory study.

In the present investigation,  $CaSO_4$ /CaO powder mixture in crucibles and CO/ $CO_2$  gas mixtures to define the oxygen partial pressure were used. Binary Fe-Cr alloys chosen as  $Cr_2O_3$ -formers were tested. The corrosion type and attack mode on the scale and alloy were determined. This experiment was aimed at examining in some detail the phase distribution, scale morphologies and the development of corrosion, with emphasis on the distribution of sulfide which usually determines the overall rate of material degradation.

## 2.2. Experimental

### 2.2.1. Specimen preparation

The iron-chromium alloys were melted in an induction furnace under vacuum, and cast into 50 mm diameter ingots. The chemical compositions of the alloy ingots

are shown in Table 1, and also indicated on the Fe-Cr phase diagram shown in Figure 2. The cast ingots were homogenized at 1473 K for 24 hours. The alloys were then cut into test coupons measuring approximately 10 x 10 x 1 mm. The specimens were wet polished on SiC papers ranging from 180 grit to 600 grit under flowing water, and then washed with soap solution, distilled water and ethanol thoroughly. Prior to oxidation the dimensions of each test sample were measured using a micrometer. To determine the amount of oxidation which had occurred, the weight of each specimen was measured using an analytical torsion balance before and after each oxidation test.

### 2.2.2. Corrosion experiments.

The oxidation tests were conducted in a vertical tube furnace at a temperature of 1223 K for different time intervals up to 200 hours. The specimens were wholly immersed in the powder bed. The detailed experimental conditions are shown in Table 2. Mixtures of reagent grade  $CaSO_4$  and CaO were used. A gas mixture of CO-CO<sub>2</sub> having a specified oxygen activity was passed over the powder bed. The certified grade CO-CO<sub>2</sub> gas mixtures were supplied premixed by Matheson Gas Products Co. The oxygen partial pressure of  $10^{-11.2}$  atm was selected based on the measured values of CO-content in the gas in a fluidized bed using a zirconia probe<sup>6</sup>. The local  $P_{O_2}$  and  $P_{S_2}$  near the specimens inside the powder bed were calculated from the CO-CO<sub>2</sub> equilibria and the  $CaSO_4$ -CaO equilibria (see Appendix 8.1. for details). Figure 3 shows the schematic diagram of the experimental apparatus. The alumina crucible containing the specimens immersed completely in the powder mixture was introduced from the top of the furnace, supported by an alumina rod attached to the crucible with alumina pins. After purging the apparatus with dry argon gas, the premixed gas mixture was admitted to the reaction chamber, and then the crucible was lowered to the furnace hot zone. At the completion of an oxidation run, the specimens were raised to the cold part while flushing with argon.

### 2.2.3. Analysis of corrosion products

After oxidation, the bed material adhering to the external surface of the oxidized specimens was removed, by blasting off dust with compressed air and then by ultrasonic cleaning with ethanol solution. After weighing, each test specimen was cold-mounted in epoxy resin and sectioned for metallographic examination. The mounted specimens were wet ground mechanically in cross-section using SiC abrasive papers from 180 grit to 600 grit, and then ground finely on alumina papers using lapping oil. Fine details of the cross-section were resolved after fine polishing by using 1  $\mu\text{m}$  diamond paste under flowing Kerosene oil. The unetched cross-section morphologies of the scale and alloy were first examined using optical metallography. The typical thickness of the thin compact scale, which had a fairly uniform thickness over the alloy surface, and the maximum thickness of the thick two-layer scale which developed after the breakdown of the initial thin scale, were measured in the optical microscope. Several measurements were taken, and an average value calculated. The depth of penetration of the internal sulfide/oxide particles into the underlying alloy below the oxide layer was also measured, and the maximum measured value is reported. The maximum penetration is quoted even if it corresponded to a deep penetration along a grain boundary of the alloy. The established pattern used in this measurement is sketched in Figure 4. Following this examination of the unetched specimen, Vilella's reagent (5 ml HCl, 1 g picric acid, 100 ml ethanol) was used as an etchant to reveal the grain boundaries of the alloy. Alternatively, a 10% bromine-90% methanol solution was used to dissolve away the metal, revealing the morphology of the inner surface of scale at the scale-alloy interface without destroying the scale mechanically, irrespective of whether the scale was in direct contact with alloy or separated from it. The morphology of the scale and alloy in cross-section after etching by Vilella's reagent or by the bromine-methanol solution were examined in the optical microscope and then in



more detail using the Scanning Electron Microscope(SEM). In the latter case, the specimens were coated with conducting materials. Carbon was used mainly for coating the specimen surface, and sometimes aluminum and gold were also used. The morphologies of the outer surface, of the fractured section and of the inner surface of the stripped scale were also observed carefully using the SEM.

The chemical analysis of the corrosion products was carried out with an Energy Dispersive Analysis of X-rays(EDX) unit attached to the SEM. The system consisted of a Kevex Micro-X7000 analytical Spectrometer(energy dispersive, multichannel analyzer), a minicomputer, an integrated console, a dual floppy disk drive, and a printer terminal. The elements present were identified from the peak positions and analyzed quantitatively from the net intensity after subtracting the background. The spatial distribution of each element was determined mainly from the EDX elemental mapping of selected areas, and less frequently from line-scans, as well as from quantitative analysis of small selected areas.

The major crystallographic phases present in the corrosion products were identified using X-ray diffraction(XRD). A X-ray diffractometer using Cu- $K_{\alpha}$  radiation and Ni-filter step-scanned at a very slow speed of the order of  $1^{\circ}$ /min, on the external surface of oxidized samples and less frequently on the outer surface of the descaled alloy substrate. The phases present in the scale were identified from the characteristic peak positions and the corresponding intensities.

### 2.3. Results

Table 3 summarizes the overall experimental results in the crucible test.

#### 2.3.1. Kinetics

Figure 5 shows the weight gain of the Fe-20Cr alloy and the Fe-25Cr alloy as a function of exposure time in the low external  $P_{O_2}$  environment( $P_{O_2}=10^{-11.2}$  atm) in the

$\text{CaSO}_4/\text{CaO}$  mixture at 1223 K, illustrating the effect of the Cr-content in the alloy. At the early stage of oxidation until 100 hours, the Fe-20Cr alloy showed better oxidation resistance than the Fe-25Cr alloy. The weight change of the Fe-20Cr and the Fe-25Cr alloy after 100 hours oxidation was  $2.07 \text{ mg/cm}^2$  and  $3.10 \text{ mg/cm}^2$ , respectively. Breakaway kinetics was observed after an exposure of 150 hours in the Fe-20Cr alloy. In the Fe-25Cr alloy, the weight change increased slightly as the reaction time increased, still showing protective behavior.

### 2.3.2. Scale morphology and chemical composition.

As the chromium content in the alloy was increased, the scale formed on the alloy surface became thin, and also the chromium content in the scale was increased. The thin adherent  $\text{Cr}_2\text{O}_3$  scale was formed nearly uniformly on the alloy surface at the early stage of oxidation, from the 20 wt.% Cr in the alloy. In the  $\text{CaSO}_4$ -containing environments, no internal sulfidation was observed in the Fe-25Cr alloy. However, the Fe-20Cr alloy oxidized severely showing the characteristics of sulfidation, and the Fe-18Cr alloy oxidized more rapidly also showing sulfidation. The following discussion refers mainly to the Fe-20Cr alloy.

Figure 6 illustrates the breakaway process for the Fe-20Cr alloy in the  $\text{CaSO}_4/\text{CaO}$  mixture in the low external  $P_{\text{O}_2}$  environment ( $P_{\text{O}_2} = 10^{-11.2} \text{ atm}$ ) at 1223 K. Cross-section morphologies consistent with the kinetic curve shown in Figure 5 exhibit the breakaway process of the thin compact chromium oxide scale to a thick two-layer scale composed of an outer Fe-oxide layer and an inner mixed Fe-Cr oxide layer. The protective chromium oxide scale formed on the Fe-20Cr alloy had broken away after 150 hours oxidation. Figure 6a, 6b, 6c, and 6d show the compact chromium-rich oxide scale with a thickness of about  $3\text{-}4 \mu\text{m}$ ,  $6 \mu\text{m}$ ,  $9\text{-}10 \mu\text{m}$ , and  $14\text{-}15 \mu\text{m}$ , respectively. The scale had grown gradually as the exposure time increased. At the early stage of oxidation, the grain size of oxide was about  $1 \mu\text{m}$  in the thin adherent chromium oxide

scale with a thickness of about 5  $\mu\text{m}$ . The morphology of the scale at the scale-alloy interface was wavy. Figure 6e shows the two-layered scale, with a thickness of 50  $\mu\text{m}$ , which was composed of an outer iron-rich oxide layer and an inner Cr-rich oxide layer. After the thickening and the separation of the scale, the overall scale was composed of two layers; an outer thick iron-rich oxide layer, and an inner relatively thin Cr-rich oxide layer. The external scale contained little or no chromium, no sulfur, and apparently no calcium at least close to the interface. The inner chromium-rich oxide layer contained some iron-rich regions which appeared under the optical microscope to be metallic iron. Figure 6f shows the thick two-layered scale composed of an outer Fe-rich oxide layer and an inner mixed Fe-Cr oxide layer, which gradually spreads, destroying the remaining protective scale; part of the scale is still protected by the chromium oxide, part shows the thick scale. The inner mixed Fe-Cr oxide layer was more porous and non-compact. The innermost thin chromium-rich oxide layer with a thickness of approximately 5-10  $\mu\text{m}$  was formed near the scale-alloy interface.

In the metal, isolated particles rich in Cr and S but very low in Fe were detected. The maximum depth of the internal sulfidation zone containing Cr-rich sulfide particles below the inner chromium oxide layer was approximately 20-30  $\mu\text{m}$ . It is possible that oxides or oxysulfides might have been present in this zone, but in the absence of an oxygen-distribution determination it is not possible to be sure. However, the appearance of all the particles is consistent with their being CrS. Discrete internal chromium-rich sulfide particles were globular in shape and aligned to a constant depth in the alloy parallel to the scale-alloy interface. Oxide intrusion into the alloy matrix, containing some sulfur, and globular Cr-rich sulfide particles just below them were also observed. Figure 7 shows an SEM micrograph exhibiting the cross-section morphology of an Fe-20Cr alloy oxidized for 150 hours in the  $\text{CaSO}_4/\text{CaO}$  mixture in the low external  $P_{\text{O}_2}$  environment ( $P_{\text{O}_2} = 10^{-11.2}$  atm) at 1223 K. Figure 8 shows the sulfur

distribution through the thick two-layer scale. Sulfur was detected at the boundary region between an outer Fe-rich oxide and an inner Cr-rich oxide, and between an inner Cr-rich oxide and alloy. Sulfur was also randomly distributed in the Cr-rich region in the scale. The observation of Cr-rich sulfides within and just below the thick two-layer scale suggests that this internal attack may be correlated with the formation and growth of the thick scale. There was a strong tendency for the scale to spall off more easily in the sulfur-containing environment, indicating that sulfur may be closely related with the non-adherency and the premature breakaway of the  $Cr_2O_3$  scale.

A scale composed of an outer (Ca/Cr) oxide layer and an inner Cr-rich oxide layer was produced on the Fe-20Cr alloy surface locally, as shown in Figure 9. The (Ca/Cr) oxide formed on the external surface of the oxidized samples as a reaction product appears to be a mixture of CaO and  $Cr_2O_3$ , based on the EDX analysis results and on the CaO- $Cr_2O_3$  phase diagram shown in Figure 10. In all cases, the mixture of CaO and  $Cr_2O_3$  was uniformly distributed, not too thick, and did not reach the bare alloy surface, which was always well covered by the inner Cr-rich oxide layer. The CaO and  $Cr_2O_3$  oxide mixture was also formed on the external surface of the oxidized samples as a reaction product, with the iron oxide just above the thin Cr-rich oxide layer. The CaO and  $Fe_2O_3$  oxide mixture was not continuously distributed, and not deep enough to penetrate through the thin Cr-rich oxide layer, reaching the scale-alloy interface. No Ca-bearing species were detected at or below the scale-alloy interface.  $CaO \cdot Cr_2O_3$  or  $CaO \cdot Fe_2O_3$  single phase was not detected on the surface of the oxidized samples by XRD in any case, just a mixture was observed in the microscope. There was no evidence of compound oxide formation, either in the Ca-Fe-O or Ca-Cr-O system.

#### 2.4. Concluding remarks

The severe sulfidation/oxidation type attack induced by  $CaSO_4$  occurred locally, as shown in Figure 11, accompanying the breakaway of the protective chromium oxide scale on the iron-chromium alloy.

Iron-rich oxides, chromium-rich sulfides and  $Cr_2O_3$  developed as corrosion products. The reaction products at the external surface of scale on the iron-chromium alloys, such as a CaO and  $Cr_2O_3$  oxide mixture and a CaO and  $Fe_2O_3$  oxide mixture appear to be insignificant in controlling the overall corrosion mechanism. In the environment of a moderately low oxygen partial pressure and a relatively high sulfur partial pressure, Cr-rich sulfides were formed below and within the scale. The chromium content in the alloy was critical i.e. low chromium alloys such as Fe-15Cr and Fe-18Cr were more susceptible to sulfidation/oxidation type attack. A uniform band of discrete globular chromium sulfide particles below an inner thin chromium-rich oxide layer was the most common observation locally, which seems to be significant in the long-term oxidation.

The distribution of the internal Cr-rich sulfide particles seems to be critical, as well as the chromium depletion caused by the sulfur pick-up locally. Internal sulfidation of the metal below an inner thin chromium oxide could be a precursor to breakaway corrosion.

### **3. Corrosion behavior of iron-chromium alloys in mixed gas atmospheres.**

#### **3.1. Introduction**

The corrosion behavior of binary Fe-Cr alloys in mixed gas atmospheres has been studied. There is a need to determine the reaction mechanism of sulfidation/oxidation corrosion and the breakdown mechanism of protective chromium oxide scales in oxygen- and sulfur- containing atmospheres which simulate the corrosive environments

within the bed of a fluidized bed combustor. In this experiment, gas mixtures including  $SO_2$  were used, without using any Ca-containing species such as solid  $CaSO_4$  powder. In the gaseous environments, sulfur-containing species could be supplied continuously to the system i.e. the  $SO_2$  partial pressure in the environment is time-independent throughout the oxidation run. Direct and independent control of the oxygen and sulfur partial pressures was thus possible.

In oxidizing atmospheres without sulfur, *Whittle*<sup>2-3</sup> et al proposed that the chromium oxide scale formed on binary Fe-Cr alloys(16, 18, 23% Cr) would break down mechanically. *Birks*<sup>16</sup>, *Giggins*<sup>17</sup>, *Pettit*<sup>18</sup>, *Worrell*<sup>19</sup> et al studied the corrosion behavior of metals and alloys in  $SO_2$ -containing gas mixture environments. Most previous work using gas mixtures including  $SO_2$  have been done in relatively high oxygen partial pressures such as  $SO_2/Ar$ ,  $SO_2/O_2$ ,  $SO_2/CO_2$ ,  $SO_2/SO_3$ , and also usually large amounts of  $SO_2$  were used to make the experiment easier. Meanwhile, *Rahmel*<sup>20</sup> studied the corrosion behavior of Fe-20Cr alloy using  $H_2/H_2O/H_2S$  gas mixtures, in the very low oxygen partial pressure range. However, in a number of practical applications, environments which have a moderately low oxygen partial pressure and a relatively high sulfur partial pressure are of great importance.

The approach outlined here is to select experimental conditions which are intended to simulate a specific type of sulfidation/oxidation corrosion corresponding to that encountered in the fluidized bed combustor environment. The  $CO-CO_2-SO_2$  gas mixtures were chosen to produce oxygen and sulfur partial pressures in the ranges  $P_{O_2}=10^{-14}-10^{-10}$ ,  $P_{S_2}=10^{-6.4}-10^{-4.0}$  atm. Typically, the  $CO-CO_2-SO_2$  gaseous environments can be defined thermodynamically in terms of the oxygen and sulfur partial pressures, and the carbon activity. In these experiments, the carbon activity was very low; low enough not to form a carbide as a reaction product. In this report, consequently, the atmospheres are characterized only by their oxygen and sulfur pressures.

In the thermodynamic phase stability diagram of the Cr-O-S system, shown in Figure 12, the environments chosen in this study lie in the  $Cr_2O_3$  stability region just below the stability boundary between sulfide and oxide and also above the extrapolation of the stability boundary between sulfide and metal.

The effect of the sulfur activity, the  $SO_2$  partial pressure, and the Cr-content of the alloy (15, 18, 20, 25, 30% Cr) on the kinetics of the reaction, on the morphology of the reaction products, and on the development of the corrosion was studied. Emphasis was placed on the distribution of internal sulfides/oxides and the penetration of oxide intrusions in the alloy, as well as the regeneration of the external protective Cr-oxide scale. This experiment also concentrates on the critical factors which lead to the breakdown of the protective  $Cr_2O_3$  scale such as the microstructural changes in the  $Cr_2O_3$ -rich scale, the adhesion characteristics of the scale-alloy interface, and the formation of internal sulfides in the alloy.

### 3.2. Experimental

#### 3.2.1. Specimen preparation

Specimens were prepared using the same methods as for the previous studies (section 2.2.1.).

#### 3.2.2. Corrosion experiment

The oxidation tests were conducted in a vertical tube furnace for different time intervals up to 200 hours (mostly 100 hours) in the mixed gas environments. Figure 13 shows a schematic diagram of the experimental apparatus. Table 5 shows the experimental conditions.  $P_{O_2}$  and  $P_{S_2}$  were calculated from the CO-CO<sub>2</sub>-SO<sub>2</sub> equilibria (see Appendix 8.2. for details). The premixed CO-CO<sub>2</sub> and SO<sub>2</sub>-Ar gas mixtures were combined to form the required atmosphere, which then flowed into the reaction chamber. The certified premixed gases were supplied by Matheson Gas Products Co. Figure 14

shows the simplified stability diagram superimposed for the chromium-oxygen-sulfur system and the iron-oxygen-sulfur system at 1223 K and at 1123 K. The gas mixtures used in this experiment are indicated by the points on the stability diagram. The premixed  $CO-CO_2$  and  $SO_2$ -Ar gas mixtures flowed into the gas mixer filled with alumina granules, passing through each flowmeter already set up with the predetermined flow rate. After the completion of a continuous mixing, a preadjusted  $CO-CO_2-SO_2$ -Ar gas mixture passed through the long tube for gas equilibration. After purging the apparatus with dry argon gas, the fully equilibrated gas mixture was admitted to the system, and then the specimens were lowered from the top of the furnace to the furnace hot zone using a ceramic specimen holder. At the completion of an oxidation run, the specimens were raised to the cold part while flushing with argon.

### 3.2.3. Analysis of corrosion products

After oxidation, the corrosion products on the alloy surface were visually examined, noting such factors as the general appearance, colour, any evidence of spalling, general uniformity etc. After each oxidation run, specimens were weighed to determine the amount of corrosion products.

The observation of the surface and cross-section morphologies of the scale and alloy using optical metallography and scanning electron microscopy, and quantitative chemical analysis of the corrosion products using an EDX unit attached to the SEM were carried out using the same methods as described in the previous section 2.2.3. Fracture sections of the scale and alloy were prepared by breaking the oxidized specimens at liquid nitrogen temperature and examined in the SEM. Quantitative chemical analysis of the corrosion products and the depth profile of particular elements such as sulfur were performed using Auger Electron Spectrometry(AES).

The major crystallographic phases in the corrosion products were identified by using X-ray diffraction(XRD). A X-ray diffractometer using  $Cu-K_{\alpha}$  radiation and Ni-



filter step-scanned at a very slow speed, of the order of 1 sec/step, over  $0.1^\circ$   $2\theta$  interval, on the external surface of oxidized samples and less frequently on the inner surface of the stripped scale. The phases present in the scale were identified from the characteristic peak positions and the corresponding intensities. The lattice constants of the  $M_2O_3$ -type scale such as  $Cr_2O_3$  or  $(Cr,Fe)_2O_3$  solid solution were calculated from the measured  $2\theta$  value or interplanar spacing, step-scanning at a very slow speed of the order of 4 sec/step, over  $0.01^\circ$   $2\theta$  interval around each of the (110), (116), (300), (220) peak positions. The overall characterization methods for the corrosion products are summarized in Table 4.

### 3.3. Results

Table 6 summarizes the overall experimental results in the mixed gas atmospheres at 1223 K.

#### 3.3.1. Kinetics

The atmosphere with  $P_{O_2}=10^{-11.2}$ ,  $P_{S_2}=10^{-6}$  atm (environment number 3 in Table 5) produced no internal sulfidation in any of the alloys at 1223 K. Only minor traces of sulfur were detected in the scale on the Fe-15Cr alloy. The following discussion thus refers mainly to the remaining two sulfur partial pressures ( $P_{S_2}=10^{-4}$ , or  $10^{-5}$  atm) which are referred to as "high" and "low"  $P_{S_2}$ , respectively.

Figure 15 illustrates the effect of the Cr-content in the Fe-Cr alloys. Fe-20Cr and Fe-25Cr were oxidized slowly up to 200 hours, but the Fe-15Cr alloy oxidized very rapidly even in the low  $P_{S_2}$  atmosphere ( $P_{O_2}=10^{-11.2}$ ,  $P_{S_2}=10^{-5}$  atm). Figure 16 shows the weight change of the Fe-20Cr alloy as a function of exposure time in the two different  $P_{S_2}$  atmospheres at the same  $P_{O_2}$  ( $P_{O_2}=10^{-11.2}$  atm) at 1223 K. Breakaway kinetics were observed after an exposure time of 150 hours in the high  $P_{S_2}$  atmosphere. In the low  $P_{S_2}$  atmosphere, the weight change increased slightly as the reaction time

increased, still showing protective behavior. It is very difficult to compare the weight changes of the Fe-25Cr alloy because the scale formed on Fe-25Cr alloy spalled off more easily than that on Fe-20Cr alloy. Figure 17 shows the variation of the thickness of the typical protective scale of Fe-20Cr and Fe-25Cr as a function of exposure time in the four different atmospheres. In the high  $P_{S_2}$  atmosphere, the measured values of scale thickness were greater and more scattered than in the low  $P_{S_2}$  atmosphere. Near-parabolic kinetics were observed except in the high  $P_{S_2}$  atmosphere. Comparison of averaged scale thickness with weight gains indicated that oxide had not nearly spalled from outside these thinner scale regions. Figure 18 shows the maximum penetration depth of Fe-20Cr and Fe-25Cr as a function of exposure time in the two  $P_{S_2}$  atmospheres at the same  $P_{O_2}$ . For the high  $P_{S_2}$  atmosphere, the maximum penetration depth of the internal Cr-rich sulfide/oxide particles into the underlying alloy increased with time, exhibiting a similar trend to the scale thickness. For the low  $P_{S_2}$  atmosphere, the internal penetration was negligible, although internal sulfides could be detected immediately beneath the interface. Comparison of Figures 16 and 17 indicates that although a large part of the increased weight gain after 100 hours is attributable to the thick two-layer scale, both the remaining protective scale and the penetration exhibited increasing rates of growth.

### 3.3.2. Scale morphology and chemical composition

#### Fe-15Cr

A continuous protective chromium oxide layer was not formed on the Fe-15Cr alloy in any case, irrespective of the sulfur activity in the environment. In the high  $P_{S_2}$  environment ( $P_{O_2}=10^{-11.2}$ ,  $P_{S_2}=10^{-4}$  atm), a thick two-layer scale composed of an outer Fe-oxide layer and an inner mixed Fe-Cr oxide layer was formed on the alloy surface; the two layers had approximately equal thickness. In the inner part of the

inner mixed Fe-Cr oxide layer and also in the vicinity of the scale-alloy interface, sulfur was detected in Cr-rich regions. In the low  $P_{S_2}$  environment ( $P_{O_2}=10^{-11.2}$ ,  $P_{S_2}=10^{-5}$  atm), a thick two-layer scale was also formed on the alloy surface, but the thickness of each layer was less than that in the high  $P_{S_2}$  environment for the same oxidation period. For example, after 25 hours oxidation, the thickness of each of the layers was about 150  $\mu\text{m}$  in the low  $P_{S_2}$  environment, whereas the thickness of each layer was about 250  $\mu\text{m}$  in the high  $P_{S_2}$  environment. Even in the low  $P_{S_2}$  environment, sulfur was also detected in the Cr-rich region, at and near the scale-alloy interface; but the extent of sulfidation was less in the low  $P_{S_2}$  environment. The main differences between the high  $P_{S_2}$  environment and the low  $P_{S_2}$  environment were thus the thickness of the oxide layers, and the extent of sulfidation at and near the scale-alloy interface. Figure 19 shows optical micrographs of the cross-section morphology of the Fe-15Cr alloy oxidized for 25 hours in the two different  $P_{S_2}$  atmosphere ( $P_{S_2}=10^{-4}$ ,  $10^{-5}$  atm) at the same  $P_{O_2}$  ( $P_{O_2}=10^{-11.2}$  atm) at 1223 K.

#### Fe-18Cr

In the low  $P_{S_2}$  atmosphere ( $P_{S_2}=10^{-5}$  atm), the Cr-oxide scale was uniformly distributed on the alloy surface after the specimens were oxidized for 100 hours. After 200 hours oxidation, the metal was completely consumed. Internal sulfide/oxide particles do not appear to have increased in population with the increasing oxidation time. In the high  $P_{S_2}$  atmosphere ( $P_{S_2}=10^{-4}$  atm), nearly all of the metal was consumed after the specimens were oxidized for 100 hours. The remaining  $\text{Cr}_2\text{O}_3$  scale was 6-10  $\mu\text{m}$  thick.

#### Fe-20Cr

Figure 20 illustrates the breakaway process for the Fe-20Cr alloy in the high  $P_{S_2}$  atmosphere ( $P_{O_2}=10^{-11.2}$ ,  $P_{S_2}=10^{-4}$  atm) at 1223 K. The scale formed on Fe-20Cr had

broken away after 100 hours oxidation. Internal Cr-rich sulfide/oxide particles were observed in the underlying alloy below an inner Cr-rich oxide layer. Internal sulfide/oxide stringers penetrated into the alloy perpendicular to the scale-alloy interface. As the exposure time increased, the sulfide/oxide particles penetrated more deeply into the base alloy. Meanwhile, the scale was gradually separating into two layers; an outer Fe-oxide and an inner Cr-rich oxide, more and more obviously. Finally, a two-layer scale composed of an outer layer of iron oxide and an inner layer containing iron and chromium oxides, with sulfur present in the innermost part was formed.

Figure 21 shows the SEM topography and the optical cross-section morphology of the scale produced on Fe-20Cr alloy oxidized for 50 hours in the high  $P_{S_2}$  atmosphere at 1223 K. Nodules composed of an outer Fe-oxide and an inner Cr-rich oxide layer were observed. Internal sulfide particles were formed, and the internal sulfidation front advanced deep into the underlying alloy as the nodule thickness increased. Figure 22 shows the SEM micrograph exhibiting the cross-section morphology of an Fe-20Cr alloy oxidized for 100 hours in the high  $P_{S_2}$  atmosphere at 1223 K. An outer Fe-oxide layer was formed above an inner Cr-rich oxide layer. Coarse Cr-rich sulfide particles were distributed in the underlying alloy to a depth of 20-30  $\mu\text{m}$  below the metal/oxide interface. Sulfur was also detected at the part of the inner Cr-rich oxide layer.

Figure 23 shows SEM micrographs of the scale-alloy interface, revealed by the deep etching technique, of the Fe-20Cr alloy oxidized for 100 hours in the two different  $P_{S_2}$  atmospheres ( $P_{S_2}=10^{-4}$ ,  $10^{-5}$  atm) at the same  $P_{O_2}$  ( $P_{O_2}=10^{-11.2}$  atm) at 1223 K. In the specimen exposed to the high  $P_{S_2}$  atmosphere, the oxide intrusions shown in Figure 23a were found, by means of the EDX technique, to contain sulfur. The scale itself was porous. The pores may have originated in one of several ways: by dissolving away isolated base-metal islands in the scale in the bromine-methanol solution; as a result of

pull-out during the polishing of the specimen; perhaps as a real feature of the oxidation. In contrast, in the low  $P_{S_2}$  atmosphere, the scale-alloy interface was smooth. The scale has no visible macropores and there was no internal sulfidation of the base alloy.

For Fe-20Cr specimens oxidized in the low and very low  $P_{S_2}$  atmospheres ( $P_{S_2}=10^{-5}$ ,  $10^{-6}$  atm), X-ray diffraction detected only  $Cr_2O_3$  in the scale; small amounts of iron were detected in the  $Cr_2O_3$  scale by EDX. Rapid corrosion did not occur in the low  $P_{S_2}$  atmospheres. The  $Cr_2O_3$  scale was uniformly distributed on the alloy surface. Some Cr-rich sulfide particles were detected, apparently within grooves present at the scale-alloy interface in the very low  $P_{S_2}$  environment. The region which seems to connect the scale and alloy was very porous. Figure 24 shows the SEM topography of the descaled Fe-20Cr alloy substrate oxidized for 200 hours in the very low  $P_{S_2}$  environment ( $P_{O_2}=10^{-11.2}$ ,  $P_{S_2}=10^{-6}$  atm) at 1223 K. No sulfur was detected in the scale and alloy. Cr-rich sulfide particles formed probably by the molecular penetration of  $SO_2$  gas through the scale.

Internal sulfidation was not observed even in the high  $P_{S_2}$  atmosphere ( $P_{S_2}=10^{-4}$  atm) at the lower  $P_{O_2}$  ( $P_{O_2}=10^{-12.0}$  atm) at 1223 K up to 200 hours, if the partial pressure of  $SO_2$  is very low. Only slow oxidation was observed. In other words, in the low  $P_{SO_2}$  gas atmosphere ( $P_{SO_2}=0.004$ ,  $P_{O_2}=10^{-12.0}$ ,  $P_{S_2}=10^{-4}$  atm), internal sulfidation did not occur even in the high  $P_{S_2}$  atmosphere. The partial pressure of  $SO_2$  in the environment apparently played a more decisive role in the occurrence of the internal sulfidation on the Fe-20Cr alloy than the partial pressures of oxygen or sulfur.

#### Fe-25Cr

In the high  $P_{S_2}$  atmosphere, the Fe-25Cr alloy was corroded more severely than the Fe-20Cr alloy in the early stages of the oxidation, forming internal Cr-rich

sulfide/oxide particles more deeply in the base alloy. But the internal sulfidation front advanced very slowly into the alloy as the reaction time increased. Figure 25 shows an SEM micrograph of the cross-section of an Fe-25Cr alloy oxidized for 25 hours in the high  $P_{S_2}$  atmosphere ( $P_{O_2}=10^{-11.2}$ ,  $P_{S_2}=10^{-4}$  atm) at 1223 K. An outer Fe-oxide layer was formed above an inner Cr-oxide layer. Cr-rich sulfide particles were distributed in the underlying alloy to a depth of 20-25  $\mu\text{m}$  below the metal-oxide interface. Sulfur was present throughout the inner Cr-rich oxide layer; however, the concentration appeared to be significantly greater immediately adjacent to the metal/oxide interface. Figure 26a and 26b show an optical micrograph and an SEM micrograph of the cross-section of an Fe-25Cr alloy oxidized for 50 hours in the high  $P_{S_2}$  atmosphere. A band of Cr-rich sulfide particles was formed below the inner Cr-rich oxide layer to a depth of about 50-80  $\mu\text{m}$ . Local Cr-rich sulfide/oxide intrusions penetrated more deeply into the alloy up to 120  $\mu\text{m}$ , along the badly-bonded grain boundaries which appear to be chromium-depleted regions or to be precracked by stresses created during specimen preparation. In the Fe-25Cr alloy specimen, etched with Vilella's reagent, coarse internal Cr-rich sulfide particles were observed in the vicinity of the boundary between the unaffected base alloy and the affected zone of the underlying alloy, as shown in Figure 27. The smaller particles in the affected zone were located within a depth of 50  $\mu\text{m}$  below the Cr-rich oxide layer. The affected zone of the underlying alloy was created probably by the Cr-depletion. There was no tendency for the internal Cr-rich sulfide/oxide particle front to advance preferentially along the grain boundaries of the alloy under the adherent scale.

In the very low  $P_{S_2}$  atmosphere ( $P_{O_2}=10^{-11.2}$ ,  $P_{S_2}=10^{-6}$  atm) small amounts of sulfur were detected locally at the inner surface of the detached Cr-oxide scale produced on the Fe-25Cr alloy. Figure 28 shows the underview of the scale produced on an Fe-25Cr alloy oxidized for 100 hours in the very low  $P_{S_2}$  atmosphere at 1223 K. No

sulfur was detected in the scale or the alloy on the cross-sectioned specimens. This observation is also indirect experimental evidence that the sulfur-containing species such as  $SO_2$  were transported through short-circuit diffusion paths in the scale by molecular penetration.

Figure 29b shows SEM fractography of the scale formed on an Fe-25Cr alloy oxidized for 150 hours in the high  $P_{S_2}$  atmosphere ( $P_{SO_2}=0.026$ ,  $P_{O_2}=10^{-11.2}$ ,  $P_{S_2}=10^{-4}$  atm), and Figure 29a shows the scale on the same alloy oxidized for 200 hours in the low  $P_{SO_2}$  atmosphere ( $P_{SO_2}=0.004$ ,  $P_{O_2}=10^{-12.0}$ ,  $P_{S_2}=10^{-4}$  atm) at 1223 K. In the high  $P_{S_2}$  atmosphere, the scale was composed of an outer columnar Fe-oxide layer and an inner porous Cr-rich oxide layer. The chromium sulfide was developed beneath and within the inner Cr-rich oxide layer, which appears to be related with the breakaway kinetics. In contrast, in the low  $P_{SO_2}$  atmosphere a uniform fine-grained compact Cr-oxide scale was formed, which appears to be related to the parabolic kinetics, even though the sulfur partial pressure was the same ( $P_{S_2}=10^{-4}$  atm).

#### Fe-30Cr

In the low  $P_{S_2}$  atmosphere ( $P_{S_2}=10^{-5}$  atm), the Cr-oxide scale was uniformly formed on the Fe-30Cr alloy oxidized for 200 hours at 1223 K. In the high  $P_{S_2}$  atmosphere ( $P_{S_2}=10^{-4}$  atm), internal Cr-rich sulfide/oxide particles were observed in the underlying alloy below the Cr-rich oxide layer to a depth of about 10-16  $\mu\text{m}$ , after the specimens were oxidized for 50 hours at 1223 K. Figure 30 is an optical micrograph of the cross-section of an Fe-30Cr alloy oxidized for 50 hours in the high  $P_{S_2}$  atmosphere.

#### Scale-surfaces

Figure 31 shows the SEM topography of the scale produced on an Fe-20Cr alloy and an Fe-25Cr alloy oxidized for 100 hours, respectively, in the three different  $P_{S_2}$

atmospheres ( $P_{S_2} = 10^{-4}, 10^{-5}, 10^{-6}$  atm) at the same  $P_{O_2}$  atmosphere ( $P_{O_2} = 10^{-11.2}$  atm) at 1223 K. In the high  $P_{S_2}$  atmosphere ( $P_{S_2} = 10^{-4}$  atm), the Fe-oxide which grew outward rapidly was distributed randomly on the upper part of the scale as an outer layer. Figure 32 shows the relation of the weight percentage ratio of Fe and Cr contents detected at the external surface of the scales with the thickness of scale formed in the two different  $P_{S_2}$  atmospheres ( $P_{S_2} = 10^{-4}, 10^{-5}$  atm) at the same  $P_{O_2}$  ( $P_{O_2} = 10^{-11.2}$  atm). The (Fe/Cr) ratio was calculated from the EDX data. The measured values of (Fe/Cr) ratios in the thick scale were more scattered than in the thin scale. The (Fe/Cr) ratio in the high  $P_{S_2}$  atmosphere was higher than that in the low  $P_{S_2}$  atmosphere irrespective of the scale thickness i.e. more iron was dissolved in the Cr-oxide scale in the high  $P_{S_2}$  atmosphere.

### 3.3.3. Development of the corrosion of the higher chromium-containing alloys.

The  $Cr_2O_3$  scale formed on the two higher chromium-containing alloys was nearly uniformly distributed on the alloy surface, and spalled off locally on cooling. When the specimens were slowly cooled after the oxidation run, there was a tendency for the initial, thin  $Cr_2O_3$  scale formed on Fe-25Cr alloy to spall off more easily than that on the Fe-20Cr alloy, the difference in adhesion increasing as the exposure time increased i.e. as the scale thickness increased. The tendency to spall increased with increasing Cr-content. Figure 33 compares the spalling tendency of Fe-20Cr and Fe-25Cr alloy in the three different  $P_{S_2}$  atmospheres ( $P_{S_2} = 10^{-4}, 10^{-5}, 10^{-6}$  atm) at the same  $P_{O_2}$  atmosphere ( $P_{O_2} = 10^{-11.2}$  atm). Although part of the scale formed on the Fe-25Cr alloy frequently spalled explosively on cooling as a spray of finely shattered particles, much of the specimen surface was still covered with a thin adherent Cr-oxide scale. In other words, as the extent of scale spalling increased, although the alloy exhibited severe internal corrosion and developed an outer Fe-oxide above an inner Cr-rich oxide



layer, the overall oxidation rate of the Fe-25Cr alloy did not accelerate greatly. However, although Fe-20Cr alloy showed good protective behavior at the early stage of oxidation, with the adherent scale resisting spalling to a greater extent, when the initial scale was broken down locally, the alloy corroded rapidly, forming a thick two-layer scale composed of an outer Fe-oxide layer and an inner mixed Fe-Cr oxide layer. Then the two-layer scale grew laterally, destroying the neighboring Cr-oxide scale.

Figure 34 shows SEM fractography of the scale formed on Fe-25Cr alloy oxidized for 200 hours in the low  $P_{SO_2}$  atmosphere ( $P_{SO_2}=0.004$ ,  $P_{O_2}=10^{-12.0}$ ,  $P_{S_2}=10^{-4}$  atm). The sulfur-containing intrusions below the Cr-rich oxide scale appear to be responsible for the spalling of scale. The chromium sulfide agglomerates which look like black dots in the low magnification micrograph were observed locally on the external surface of the descaled substrate of Fe-25Cr alloy specimen in the high  $P_{S_2}$  atmosphere, as shown in Figure 35. These sulfide agglomerates probably formed below the Cr-rich oxide before the spalling-off of the scale or formed on the descaled alloy substrate after the spalling-off. Judging from the viewpoint of thermodynamic stability, CrS is thermodynamically stable below the  $Cr_2O_3$  scale.

Table 7 compares the scaling characteristics of Fe-20Cr and Fe-25Cr alloys in the high  $P_{S_2}$  atmosphere ( $P_{O_2}=10^{-11.2}$ ,  $P_{S_2}=10^{-4}$  atm), describing the sulfidation/oxidation type corrosive attack. Table 8 compares the extent of the corrosive attack of the Fe-20Cr alloy and of the Fe-25Cr alloy in the high  $P_{S_2}$  atmosphere, attempting to relate the extent of corrosion with the scale thickness and the penetration depth. The relative thickness of the outer Fe-oxide layer appeared to vary with the extent of internal oxidation. Table 9 shows that when the sulfur activity in the environment ( $P_{S_2}=10^{-4}$  atm) was high enough to sulfidize the alloy, the  $Cr_2O_3$  scale had already ceased to be protective when the thickness was only 7-15  $\mu\text{m}$ . However, when the sulfur activity was low ( $P_{S_2}=10^{-5}$  atm), the  $Cr_2O_3$  scale remained protective even at a thickness of

12-14  $\mu\text{m}$ . In other words, it is possible that the critical thickness of  $\text{Cr}_2\text{O}_3$  scale to remain protective decreases as the sulfur activity in the environment increases. The type and the mode of corrosive attack in the mixed gas environments containing both oxygen and sulfur is summarized in Table 10 and Table 11. In the high  $P_{\text{S}_2}$  and high  $P_{\text{SO}_2}$  atmosphere ( $P_{\text{S}_2}=10^{-4}$ ,  $P_{\text{SO}_2}=0.026$  atm), internal sulfidation was observed in the higher Cr-containing Fe-Cr alloys (20, 25, 30% Cr). If  $P_{\text{SO}_2}$  is high ( $P_{\text{SO}_2}=0.026$  atm), internal sulfidation was still observed below the thin two-layer scale in the Fe-25Cr alloy even in the very low  $P_{\text{S}_2}$  atmosphere ( $P_{\text{S}_2}=10^{-6.4}$  atm). When  $P_{\text{SO}_2}$  is below 0.008 atm, internal sulfidation was not observed in the Fe-25Cr alloy irrespective of  $P_{\text{S}_2}$  ( $P_{\text{S}_2}=10^{-6}$ - $10^{-4}$  atm). In the Fe-20Cr alloy, internal sulfidation was barely observed below the thick two-layer scale in the low  $P_{\text{SO}_2}$  atmosphere ( $P_{\text{SO}_2}=0.008$ - $0.004$  atm), but the attack was not severe. The extent of sulfidation/oxidation corrosion decreased as  $P_{\text{SO}_2}$  decreased. In the very low  $P_{\text{S}_2}$  ( $P_{\text{S}_2}=10^{-6}$  atm) and very low  $P_{\text{SO}_2}$  ( $P_{\text{SO}_2}=0.002$  atm) atmosphere, internal sulfidation was not observed in the Fe-20Cr alloy. For a fixed sulfur partial pressure of  $10^{-4}$  atm, internal sulfidation was observed for  $\text{SO}_2$  partial pressure above 0.004 atm in the case of the Fe-20Cr alloy, and at 0.026 atm in the Fe-25Cr alloy. The  $\text{SO}_2$  partial pressure appears to be critical factor in determining the corrosion type. The extent of the corrosion depends more decisively on  $P_{\text{SO}_2}$  than on  $P_{\text{S}_2}$ . As the chromium content in the Fe-Cr alloys increased, the sulfidation/oxidation corrosion was retarded.

#### 3.3.4. Effect of temperature

A limited number of tests were conducted at 1123 K to give an indication of the effect of temperature. Table 12 shows the experimental results. Comparison of the corrosion in environments numbers 1 and 6 indicates that at the same  $P_{\text{SO}_2}$ , the Cr-oxide scale grew on any of the alloys more slowly at 1123 K than at 1223 K. The

internal sulfide/oxide front penetrated slightly deeper at 1223 K than at 1123 K. Comparison of environments numbers 5 and 6 indicates that when the volume fractions in the gas mixture are the same at the two different temperatures, the general scaling characteristics were similar; such as the formation of two-layer scale consisting of an outer Fe-oxide and an inner Cr-rich oxide, and the internal sulfidation in the underlying alloy. However, the extent of corrosion was more severe at 1223 K than at 1123 K. In the relatively low  $P_{S_2}$  atmosphere ( $P_{O_2}=10^{-12.2}$ ,  $P_{S_2}=10^{-5.7}$  atm) at 1123 K, no internal sulfidation was observed and only a  $Cr_2O_3$  scale was uniformly distributed on the surface of any alloys.

#### 3.4. Concluding remarks

The formation of internal Cr-rich sulfide/oxide particles in the underlying alloy below an inner Cr-rich oxide layer was a common observation for the relatively high sulfur partial pressure atmospheres. Figure 36 is a schematic representation of the development of the corrosion.

The development of internal sulfides leads to internal oxidation, fragmentation of the more noble metal in the scale, instability of the interface between the scale and alloy, and finally the inability of the alloy to regenerate protective oxide. The activity of sulfur plays an important role in determining whether sulfidation/oxidation corrosion occurs or not. However, the partial pressure of  $SO_2$ , rather than the sulfur activity, appears to be the more decisive factor in the development of the sulfidation/oxidation corrosion. The Cr-content in iron-chromium alloys was also important. The Fe-20Cr alloy exhibited good resistance to spalling, but after local failure of the initial  $Cr_2O_3$  scale, the alloy corroded rapidly forming a thick two-layer scale. Meanwhile, although the  $Cr_2O_3$  scale formed on the Fe-25Cr alloy spalled off easily, the overall oxidation rate of the alloy did not accelerate greatly. As the Cr-content in Fe-Cr alloys increased, the sulfidation/oxidation corrosion was retarded.

The extent of corrosion was more severe at 1223 K than at 1123 K.

The sulfidation/oxidation corrosion is a breakaway process. After breakaway, the metal oxidized to form non-protective two-layer scales composed of an outer Fe-oxide and an inner Cr-rich oxide. The deleterious effect of sulfur is related to its developing a microstructure which prevents the maintenance and the reformation of a protective external scale. The critical microstructure developed by the formation of the internal sulfides/oxides in the underlying alloy could cause the breakaway oxidation.

The formation of the globular internal Cr-rich sulfides in the underlying alloy below an inner Cr-rich oxide layer and a characteristic two-layer scale composed of an outer Fe-oxide and an inner Cr-rich oxide, were common observations both in the crucible test and the test in the simulated mixed gas atmosphere. These observations indicate that the sulfur-containing species such as  $SO_2$  was evolved from the  $CaSO_4/CaO$  equilibria in the low oxygen partial pressure atmospheres created by the  $CO/CO_2$  gas mixture. The sulfur activity in the low oxygen partial pressure atmosphere would be increased enough to sulfidize the alloy locally, along the  $CaSO_4/CaO$  equilibrium line as a function of oxygen partial pressure. The maximum penetration depth of internal sulfides, representing the corrosion rate of material at given environmental conditions, saturated to a constant depth below the inner Cr-rich oxide layer as the oxidation time increased. In the mixed gas environments, the maximum penetration depth was 30-40  $\mu m$  in the Fe-25Cr alloy, and 40-50  $\mu m$  in the Fe-20Cr alloy in the high  $P_{S_2}$  atmosphere. In the crucible test, the maximum penetration depth was negligible in the Fe-25Cr alloy, and 20-30  $\mu m$  in the Fe-20Cr alloy, in the theoretically postulated high  $P_{S_2}$  atmosphere connected through the low external  $P_{O_2}$  atmosphere and the  $CaSO_4/CaO$  equilibria. The sulfidation/oxidation corrosive attack in the mixed gas environments was more severe than that in crucible tests. The corrosion

process is not directly comparable because the evolution of  $SO_2$  gas in crucible tests was  $CaSO_4$  decomposition reaction dependent and time-limited in this laboratory experiment, and because of a continuous supply of sulfur-bearing species even after breakdown of a protective  $Cr_2O_3$  scale in the mixed gas atmospheres. A series of specially designed experiments are needed to answer the cause of the sulfidation/oxidation corrosive attack in various sulfur-containing environments more clearly.

#### **4. Development of microstructure giving rise to breakaway oxidation.**

##### **4.1. Introduction**

It is postulated that the breakdown of the protective oxide in sulfidation/oxidation corrosion is associated with the development of a "critical microstructure". This critical microstructure is sketched in Figure 37, and it arises from the break-up of the planar interface by the chromium-rich oxide intrusion, which results from the oxidation in-situ of the internal chromium sulfides, and from the consequent depletion of the surface layers of the metal in chromium, inhibiting the reformation of a protective external  $Cr_2O_3$  scale if the initial oxide fails or is otherwise removed. The usefulness of this concept is that the evolution of such a microstructure can be detected at an early stage, well before the onset of breakaway, allowing the prediction of probable breakaway behavior from relatively short-term testing.

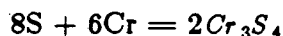
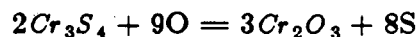
##### **4.1.1. Previous investigation**

Few investigations have provided information leading toward a detailed understanding of the transport of sulfur in chromium oxide. *Seybolt*<sup>21</sup>, using hot pressed  $Cr_2O_3$  powder samples and  $H_2/H_2S$  mixed gas environments, estimated the diffusion coefficient of sulfur in  $Cr_2O_3$  to be about  $10^{-10}$   $cm^2/sec$  at 1273 K. There has been significantly greater efforts aimed at the investigation of the transport of other species

through  $Cr_2O_3$ . *Hagel*<sup>22</sup> studied the diffusion of oxygen in single crystal  $Cr_2O_3$ , and the diffusion coefficient of oxygen was slower by several orders of magnitude than the diffusion coefficient of sulfur measured by Seybolt. Many studies of chromium diffusion in chromium oxide have been reported, and the data have been published by *Kofstad*<sup>23</sup> and by *Atkinson*<sup>24</sup>. *Kofstad* claimed that chromium vacancies or interstitials diffuse through the bulk oxide. However, *Atkinson* demonstrated that chromium diffuses through short-circuit diffusion paths such as grain boundaries in the oxide.

Internal oxidation of alloys has been an active topic of research for many years. *Wagner*<sup>25</sup> developed the first quantitative theory for the process, and for the transition from internal to external oxidation. *Rapp*<sup>26</sup> reviewed the early literature and conducted a number of experiments, particularly in the Ag-In system, confirming the major features of the Wagner model. Essentially, internal oxidation involves a competition between the diffusion of oxygen into the alloy and the diffusion of the oxide-forming element out. *Hossain*<sup>27</sup> studied the effect of cold-working in the oxidation of Fe-Cr alloys. The effect of this is to produce, at the oxidation temperature, a fine-grained recrystallized structure. Chromium outward diffusion via metal grain boundary short-circuit paths is enhanced, and the effect is to encourage the formation of an external oxide and thus to improve the oxidation resistance of alloys having marginal chromium contents. The diffusion coefficients of sulfur in Fe-Cr alloys (18, 26, 34% Cr) were determined by *Fillastré*<sup>28</sup> in the temperature range 1123-1473 K. The solubility of sulfur in Fe-Cr alloys of various compositions was reported by *Oudar*<sup>29</sup> for the temperature range of 1273-1473 K. *Risoe*<sup>30</sup> studied the internal sulfidation of dilute Fe-based alloys with alloying elements such as Cr, Al in  $H_2O-H_2S$  mixed-gas atmospheres. From measurements of the penetration depth of internal sulfidation in the alloy, the diffusion coefficient of sulfur in Fe-Cr alloys was calculated to be about  $4.5 \times 10^{-10} \text{ cm}^2/\text{sec}$  at 1200 K.

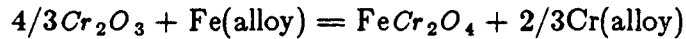
Internal sulfide precipitates can affect both the mechanism and kinetics of external scale formation. The study of the interactions between oxygen and preexisting chromium sulfide precipitate is providing insight into the significant influence of internal sulfide/oxide precipitates aspects on oxidation behavior, such as the microstructural changes and the kinetics of internal oxidation in alloys. Spengler and Viswanathan<sup>31</sup> proposed the self-sustaining process that the in-situ oxidation of internal Cr-rich sulfides releases sulfur, which then moves inward, forming new sulfide particles.



However, the formation of  $Cr_3S_4$  in the underlying alloy appears to be thermodynamically unfavorable. *EIDahasan*<sup>32</sup> et al studied the oxidation of presulfidized Co-Cr alloys, and proposed a model essentially the same as that of Spengler and Viswanathan, but noted that a thick external chromium sulfate layer initially oxidized to form an external  $Cr_2O_3$  layer at essentially the same rate as the unsulfidized alloy. Only after the integrity of the external sulfate layer was destroyed, did the internal oxidation/sulfidation start. The internal sulfide appeared to be a chromium-rich  $MS_x$ , where  $x \leq 1$ .

In addition to the study of microstructural changes in the scale and alloy, the kinetics of breakaway oxidation was also studied. A mechanism for the mechanical breakdown of protective  $Cr_2O_3$  scales was proposed by Whittle and Wood<sup>2-3</sup>. They suggested that mechanical cracking of the protective oxide, followed by scale lifting and cracking, and then finally gross mechanical failure of the protective scale permits rapid oxidation of the underlying chromium-depleted alloy. Proposed possible causes for the mechanical failure of the protective scale include the  $\alpha$ - $\gamma$  phase change in the underlying alloy, stress development during oxide growth in the scale and alloy, void

formation at the scale-alloy interface, grain growth in the alloy, etc. In earlier work, *Edstroem*<sup>33</sup> proposed that chemical transformation of  $Cr_2O_3$  scale to  $Cr_2O_3 \cdot Fe_2O_3$  solid solution and finally to  $FeO (Cr, Fe)_2O_3$  spinel facilitates the rapid outward diffusion of  $Fe^{2+}$  ions to form  $Fe_3O_4$  and  $Fe_2O_3$  layers.



However, it was demonstrated by *Whittle*<sup>34</sup> that the chemical transformation is thermodynamically unfavorable.

#### 4.1.2. Basis of the present investigation

On the basis of the earlier work, it appeared that further information leading towards a detailed understanding of the microstructural changes associated with the changes in the oxidation kinetics was required. In particular, if the breakaway is indeed associated with the evolution of a critical microstructure, it is necessary to establish clearly the ways in which this microstructure develops. In the present investigation, the study has been divided into three main sections;

- (1) the transport of sulfur in  $Cr_2O_3$  scale,
- (2) the mode of internal sulfidation in the alloy,
- (3) the oxidation of the internal sulfides.

In these sections, a fundamental model for the development of the critical microstructure is established through comparison between the microstructural changes and the breakaway kinetics.

In the first section, the Fe-Cr alloys specimens were preoxidized to form an initial  $Cr_2O_3$  scale, and then exposed to the  $CO-CO_2-SO_2$  mixed gas atmosphere. The transport of sulfur-bearing species through the initially-formed  $Cr_2O_3$  scale was thus examined.



In the second section, Fe-Cr alloys(18, 20, 25% Cr) with different grain structures(cast and homogenized, cold-rolled and annealed) were oxidized in the three different CO-CO<sub>2</sub>-SO<sub>2</sub> mixed gas atmospheres. The attack modes of internal sulfides in the two microstructures have been examined in some detail.

In the third section, internal sulfides were first formed in the underlying alloy, by oxidizing Fe-Cr alloy specimens in the CO-CO<sub>2</sub>-SO<sub>2</sub> mixed gas atmosphere. The descaled specimens were further oxidized in air, oxidizing the internal sulfides present in the alloy. The behavior of sulfur in the alloy and the extent of attack have been determined microscopically.

#### 4.1.3. Significance of present work.

The object of the present work has been to perform similar studies under conditions as previously defined as possible, thus determining the reproducibility of the phenomena, to obtain more detailed data and to provide supporting evidence for the theories advanced. To answer those questions arising from evolution of a critical microstructure, a series of three specially designed experiments were performed, not just simple as the previous experiments such as a crucible test and the mixed gas experiments. The purpose of designing the critical experiments is to conduct systematic mechanistic study, in carefully controlled conditions, of the main cause of results of previous experiments, both in crucible tests and in mixed gas experiments; sulfur transport in protective Cr<sub>2</sub>O<sub>3</sub> scale, the formation of internal sulfides in the alloy and oxidation of internal sulfides.

From the experiments designed to preoxidize Fe-Cr alloys in air, and then to further oxidize them in the high P<sub>S<sub>2</sub></sub> atmosphere, it is expected that internal Cr-rich sulfides were formed in the underlying alloy below the Cr-rich oxide layer at a limited oxidation time. If internal sulfides formed in the alloy, this means that sulfur-bearing species transported along short-circuit diffusion paths in the protective Cr<sub>2</sub>O<sub>3</sub> scale. If

internal sulfides were not observed, this means that sulfur transported by solid state diffusion via the oxide lattice or grain boundaries of the oxide at a slow rate, or enough short-circuit transport paths for short-term sulfur movement were not produced in this experiment.

From the experiments in which the Fe-Cr alloy ingots were cold-rolled to a reduction in area of about 71 % in order to increase the grain boundary area by grain refinement, it is expected that internal sulfidation would penetrate inward predominantly along the grain boundaries of the alloy. If this is the case, sulfur would diffuse inward via grain boundaries of the alloy and form internal sulfides deep in the alloy. If this is not the case, internal sulfides would be produced in the alloy matrix as well as grain boundaries of the alloy. Sulfur will diffuse intragranularly, probably down the chromium concentration gradient, i.e. chromium depletion of the underlying alloy is mainly responsible for internal sulfidation.

From the experiments designed such that the higher Cr-containing Fe-Cr alloys were presulfidized in the high  $P_{S_2}$  atmosphere, and then oxidized in air, it is expected that the rapid oxidation of internal sulfides themselves and further inward movement of liberated sulfur occur in the alloy. If this is the case, the sulfur released can diffuse further into the metal forming sulfides, in which case the attack is self-propagating and the corrosion will be a serious accelerated process. If this is not the case, the sulfur released escapes through the porous oxide to the atmosphere, in which case the attack is self-limiting and will slow down and stop unless there is a fresh supply of sulfur, and the corrosion is slow process. The role of sulfur in the alloy would be only tying up chromium necessary for formation and maintenance of protective  $Cr_2O_3$  scale.

#### 4.2. Transport of sulfur through a $Cr_2O_3$ scale

#### 4.2.1. Experimental

Table 13 summarizes the overall experimental conditions. Some specimens were preoxidized in air for 60 or 168 hours, to form  $Cr_2O_3$  scales initially at 1223 K, and they were exposed directly for 100 hours to the high  $P_{S_2}$  atmosphere ( $P_{O_2}=10^{-11.2}$ ,  $P_{S_2}=10^{-4}$ ) at 1223 K. Immediately after the preoxidation, without cooling, the inside of the reaction chamber was purged with dry argon, after which the CO-CO<sub>2</sub>-SO<sub>2</sub>-Ar gas mixture was admitted. Other specimens were preoxidized in air, generally for 100 hours, cooled to room temperature in order to generate thermal shock stresses, and then exposed to the high  $P_{S_2}$  atmosphere for different time intervals up to 500 hours.

The scale and alloy was fracture sectioned by breaking the oxidized specimens at liquid nitrogen temperature. The fractured surface was examined in an SEM equipped with an EDX. The phases present in the scale were identified using XRD from the characteristic peak positions and the corresponding intensities. The lattice constants of the  $M_2O_3$ -type scale such as  $Cr_2O_3$  or  $Cr_2O_3:Fe_2O_3$  solid solutions were calculated from the measured  $2\theta$  value, step-scanning at a very slow speeds of the order of 4 sec/step, over  $0.01^\circ$   $2\theta$  intervals. The half-widths of each (110), (116), (300), (220) peak positions were measured.

#### 4.2.2. Results

Table 14 summarizes the experimental results in the case of the oxidation of the preoxidized specimens in the mixed gas atmospheres.

##### 4.2.2.1. Metallographic observations

There was no severe sulfidation/oxidation type corrosive attack on the preoxidized specimens of the high chromium alloys such as Fe-20Cr and Fe-25Cr in the high  $P_{S_2}$  atmosphere, both in the case of a continuous isothermal transition from preoxidation to oxidation and in the case that the specimens preoxidized in air were cooled to

room temperature, heated up again, and then oxidized in the  $\text{CO-CO}_2\text{-SO}_2$  gas mixture. This observation indicates that the stresses caused by cooling to room temperature from 1223 K did not introduce any significant macro-cracks in the preformed Cr-rich oxide scale. No sulfidation/oxidation type corrosive attack was observed on preoxidized Fe-30Cr alloy specimens. A continuous protective chromium oxide scale was not formed on the Fe-15Cr alloy in air at 1223 K in any case. The Fe-15Cr alloy specimens oxidized very rapidly. The following discussion refers mainly to the corrosion of high chromium Fe-Cr alloys such as Fe-18Cr, Fe-20Cr and Fe-25Cr in the case that the specimens preoxidized in air at 1223 K were cooled to room temperature, heated up again to 1223 K, and oxidized in the high  $P_{\text{S}_2}$  atmosphere (run number: 3-6 in Table 13).

#### Fe-18Cr

A continuous protective chromium oxide scale was formed on the Fe-18Cr alloy after preoxidation in air for 100 hours. After the preoxidized specimens were cooled and then oxidized in the high  $P_{\text{S}_2}$  atmosphere, a thick two-layer scale composed of an outer Fe-oxide layer and an inner mixed Fe-Cr oxide layer was formed nearly always at the corner of the specimens. In addition, internal sulfidation was observed only below the thick two-layer scale. Figure 38 is an SEM micrograph showing the cross-section morphology of an Fe-18Cr alloy preoxidized for 50 hours in air and then oxidized for 100 hours in the high  $P_{\text{S}_2}$  atmosphere at 1223 K after cooling. The coarse internal Cr-rich sulfide particles were distributed in the underlying alloy to a depth of 20-30  $\mu\text{m}$  below the thick two-layer scale composed of an outer Fe-oxide layer and an inner mixed Fe-Cr oxide layer at the corner of the specimens, and the outside part of inner Cr-oxide layer also contained sulfur i.e. sulfur-pocketing.

#### Fe-20Cr

A continuous protective chromium oxide scale was uniformly formed on the Fe-20Cr alloys after preoxidation in air. No sulfidation/oxidation type corrosive attack was observed on Fe-20Cr alloy specimens which were preoxidized for 100 hours in air and subsequently oxidized in the high  $P_{S_2}$  atmosphere for up to 500 hours at 1223 K. The sulfur penetration was completely prevented by the initial  $Cr_2O_3$  scale. No sulfur was detected on the microscopical level, in the cross-section of the scale and alloy, and also in the fracture section.

Even after the oxidation in the high  $P_{S_2}$  atmosphere, the preoxidized specimens remained still covered uniformly with a thin, adherent Cr-oxide scale, without showing any spallation of scale. However, the Fe-20Cr alloy specimens directly exposed to the high  $P_{S_2}$  atmosphere showed a tendency for part of the Cr-oxide scale to spall off locally. Figure 39 compares the spalling tendency of the scale formed on Fe-20Cr alloy, in two cases of both with and without preoxidation in air.

#### Fe-25Cr

A continuous protective chromium oxide scale was uniformly formed on all Fe-25Cr alloy specimens after the oxidation in air at 1223 K for up to 1150 hours. There was no severe sulfidation/oxidation type corrosive attack on Fe-25Cr alloy specimens which were preoxidized for 100 hours in air and then oxidized in the high  $P_{S_2}$  atmosphere at 1223 K. Fragmentation of noble metal in the scale occurred locally at the inner part of the Cr-rich oxide layer. Cr-rich oxide nodules having whiskers were produced on the external surface of the Cr-oxide scale. A uniform Cr-rich oxide scale, large pores in the scale, and a discontinuous distribution of large voids at the scale-alloy interface, were observed in the fracture sections of the scale and alloy.

Figure 40 shows an SEM fractograph of the scale and metal for a Fe-25Cr alloy which was preoxidized for 100 hours in air, cooled to room temperature, and further

oxidized for 500 hours at 1223 K in the high  $P_{S_2}$  atmosphere (run number 6, in Table 13). After the preoxidized specimens were oxidized for 500 hours in the high  $P_{S_2}$  atmosphere, small amounts of internal Cr-rich sulfide particles were embedded in the underlying alloy below the Cr-rich oxide layer. The penetration depth of Cr-rich sulfide particles in the underlying alloy was about 47  $\mu\text{m}$ , and the scale thickness measured was about 20  $\mu\text{m}$ . This alloy appeared to fracture intragranularly along crystallographic planes rather than along the grain boundaries at liquid nitrogen temperature.

#### 4.2.2.2. Structural analysis by X-ray diffraction

The lattice constants of  $M_2O_3$  solid solutions such as the  $(Cr,Fe)_2O_3$  scale formed on the Fe-Cr alloys were calculated from the d-values measured from four different Bragg angles. When the  $Cr_2O_3$ -rich scale produced on the higher Cr-containing Fe-Cr alloys such as Fe-20Cr and Fe-25Cr was step-scanned in a X-ray diffractometer, the strongest intensity peak was originated from the chromium oxide grown on a (110) crystallographic plane instead of (104) plane reflections taken from the JCPDS file. Figure 41 shows the variation of lattice constants as a function of the Cr-content in the Fe-Cr alloys. The lattice constants based on the hexagonal indices are used. As the chromium content in the Fe-Cr alloys decreased, the lattice constants in the  $\alpha-Cr_2O_3-Fe_2O_3$  solid solution increased i.e. the amount of  $Fe_2O_3$  dissolved in the  $Cr_2O_3$  scale increased.

In Figure 42 are plotted the variation of half-width of the (110), (116), (300), (220) peak lines, and the lattice constants as a function of scattering angle. The strain and size of crystalline phase can be analyzed by X-ray line-broadening measurements. Qualitatively, the greater broadening of the diffraction peaks indicates a larger strained oxide<sup>36</sup>, assuming that the crystallite size exceeds 0.1  $\mu\text{m}$ , and the oxide layer is thin. The line broadening indicating the strained oxide scale in this case increased

as the scattering angle increased i.e. as the depth within the scale from the external surface increased.

### 4.3. Internal sulfidation

#### 4.3.1. Experimental

In order to increase the grain boundary areas, the following thermomechanical treatments were performed on the alloy ingots. The homogenized Fe-18Cr, Fe-20Cr and Fe-25Cr alloy ingots were hot-rolled at 1373 K to 4.2 mm thick sheets from 25.4 mm thick disks. Sheets 2.7 mm thick were subsequently produced by cold-rolling, and intermediately annealed at 473 K for 6 hours. The sheets were further cold-rolled to 1.2 mm thick; representing a total 71% cold reduction, and finally annealed for 1 hour at 1223 K. The alloys were then cut into specimens approximately 15 x 10 x 1 mm. The entire specimen surface was polished to 600 grit silicon carbide paper, and a hole drilled in one end. The cast and homogenized specimens and the cold-rolled and annealed specimens were then exposed to CO-CO<sub>2</sub>-SO<sub>2</sub>-Ar gas atmospheres at 1223 K. Table 15 summarizes the experimental conditions.

#### 4.3.2. Results

The grain size of Fe-Cr alloy specimens was reduced by the cold-rolling and annealing treatment to about 50-110  $\mu\text{m}$  from 320-800  $\mu\text{m}$  (average: 520  $\mu\text{m}$ ), irrespective of Cr-content in Fe-Cr alloys, as shown in Table 16. The effect of grain structure of the alloys on the corrosion behavior has been compared for the three different atmospheres. Table 17 shows the experimental results in the case of the oxidation of the cold-rolled and annealed Fe-Cr alloys in the mixed gas atmospheres at 1223 K. Table 18 shows the scale thickness and the penetration depth of the coarse grained and small grained Fe-Cr alloys such as Fe-20Cr and Fe-25Cr, after 100 hours oxidation, in the sulfur-containing environment. In the high  $P_{S_2}$  atmosphere, the penetration depth of internal sulfidation front in the small grained specimens were deeper than that in the

coarse grained specimens, in case of 100 hours oxidation of both Fe-20Cr and Fe-25Cr. In the low  $P_{S_2}$  atmosphere, slight internal sulfidation was observed in the small grained specimens. In contrast, no internal sulfidation was observed in the coarse grained specimens. The small grained Fe-Cr alloy specimens were corroded more severely than the coarse grained specimens, probably because of the enhanced diffusion in the alloy resulting from the increase in grain boundary area. At the early stages of the oxidation, diffusion outwards from the alloy is rate-controlling. Whereas later on, diffusion in the scale predominates.

#### Fe-18Cr

In the low  $P_{S_2}$  atmosphere ( $P_{S_2}=10^{-5}$  atm), after 100 hours, the small grained specimens had a uniform  $Cr_2O_3$  scale thicker than the coarse grained specimens. All specimens were consumed completely after 200 hours oxidation. In the high  $P_{S_2}$  atmosphere ( $P_{S_2}=10^{-4}$  atm), the specimens were severely corroded by the rapid oxidation/sulfidation attack. All specimens were completely consumed after 100 hours oxidation. In the low  $P_{SO_2}$  atmosphere ( $P_{SO_2}=0.004$ ,  $P_{O_2}=10^{-12.0}$ ,  $P_{S_2}=10^{-4.0}$  atm), internal sulfidation was observed.

#### Fe-20Cr

In the low  $P_{S_2}$  atmosphere, the small grained specimens developed a uniform  $Cr_2O_3$  scale of essentially the same thickness as the coarse grained specimens. No internal sulfidation was observed. In the high  $P_{S_2}$  atmosphere, the small grained specimens were internally sulfidized/oxidized deeper than the coarse grained specimens, as shown in Table 18a. In the low  $P_{SO_2}$  atmosphere, the scale had developed a two-layer structure after 100 hours, and the internal Cr-rich sulfide particles were observed just below the two-layer scale to a depth of 9-12  $\mu$ m. Figures 43 and 44 show the cross-section morphologies of Fe-20Cr alloys (coarse grained, small grained) oxidized for 200



hours in the low  $P_{SO_2}$  atmosphere at 1223 K. In the small grained specimen, a band of sulfide/oxide particles leads the catastrophic corrosion. As shown in Figure 43, the front of Cr-rich sulfide particles advanced into the alloy, followed by severe internal oxidation of the alloy. Meanwhile, in the coarse grained specimen as shown in Figure 44, the internal Cr-rich sulfide particles were observed just below the two-layer scale, which spreads laterally destroying the remaining Cr-oxide scale.

#### Fe-25Cr

In the low  $P_{S_2}$  atmosphere, the scale formed on the small grained specimen was thicker at the early stage of oxidation such as after the 100 hours oxidation run than that on the coarse grained specimen. But after 200 hours oxidation, the thickness of the scale on both specimens was approximately the same. No internal sulfidation was observed. In the high  $P_{S_2}$  atmosphere, internal sulfidation was observed in both the coarse grained and the small grained specimens, and a characteristic two-layer scale composed of an outer Fe-oxide and an inner Cr-rich oxide was formed on both specimens. In the low  $P_{SO_2}$  atmosphere ( $P_{SO_2}=0.004$ ,  $P_{O_2}=10^{-12.0}$ ,  $P_{S_2}=10^{-4.0}$  atm), the scale thickness varied in similar fashion to that in the low  $P_{S_2}$  atmosphere ( $P_{O_2}=10^{-11.2}$ ,  $P_{S_2}=10^{-5}$  atm), and no internal sulfidation was observed.

#### 4.4. Oxidation of internal sulfides

##### 4.4.1. Experimental

Table 19 summarizes the experimental conditions. The specimens were presulfidized in the high  $P_{S_2}$  atmosphere ( $P_{O_2}=10^{-11.2}$ ,  $P_{S_2}=10^{-4.0}$  atm) for 100 hours at 1223 K, cooled to room temperature to cause scale spalling either partially or completely, and then oxidized in air for up to 500 hours.

The cross-section morphologies of the scale and alloy were examined using optical metallography. The chemical analysis of the corrosion products was carried out mainly

with an EDX unit attached to the SEM. The distribution of each element such as Fe, Cr, S was determined mainly from the EDX elemental mapping of selected areas. The distribution of oxygen and the depth profile of particular element such as sulfur were determined using Auger Electron Spectrometry.

#### 4.4.2. Results

The internal Cr-rich sulfide particles were embedded in the underlying alloy, after the Fe-Cr alloy specimens were presulfidized in the  $\text{CO-CO}_2\text{-SO}_2$  gas mixture. The penetration depth of internal sulfides in the Fe-20Cr alloy was deeper than in the Fe-25Cr alloy. As the Cr-content in the Fe-Cr alloys decreased, the penetration depth of internal sulfides increased.

Figure 45 shows the cross-section morphology of the Fe-25Cr alloy corroded for 100 hours in the high  $P_{\text{S}_2}$  atmosphere at 1223 K. From the quantitative analysis of the characteristic Auger spectrum, the internal Cr-rich sulfide particles were determined to be CrS. By varying the sputtering time, a light gray area (point 5 in Figure 45) located at the inner part of the scale was determined to have a chromium sulfide-rich shell;  $\text{Cr}_x(\text{S},\text{O})$ , covering a core of a relatively sulfur-poor chromium oxide;  $\text{Cr}_y(\text{O},\text{S})$ . A convention is used in which  $\text{M}(\text{A},\text{B})$  implies a compound in which the amount of the element A exceeds that of B. The measured sulfur content decreased as the sputtering time increased. The scale formed on the Fe-25Cr alloy was determined to be  $\text{Cr}_2\text{O}_3$  containing little or no sulfur, from X-ray diffraction, EDX analysis and Auger analysis.

#### Fe-20Cr

A network composed of an initial thin layer of Cr-rich particles containing sulfur followed by a thicker layer of Cr-rich oxide particles was formed at the frontier between the inner Cr-rich oxide layer and the underlying alloy, in the case of very severe attack. The amount of sulfur detected by the EDX was low, close to the

detectability limit of the EDX. The formation of a network seems to be closely related to the catastrophic oxidation of the Fe-20Cr alloy.

Figure 46 shows an SEM micrograph exhibiting the cross-section morphology of an Fe-20Cr alloy presulfidized for 100 hours in the high  $P_{S_2}$  atmosphere ( $P_{O_2} = 10^{-11.2}$ ,  $P_{S_2} = 10^{-4.0}$  atm) and then oxidized for 500 hours in air at 1223 K. The coarse compact Cr-rich particles containing some sulfur were produced at the advancing front of internal oxidation, leading to maximum penetration into the alloy. A long porous Cr-rich oxide stringer perpendicular to the scale-alloy interface followed behind it.

#### Fe-25Cr

Figure 47 shows the cross-section morphology of an Fe-25Cr alloy presulfidized for 100 hours in the high  $P_{S_2}$  atmosphere, and then oxidized for 500 hours in air at 1223 K. The coarse internal Cr-rich sulfide particles penetrated deeply into the alloy, and the Cr-rich oxide intrusions also penetrated into the alloy following the coarse particles. The penetration depth of the coarse sulfides was about 40-50  $\mu\text{m}$ , greater than that of the fine sulfides. In other words, the size of the internal sulfides apparently increased as the penetration depth increased. From the quantitative analysis of Auger spectra, the internal sulfide particles were determined to be CrS. The sulfur contents in the chromium sulfides were the same at two different sputtering times; 5 minutes and 8 minutes (point 1, 3 in Figure 47). The porous area behind the CrS was determined to be  $\text{Cr}_2\text{O}_3$  (point 5 in Figure 47). The Cr-rich oxide intrusion contained a little sulfur (point 0 in Figure 47). Elemental mapping of selected areas exhibits clearly the distribution of corrosion products such as CrS,  $\text{Cr}_2\text{O}_3$  and Cr-rich oxide intrusion.

Figure 48 shows an optical micrograph exhibiting the cross-section morphology of the Fe-25Cr alloy presulfidized for 100 hours in the high  $P_{S_2}$  atmosphere, and then oxi-

dized for 500 hours in air at 1223 K. The coarse internal Cr-rich sulfides were interconnected each other, nearly separating the internal oxidation zone below the scale from the alloy matrix. The Cr-rich oxide intrusions penetrated perpendicular to the scale-alloy interface. The interconnected Cr-rich sulfides indicate the sideways growth of coarse sulfides and the negligible advancement of sulfides into the alloy. The penetration depth of coarse sulfides was about 18-23  $\mu\text{m}$ , which was relatively shallow compared to the penetration depth of 40-50  $\mu\text{m}$  measured in case of inward growth of coarse sulfides, as shown in Figure 47. The internal Cr-rich sulfides produced in the high  $P_{S_2}$  atmosphere were coarsened by the subsequent oxidation treatment. The Cr-rich oxide intrusion penetrated into the alloy behind the advancing front of coarse Cr-rich sulfides. Briefly summarizing, two types of coarsening of internal Cr-rich sulfides were observed. One is inward movement and growth, and the other is sideways growth. The small grained alloy was attacked more severely than the coarse grained.

#### Fe-30Cr

The Cr-rich oxide scale produced in the  $\text{CO-CO}_2\text{-SO}_2$  gas mixture readily spalled. Even after further oxidation in air for 500 hours at 1223 K, there was no severe attack of the Fe-30Cr alloy. The maximum penetration depth of the internal particles was only about 10-15  $\mu\text{m}$ , and a two-layer scale did not develop.

#### 4.5. Concluding remarks.

The development of the critical microstructure is schematically represented in Figure 49.

##### (1) Transport of sulfur in the protective chromium oxide.

The cooling stresses caused by cooling to room temperature from 1223 K did not introduce any significant macro-cracks in the preformed Cr-rich oxide scale. No sulfur

was detected in the Fe-20Cr alloy on the microscopic level, in the cross-section of the scale and alloy, and also in the fracture section. Small amounts of internal Cr-rich sulfide particles were embedded to a depth of about 47  $\mu\text{m}$  in the Fe-25Cr alloy below the Cr-rich oxide layer with a thickness of about 20  $\mu\text{m}$ . Sulfur-bearing species appear to transport inward through the protective Cr-oxide scale along short-circuit diffusion paths such as grain boundaries of the oxide, microcracks or pores.

## (2) Internal sulfidation

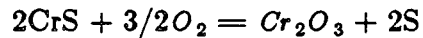
Internal Cr-rich sulfide particles were precipitated in the underlying alloy to a constant depth below the scale-alloy interface, which seems to be the frontier of Cr-depletion zone of the alloy. The internal sulfides coarsened with time. The size of the internal sulfides apparently increased as the penetration depth increased. The penetration depth of internal sulfidation front in the small grained specimens was deeper than that in the coarse grained specimens, in case of both Fe-20Cr and Fe-25Cr. Preferential penetration of internal sulfidation along the grain boundaries of the small grained alloy was not observed. The small grained cold-rolled and annealed alloys with their increased grain boundary areas corroded more severely than the coarse grained cast and homogenized alloys.

In the small grained Fe-20Cr alloy specimens, a band of front sulfides/rear oxides network leads to the rapid oxidation of alloy in the low  $P_{SO_2}$  atmosphere ( $P_{SO_2} = 0.004$  atm). The front of Cr-rich sulfides advanced into the alloy, followed by severe internal oxidation of the alloy. Meanwhile, in the coarse grained Fe-20Cr alloy specimens, the internal Cr-rich sulfide particles were formed just below the characteristic two-layer scale composed of an outer Fe-oxide and an inner Cr-rich oxide, in the low  $P_{SO_2}$  atmosphere ( $P_{SO_2} = 0.004$  atm).

## (3) Oxidation of internal sulfides.

The internal Cr-rich sulfide particles were determined to be CrS from the quantitative analysis of the characteristic Auger spectra. Oxidation of the internal sulfides themselves leads to accelerated internal oxidation of alloy. In the Fe-20Cr alloy, the coarse compact Cr-rich particles containing some sulfur were produced at the advancing front of internal oxidation, leading to maximum penetration into the alloy. Long, porous Cr-rich oxide particles were observed behind the CrS. The front of coarse internal Cr-rich sulfides moves inwards and/or grew sideways till interconnected, followed by deep penetration of Cr-rich oxide intrusions, resulting in heavy metal loss.

The anticipated chemical reaction is



From the in-situ internal oxidation of CrS, a porous  $\text{Cr}_2\text{O}_3$  would be left behind it, because of the difference in the Pilling-Bedworth ratio. Liberated sulfur released from the above chemical reaction does not appear to escape to the atmosphere, but moves further inward into the alloy. If this is the case, the sulfidation/oxidation corrosive attack is a self-sustaining process.

## 5. Discussion

### 5.1. The corrosive environment within the bed of a fluidized bed combustor

Calcium sulfate is solid and thermodynamically stable in air in the temperature range 1023-1223 K,<sup>36</sup> this is the operating temperature range of a fluidized bed combustor. However, calcium sulfate deposited on the hotter metal surfaces in fluidized bed combustors would be decomposed to  $SO_2$  at a relatively low oxygen partial pressure.



Figure 50 shows the thermodynamic phase stability diagram for the Ca-O-S system at 1123 K and at 1223 K *respectively*<sup>37</sup>. If the oxygen partial pressure is sufficiently low, the sulfur activity could be increased theoretically to a level equal to that at the  $CaSO_4/CaO/CaS$  triple point within the bed of a fluidized bed combustor. In other words, the sulfur activity within the bed could be increased to  $10^{-3.5}$  atm at 1223 K, and to  $10^{-4.5}$  atm at 1123 K.

The nature and extent of corrosion observed in laboratory crucible experiments using  $CaSO_4$ -containing powder mixtures in low oxygen partial pressure atmospheres, have been compared with those obtained in the experiments using  $CO-CO_2-SO_2$  gas mixtures chosen to simulate the sulfur and oxygen activities in the low oxygen partial pressure locations in fluidized bed combustors. In the crucible test, the formation of internal Cr-rich sulfide/oxide particles in the underlying Fe-20Cr alloy below an inner Cr-rich oxide layer was a common observation. In the mixed gas atmospheres, internal Cr-rich sulfides were formed in the Fe-20Cr alloy in the range of sulfur activity of  $10^{-5}$ - $10^{-4}$  atm at the fixed oxygen partial pressure of  $10^{-11.2}$  atm at 1223 K. The range of sulfur activity of  $10^{-5}$ - $10^{-4}$  atm is still below the theoretical maximum value at the  $CaSO_4/CaO/CaS$  triple point, lying close to the  $CaSO_4/CaO$  equilibrium line. In other

words, it is believed the sulfur activity is increased high enough to sulfidize the alloy along the  $CaSO_4/CaO$  equilibrium line as a direct consequence of the low oxygen partial pressure. This indicates that generation of a sulfidizing gas mixture by the principal components of a compact deposit, i.e.  $CaSO_4$  and  $CaO$ , is possible mechanism of sulfidation relevant to fluidized bed combustor. In other words, the sulfur-containing species  $SO_2$  was evolved from the  $CaSO_4/CaO$  equilibrium in the low oxygen partial pressure atmospheres created by the  $CO/CO_2$  gas mixture. The evolution of  $SO_2$  gas in crucible tests was  $CaSO_4$  decomposition reaction dependent and time-limited in this laboratory experiments. A solid state reaction between a  $CaSO_4$  deposit and a protective  $Cr_2O_3$  scale is probable, but not serious. Even if a mixture of  $CaO$  and  $Cr_2O_3$  was formed by a solid state reaction, it appears to be insignificant in controlling the overall corrosion mechanism. Comparison of observations in the crucible experiments and in the mixed gas experiments indicates that sulfidation/oxidation corrosion is very likely under some circumstances within the bed in a fluidized bed combustor. This type of corrosion has the potential for breakaway--an acceleration in rate after a certain time-- and thus it can be very useful to develop a detailed understanding of the reaction in the hope of the being able to predict the onset of breakaway.

## 5.2. Sulfidation/oxidation corrosion

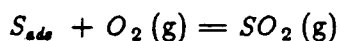
Iron-chromium alloys in sulfur-containing atmospheres developed irregular interfaces between the scale and the alloy, fragmentation of noble metal in scale, the formation of internal sulfides/oxides in the alloy, sulfur-enrichment in the innermost part of the inner Cr-rich oxide, and the formation of a non-protective two-layer scale. The internal sulfides formed were chromium-rich. The variation in the attack modes in sulfidation/oxidation corrosion on iron-chromium alloys with the partial pressure of  $SO_2$  and the activity of sulfur is represented in Table 10, and schematically in Table 11. The activity of sulfur played an important role determining whether



sulfidation/oxidation corrosion occurred or not. Internal sulfidation was observed to be related to the  $SO_2$  partial pressure: for a fixed sulfur partial pressure of  $10^{-4}$  atm, internal sulfidation was observed for an  $SO_2$  partial pressure above 0.004 atm in the case of the Fe-20Cr alloy, and at 0.026 atm in the Fe-25Cr alloy. The extent of sulfidation/oxidation corrosion decreased as  $P_{SO_2}$  decreased. The partial pressure of  $SO_2$  was a more decisive factor than the sulfur activity in the development of sulfidation/oxidation corrosion. In other words, the development of the critical microstructure leading to breakaway was dependent more on  $P_{SO_2}$  than  $P_{S_2}$ .

Three possible explanations for dependency of the microstructure on  $P_{SO_2}$  can be suggested<sup>38</sup>,

- (1) the gaseous transport of  $SO_2$  through the scale is the controlling process.
- (2) the amount of  $SO_2$  in the atmosphere is high.
- (3) desorption of  $SO_2$  from the external surface is a slow step.



If the desorption step of sulfur is slow, then the scale is covered with adsorbed sulfur, and adsorbed sulfur will accumulate at the surface until it is removed by sulfide formation, and sulfur moves through traps at grain boundaries of the scale. The sulfide formation will occur at the interface, and this will generate a two-phase structure with sulfide embedded in the oxide; sulfur could be removed by diffusion inward through the oxide to form sulfide beneath the oxide layer. As shown in Figure 45, a sulfide layer was embedded in the chromium oxide. The concept of the reaction path is useful as an aid in visualizing possible phase distributions where transport is rate controlling; no quantitative and active model has yet been developed. Figure 52 shows the possible reaction path for formation and distribution of sulfides in the scale and alloy.

The Cr-content in a Fe-Cr alloy was also critical. The Fe-20Cr alloy exhibited good resistance to spalling particularly in the sulfur-containing atmospheres, but after the local failure of the protective  $Cr_2O_3$  scale the alloy corroded rapidly forming a thick two-layer scale. In this case, sulfur penetrated deep into the alloy. Meanwhile, although the  $Cr_2O_3$  scale formed on the Fe-25Cr alloy spalled off relatively easily in the sulfur-containing atmospheres, the overall oxidation rate of the alloy did not accelerate greatly. Sulfur could assist spalling of scale on the Fe-25Cr alloy, i.e. hurt chemically the bonding between the scale and alloy, but could not penetrate deep into the alloy. As the Cr-content in the Fe-Cr alloys increased, the penetration depth of internal sulfides decreased, and ultimately sulfidation/oxidation corrosion was retarded. Figure 51 shows the variation of the maximum penetration depth of Fe-Cr alloys with Cr-content. The maximum penetration depth of internal sulfides, representing the corrosion rate of material at given environmental condition, saturated to a constant depth below the inner Cr-rich oxide layer as the oxidation time increased. In the mixed gas environments, the maximum penetration depth was 30-40  $\mu\text{m}$  in the Fe-25Cr alloy, and 40-50  $\mu\text{m}$  in the Fe-20Cr alloy in the high  $P_{S_2}$  atmosphere.

### 5.3. The development of the critical microstructure

Growth kinetic data such as the weight gain, scale thickness, and the penetration depth of internal sulfides/oxides into the alloy as a function of reaction time indicate that the conditions leading to the transition from 'protective' to 'nonprotective' behavior, so-called "breakaway", are deeply involved in the microstructure, depending on the alloy (Cr-content, grain structure) and the environment ( $P_{S_2}$ ,  $P_{SO_2}$ ). Breakaway oxidation is unpredictable, but interpretable, in that it can be correlated with microstructural changes in the reaction products and the underlying alloy. Experimentally, it is still difficult to attain reproducibility in the measurement of breakaway time even

in very carefully controlled conditions. In the near future, the information on the microstructural changes occurring before breakaway are far more valuable in estimating the possibility of accelerated corrosion, and are easy to attain in this kind of laboratory scale experiment. In sulfidation/oxidation corrosion, it is postulated that a "critical microstructure" developed before breakaway occurred.

The critical microstructure regarded as a precursor of breakaway in the present work developed as a result of the formation and growth of the internal sulfides/oxides in the underlying alloy. The schematic of the critical microstructure developed in sulfidation/oxidation corrosion is represented in Figure 37, obtained from the experimental observations in the mixed gas atmospheres. Microstructural evidence indicates that the formation of internal sulfides leads to internal oxidation, fragmentation of the more noble metal in the scale, instability of the interface between scale and alloy, and inability of alloy to regenerate a protective oxide. The question then arises as to how the critical microstructure develops.

The development of the critical microstructure involves the transport of sulfur in the protective Cr-oxide, the formation of internal sulfides in the alloy, the internal oxidation of the sulfides, and the inward diffusion of the released sulfur to form new sulfides. Sulfur-bearing species transport inward through the protective Cr-oxide scale along short-circuit diffusion paths. Internal Cr-rich sulfide particles are then precipitated and coarsen in the underlying alloy to a constant depth below the scale-alloy interface, which seems to be the frontier of the Cr-depletion zone of the alloy, presumably corresponding to a plane at which the outward chromium diffusion from the bulk of the alloy balances the inward diffusion of sulfur from the surface. The front of Cr-rich sulfide particles advance into the alloy, and in-situ oxidation of the internal sulfides leads to accelerated internal oxidation of the alloy.

### 5.3.1. Sulfur transport in the protective $Cr_2O_3$ .

The following three mechanisms have been proposed for the transport of sulfur through the  $Cr_2O_3$  scale<sup>39-40</sup>;

- (1) the more or less uniform sulfur distribution in the  $Cr_2O_3$  scale followed by the solid state diffusion of sulfur inward either via lattice or grain boundary.
- (2) the transport of sulfur-bearing gas molecules like  $SO_2$  through physical defects in the  $Cr_2O_3$  such as pores and microcracks.
- (3) the formation of connected networks of sulfides channels through the  $Cr_2O_3$  scale.

Figure 53 shows a schematic diagram exhibiting the possible transport paths of sulfur through the scale and alloy. If the amount of  $SO_2$  is high, or if desorption of  $SO_2$  at surface is the slow step, sulfide channels would also be possible in the scale. The formation of sulfide channels would provide rapid transport paths, short-circuiting the oxide lattice. As shown in Figure 13, both solid state diffusion of sulfur and molecular transport of sulfur-bearing gas species are possible simultaneously in the selective oxidation of chromium at the experimental conditions of this work.

As calculated in Appendix 8.3., the minimum estimated value of the sulfur diffusion coefficient in  $Cr_2O_3$  from the present work is about  $5.5 \times 10^{-13} \text{ cm}^2/\text{sec}$  at 1223 K. Figure 54 shows the previously reported data for the diffusion coefficients of chromium<sup>41-42</sup>, oxygen<sup>22</sup> and sulfur<sup>21</sup> in  $Cr_2O_3$ . The sulfur diffusion coefficient in hot-pressed  $Cr_2O_3$  is about  $10^{-10} \text{ cm}^2/\text{sec}$  at 1273 K. The diffusion coefficient of sulfur is about six orders of magnitude higher than the diffusion coefficient of oxygen. Comparison of the calculated value of  $D_S$  with the previously reported  $D_O$  and  $D_S$  values indicates that sulfur probably was transported through short-circuit paths in the Cr-oxide scale such as microcracks and pores for gaseous transport, and/or grain boundaries for solid state diffusion.

Other indirect experimental evidence supporting  $SO_2$  molecular transport through microcracks and pores in the protective  $Cr_2O_3$  scale is as follows;

- (1) The partial pressure of  $SO_2$  played a more decisive role than the activity of sulfur in determining the development of corrosion, as given in Table 10 and Table 11.
- (2) Small amounts of internal sulfide particles were observed at the fracture section only in the preoxidized Fe-25Cr alloy specimens. The scale formed on the Fe-25Cr alloy tends to be susceptible to cracking during cooling to room temperature. Meanwhile, in the preoxidized Fe-20Cr alloy specimens which showed excellent resistance to spalling, internal sulfide particles were not observed even after oxidation in the high  $P_{S_2}$  atmosphere. In other words, sulfur diffused through physical imperfections such as microcracks.
- (3) A sulfur concentration gradient was not observed in the scale, even in the case where sulfur was detected near the scale-alloy interface.
- (4) In the two-layer scale, sulfur was detected only at the inner porous Cr-rich oxide layer.
- (5) In the preoxidized Fe-18Cr alloy specimens, coarse internal sulfide particles were observed mostly at the corner, a geometrically sensitive site for cracking of the scale.

### 5.3.2. The formation of internal sulfides in the alloy.

Internal sulfidation preferentially along the grain boundaries of the alloy was not observed even in the cold-rolled fine-grained specimens, though the overall corrosion rate was increased by grain refinement. It could be explained that intergranular corrosion is possible when there is chromium depletion of the grain boundary regions, caused by carbide *precipitation*<sup>43</sup> in carbon-containing stainless steels such as Types 304 and 310. However, in the carbon-free binary Fe-Cr alloys, preferential intergranular

corrosion is not necessarily developed, but severe corrosion occurred, probably caused by the enhanced grain boundary diffusion of chromium outward, and sulfur and oxygen inward, along the increased grain boundaries in the alloy.

Internal sulfides were commonly observed in the underlying alloy below an inner Cr-rich oxide layer to a constant depth of about 20-50  $\mu\text{m}$ , in the case of the two-layer scale composed of an outer Fe-oxide layer and an inner Cr-rich oxide layer. The size of internal sulfide particles increased as the penetration depth increased, as shown in Figure 47. Figure 55 shows schematically the chromium concentration gradient and the size of sulfides as a function of distance from the scale-alloy interface. Qualitatively, the particle radii were proportional to the distance from the scale-alloy interface. *Rapp*<sup>28</sup> derived the equation describing the radius of spherical precipitates produced by exclusive internal oxidation of alloys.

Using this approach, the radius  $r(X)$  of spherical sulfides may be expressed by

$$r(X) = \left( \frac{3VN_{Cr}}{3\pi\beta} \right)^{1/3} \cdot \frac{X}{N_{O^{(S)}}}$$

where

$$\beta = \frac{1}{N_{O^{(S)}}} \frac{X}{\Delta X}$$

$N_{O^{(S)}}$  : the mole fraction of oxygen at the external surface

$N_{Cr}$  : the mole fraction of chromium in the bulk alloy

$\Delta X$  : the distance between precipitates

$V$  : molar volume of  $Cr_2O_3$

$X$  : penetration depth

$N_{Cr}$  increases as  $X$  increases, because of Cr-depletion in the alloy. Therefore,  $r(X)$  increases also as  $X$  increases i.e. internal sulfides coarsen at the precipitation front. This coarsening is related to the balance between the flux of oxidants inwards

and the flux of chromium out. The internal sulfides could block the inward diffusion of oxygen, and the outward diffusion of chromium. Eventually, the formation of the sulfide prevents the development of the normal continuous protective oxide layer. Because the chromium is tied up as internal oxide particles, the alloy loses its ability to regenerate its protective chromium oxide scale.

As also given in Figure 27 showing the affected zone preferentially etched by Vilella's reagent, the Cr-depletion is a major cause for the formation of the internal Cr-rich sulfide particles. Sulfur appears to diffuse through the bulk and/or along the grain boundaries down the concentration gradient of chromium. From the concentration profiles measured by *Whittle*<sup>2-3</sup> for various Fe-Cr alloys, the depth and extent of the Cr-depletion zone could be estimated.

### 5.3.3. The internal oxidation of sulfides.

The descaled alloy having internal Cr-rich sulfides oxidized rapidly. Originally, it was believed that the removal of the chromium to form the sulfide allowed the rapid oxidation of the depleted matrix.

In addition, the chromium-rich sulfides themselves oxidize rapidly, forming a layer in which particles of metal depleted in chromium are embedded in a non-protective chromium-rich oxide matrix. The front of internal sulfides advanced into the alloy leading a band of internal oxides, followed by oxide intrusion without forming the protective Cr-oxide, as shown in Figure 46 and 47.

The anticipated chemical reaction between internal sulfides and oxygen is thus to some extent

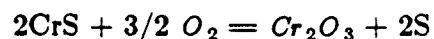


Figure 56 describes the mechanism of the formation of porous  $\text{Cr}_2\text{O}_3$  and the inward movement of liberated sulfur. The liberated sulfur released from the chemical reaction appears to be driven inwards into alloy, and does not escape to the

atmosphere. If this is the case, the reaction will be a self-sustaining process.

The interesting common observations are that sulfur at the scale-alloy interface diffused passing through the Cr-depletion zone in the underlying alloy just below the  $Cr_2O_3$  scale, and internal sulfides precipitated at the frontier of Cr-depletion zone. However, oxygen alone could not diffuse inward in the underlying alloy in the absence of sulfur.

In the absence of sulfur, oxygen diffuses inward and forms internal oxides behind the advancing internal sulfides. If so, oxygen needs certain short-circuit transport paths, definitely related to sulfur, for its inward movement. In this case, sulfur plays some role for oxygen movement. There are several possibilities for the oxygen diffusion:

- (1) through the bulk of the depleted alloy to the CrS particle,
- (2) down alloy grain boundaries to the CrS,
- (3) along the boundary between  $Cr_2O_3$  and CrS at/near the alloy grain boundaries,
- (4) through micropores resulting from the volume difference between  $Cr_2O_3$  and CrS.

#### 5.4. Breakaway oxidation

The stability of  $Cr_2O_3$  scale, mechanically and/or chemically, is very important from the viewpoint of high temperature corrosion resistance. Major compositional and microstructural changes occurring during breakaway oxidation, both mechanically and chemically, are schematically represented in Figure 57. Whittle<sup>2-3</sup> proposed a mechanical breakdown model. It was suggested that the mechanical failure of  $Cr_2O_3$  scale in an oxidizing atmosphere permits rapid oxidation of the underlying chromium-depleted alloy.

In the sulfur-containing atmosphere, chemical breakdown is more probable by developing the critical microstructure before the mechanical failure of  $Cr_2O_3$  scale



occurs. The critical microstructure developed by the formation of internal sulfides/oxides in the underlying alloy could cause the "breakaway process". The behavior exhibiting the breakaway kinetics in the high  $P_{S_2}$  atmosphere and the protective kinetics in the low  $P_{S_2}$  atmosphere are good evidence illustrating the role of sulfur in the scale and alloy, as already given in Figure 16.

The breakaway oxidation process could be divided into three periods by focusing on the microstructural changes;

- (1) precipitation of internal sulfides in the underlying alloy,
- (2) coarsening of the sulfides and scale separation as two thin layers composed of an outer Fe-oxide and an inner Cr-rich oxide,
- (3) formation of thick nodules composed of an outer Fe-oxide and an inner mixed Fe-Cr oxide, and sideways growth of the thick two-layer scale nodule.

Figure 58 describes schematically the breakaway process occurring during the formation of the critical microstructure. In the sulfur-containing atmosphere, the chemical interaction between sulfur and  $Cr_2O_3$  appears to be one of the causes for the destruction of the  $Cr_2O_3$  scale. Sulfur assists the breakthrough of  $Cr_2O_3$  scale formed on the Fe-Cr alloys. In other words, sulfur in some form, probably at the grain boundaries of the oxide, increases the growth rate of  $Cr_2O_3$ , with a slight deviation from parabolic kinetic behavior.

One explanation for chemical breakdown of the protective  $Cr_2O_3$  scale induced by sulfur is possible if the presence of a sulfur-rich region or sulfide layer within the  $Cr_2O_3$  scale is postulated, while internal sulfides precipitated in the alloy. It is strongly probable that the scale formed in the sulfur-containing atmospheres at the early stage of oxidation would appear in analysis to be simply  $Cr_2O_3$  if sulfur present within the scale is below the detection limit of the EDX used in the characterization of

reaction products. Sulfide or sulfur-rich regions near the grain boundaries of  $Cr_2O_3$  scale would provide the short-circuit diffusion paths for reactants in the following oxidation. Experimentally, the  $Cr_2O_3$  scale produced in the sulfur-containing atmospheres is not the same as that in the oxidizing atmosphere. Even though the  $Cr_2O_3$  scale was only formed on the alloy surface in the sulfur-containing atmospheres at the early stage of oxidation, it did not work properly as a protective layer for resistance to sulfur attack. For instance, the  $Cr_2O_3$  scale produced by 100 hours oxidation in air exhibited excellent resistance to sulfur attack in the next 500 hours oxidation in the sulfur-containing atmospheres. Meanwhile, the  $Cr_2O_3$  scale produced by oxidation in the sulfur-containing atmosphere was easily broken down by subsequent oxidation in the sulfur-containing atmosphere. Theoretically, within the solubility limit, the sulfur will be dissolved in the oxide according to Sievert's law which states that the amount of the dissolved sulfur is proportional to the square root of sulfur partial pressure. Table 21 reports that the solubility of sulfur in  $Cr_2O_3$  is about 9.0 wt.%. However, comparison with the other oxides indicated that solubility values measured by electron probe analysis appear to be systematically too large by a considerable amount. If the sulfur was dissolved in the compact  $Cr_2O_3$  scale, the defect structure of  $Cr_2O_3$  would be altered. The possible defect structure change in  $Cr_2O_3$  induced by sulfur depends on the nature and location of the sulfur ion within the solid solution. As an instance, Wagner et al<sup>44-45</sup> has suggested that a  $S^-$  ion could be present on an anion site as an electron donor in  $Cr_2O_3$ , thereby increasing the Cr defect concentration through decreasing the hole concentration. Defect concentrations of the Cr-oxide in the sulfur-containing atmospheres are higher.

The another possible explanation for the chemical breakdown of the protective  $Cr_2O_3$  scale induced by sulfur is that micropores in the  $Cr_2O_3$  scale produced in the sulfur-containing atmospheres increase the permeability for the easy movement of gas

molecules through the scale. The fracture section of Cr-rich oxide scale in the sulfur-containing environment was more porous than that in a merely oxidizing environment, as already shown in Figure 29. A possible mechanism of micropore formation is illustrated in Figure 56. If sulfide present in the Cr-rich oxide scale reacts with oxygen, porous  $Cr_2O_3$  would be formed within the scale by volume difference between CrS and  $Cr_2O_3$ . For the chemical breakdown, the overall mechanism would be controlled still by the diffusion of cation and oxidant, or by the combination of both the phase boundary reaction and the diffusion.

Once the internal Cr-rich sulfide particles are formed in the underlying alloy, they coarsen at the front of the chromium-depleted zone, and are followed by oxide intrusions. The local chromium depletion in the underlying alloy as a consequence of Cr-rich sulfide precipitation and coarsening would disturb the mass balance of chromium outward flux across the scale-alloy interface. The supply of chromium from the base alloy to the scale is diminished, and becomes more susceptible to further accelerated oxidation. After the internal Cr-rich sulfide particles form in the underlying alloy, the  $Cr_2O_3$  scale separates gradually as a double-layer composed of an outer Fe-oxide and an inner Cr-rich oxide, as shown in Figure 17. At this point, the growth kinetics deviate slightly from parabolic behavior. It is experimentally difficult to visualize the exact mechanism whereby the iron ions pass through the thin  $Cr_2O_3$  film to form an outer Fe-oxide *layer*<sup>46</sup>. One possible explanation is that the outward diffusion of the noble metal cation through the  $Cr_2O_3$  would be enhanced eventually by the sulfides within the scale.  $Cr_2O_3$  itself grows by outward diffusion of chromium along short-circuit diffusion paths such as grain boundaries of the oxide, as can be predicted from Figure 53. The rates of diffusion through the sulfides are *high*<sup>47</sup>. In addition to the sulfide itself, the incoherent phase boundary between the sulfide precipitates and the Cr-oxide matrix could be paths for enhanced diffusion. Once the two-layer scale

composed of an outer Fe-oxide and an inner Cr-oxide was formed, it grew faster than the Cr-oxide scale showing a linear growth rate.

If the thickness of scale exceeds a critical value, the scale would be broken down by impressed strain. As given in Table 9 and schematically represented in Figure 59<sup>48</sup>, the mechanical failure of the scale could be induced by the sulfide formation/cracking phenomena at the premature onset of breakthrough in the sulfur-containing environments. The sulfide has a high volume *ratio*<sup>47</sup>, which can cause severe stresses locally inside the scale and lead to breaking-up of the scale. Microcracks appear to be created more likely along the grain boundaries of scale. If sulfur was adsorbed at the microcrack surface, then it could induce the rapid crack growth, and also lead to spontaneous cracks by building up more stresses by the following inward movement of *oxidant*<sup>48</sup>. The protective  $Cr_2O_3$  scale would be broken down chemically/mechanically by the sulfide-initiated cracking. In case of the chemical/mechanical breakdown by cracking in the presence of sulfur, the overall mechanism could be controlled by the phase boundary reaction between the corrosive gas and solid at the scale-alloy *interface*<sup>50</sup>. If the two-layer scale composed of an outer Fe-oxide and an inner Cr-oxide is broken down, the oxidant would diffuse inward rapidly and form the nodule composed of an outer Fe-oxide and an inner mixed Fe-Cr oxide. Once the thick two-layer scale consisting of an outer Fe-oxide and an inner mixed Fe-Cr oxide was formed, the remaining Cr-oxide scale would be broken down completely by the sideways growth of the thick two-layer scale. Even though an innermost thin Cr-rich oxide layer was formed afterwards, it did not work as a protective barrier to sulfur penetration. Discrete Cr-rich sulfide particles were observed below the regenerated thin Cr-rich oxide layer, and advanced inward in the underlying alloy, and subsequently cause the severe degradation of structural material. As far as the suppression of sulfide formation is concerned, the  $Cr_2O_3$  scale formed by preoxidation could delay the sulfur

penetration efficiently, but would be broken down eventually.

## 6. Conclusions

- (1) The sulfur activities in the low oxygen partial pressure locations in the fluidized bed combustor lie along the  $CaSO_4/CaO$  equilibrium line, and the maximum sulfur pressure is that corresponding to the  $CaSO_4/CaO/CaS$  triple point. The calcium sulfate coupled with local low oxygen activities induces sulfidation/oxidation corrosion. The formation of internal Cr-rich sulfide/oxide particles in the underlying alloy below an inner Cr-rich oxide layer is a common observation, both in the crucible test and the test in the simulated mixed gas atmosphere. The reaction products formed at the external surface of the scale on iron-chromium alloys by a solid state reaction with the calcium-containing species, such as a eutectic oxide mixture of  $CaO$  and  $Cr_2O_3$  appear to be insignificant in controlling the overall degradation process.
- (2) The development of internal sulfides leads to internal oxidation, fragmentation of the noble metal in the scale, instability of the interface between the scale and alloy, and finally the inability of the alloy to regenerate protective oxide.
- (3) Although the sulfur activity in the atmosphere is important in determining whether or not sulfidation/oxidation took place, the development of the attack is much more sensitive to the actual  $SO_2$  partial pressure. Sulfidation/oxidation is a breakaway process. After breakaway, the metal oxidizes to form non-protective characteristic two-layer oxide scales.
- (4) The deleterious effect of sulfur is related to its inducing a microstructure which prevents the maintenance and the reformation of a protective external scale. The "critical microstructure" developed by the formation of the internal

sulfides/oxides in the underlying alloy leads to breakaway oxidation. The development of a "critical microstructure" involves sulfur transport through the initial protective chromium oxide scale, the formation of internal sulfides, and the internal oxidation of the sulfides.

- (5) Sulfur appears to be transported through the protective chromium oxide scale along short-circuit diffusion paths such as grain boundaries, microcracks or pores. These last two paths appear to be more likely, and involve the molecular penetration of sulfur-bearing species such as  $SO_2$ .
- (7) Sulfur seems to diffuse along the grain boundaries and/or through the bulk in the alloy probably down the concentration gradient of chromium. Preferential penetration of sulfur along the grain boundaries of the small grained binary Fe-Cr alloys was not observed, though the small grained specimens with increased grain boundary areas corroded more severely than the coarse grained.
- (8) The front of internal sulfides leads to accelerated internal oxidation i.e. rapid oxidation of internal sulfides themselves and subsequent inward movement of the liberated sulfur. In other words, the front of internal sulfidation advances into the alloy, both inwards and sideways, followed by in-situ oxidation of the chromium-rich sulfides, producing oxide intrusions. The sulfur released does not appear to escape to the atmosphere. The liberated sulfur forms the new sulfides ahead of internal oxidation in the underlying alloy. Once a critical microstructure develops, a reaction which is a self-sustaining process will take off.

## 7. References.

1. D.P.Whittle, LBL Annual report LBL-8580, 1978
2. G.C.Wood and D.P.Whittle, *Corr. Sci.* 4(1964)263
3. G.C.Wood and D.P.Whittle, *Corr. Sci.* 7(1967)763
4. J.Stringer and S.Ehrlich, "High temperature corrosion in fluidized bed combustors." ASME Annual Meeting, December, 1976, paper no 76-WAS/CD-4
5. M.J.Cooke, A.J.B.Cuttler and E.Raask, *J. Inst. Fuel*, 45(1972)153
6. A.J.Minchener et al, EPRI Final report CS-1853 Research Project 979-1, May, 1981
7. A.J.Minchener, E.A.Rogers and J.Stringer, The work by NCB and EPRI
8. R.A.Perkins, S.J.Vonk and J.Stringer, EPRI FP-1280 Research Project 979-6, Dec., 1979
9. J.Stringer, "High temperature corrosion in fluidized bed combustion." in *Ash Deposits and Corrosion due to Impurities in Combustion Gases*, ed R.W.Bryers, Hemisphere, Washington,D.C. 1977
10. J.Stringer, "High temperature corrosion problems in the electric power industry and their solution." ed Robert A.Rapp, San Diego, 1981
11. R.A.Perkins, unpublished work
12. H.Akuezue, M.S.Thesis, LBL, Univ. of California, Dec. 1979
13. S.R.J.Saunders, M.K.Hossain, B.Kent and D.M.Loyd, *High temperature technology*, 2(1984)63-73
14. J.Stringer and D.P.Whittle, *Proc. Int. VDG Conf. on Corrosion and Deposition in Power plants*, Essen, June, 1977
15. J.Stringer, K.Mark and J.S.Lin, *Proc. Electrochem. Soc. Sym. on High Tem-*

perature Materials (1983) San Francisco.

16. R.P.Salisbury and N.Birks, *J. Iron Steel Inst.* (1971)534
17. C.S.Giggins and F.S.Pettit, *Oxid. Metals*, 14(1980)363
18. F.S.Pettit, J.A.Goebel and G.W.Goward, *Corr. Sci.*, 9(1969)903-913
19. W.R.Worrell, Invited Talk, Univ. of California, 1983
20. W.F.Chu and A.Rahmel, *Oxid. Metals*, 16(1981)175
21. A.U.Seybolt, *Trans. Met. Soc. AIME*, 242(1968)752
22. W.C.Hagel, *J. Am. Cer. Soc.* 48(1965)70
23. K.P.Lillard and P.Kofstad, *J. Electrochem. Soc.*, 127(1980)2397-2419
24. A.Atkinson and R.I.Taylor, *AERE-11314*, June, 1984
25. C.Wagner, *Z. Electrochem.*, 63(1959)772
26. R.A.Rapp, *Corrosion*, 21(1965)382
27. M.K.Hossain, *Corr. Sci.*, 19(1979)1031
28. C.Fillastre, N.Barbouth and J.Oudar, *Scripta Metallurgia*, 16(1982)537-540
29. J.Oudar and N.Barbouth, *Scripta Metallurgia*, 15(1981)41-43
30. P.Risse, M.S.Thesis, LBL, Univ. of California, May, 1981
31. C.J.Spengler and R.Viswanathan, *Met. Trans.*, 3(1972)161
32. M.E.Eldahashan, D.P.Whittle and J.Stringer, *Oxid. Metals*, (1974)179-209, 211-226
33. J.O.Edstroem, *J. Iron Steel Inst.*, 185(1957)450
34. D.P.Whittle, G.C.Wood, D.J.Evans and D.B.Scully, *Acta. Met.*, 15(1967)1747-1755
35. A.U.Seybolt, *J. Electrochem. Soc.*, 107(1960)147

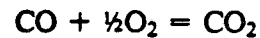


36. H.H.Kellogg, Trans. Met. Soc., AIME, 230(1964)1622
37. I.Barin, O.Knacke and O.Kubaschewski, "Thermochemical properties of Inorganic substances." Springer-Verlag, New York, 1973, 1977
38. J.Stringer, Private communication
39. J.Stringer, "The importance of short-circuit and related transport processes in high-temperature oxidation." pp495-517, "Defects and Transport in Oxides." ed. M.S.Seltzer and R.I.Jaffee, Plenum Press, 1974
40. R.A.Perkins, Final report to EPRI on Contract RP 979-6, 1978
41. W.A.Hagel and A.U.Seybolt, J. Electrochem. Soc., 108(1961)1146
42. L.C.Walters and R.E.Grace, J. Appl. Phys., 8(1968)2331
43. Corrosion, Volume 1, Metal/Environment Reactions, 2nd ed. edited by L.L.Shreir, Butterworth Inc, 1976
44. D.R.Chang, R.Nemoto and J.B.Wagner, Jr., Met. Trans., 7A(1976)803
45. G.Romeo, H.S.Spacil and W.J.Pasko, J.Electrochem. Soc., 122(1975)1329
46. G.R.Wallwork, Rep. Prog. Phys., 39(1976)401
47. Karl Haufe, "Oxidation of Metals.", Plenum Press. (1965)366
48. M.I.Manning et al, EPRI report FP-686, Feb., 1978
49. Y.Ikeda and K.Nii, Oxid. Met. 12(1978)487
50. K.R.Lawless, Rep. Prog. Phys. 37(1974)231

## 8. APPENDIX

### 8.1. Calculation of the local $P_{O_2}$ and $P_{S_2}$ inside the powder bed.

#### (1) Calculation of the oxygen partial pressure in the CO-CO<sub>2</sub> gas mixture.



$$\text{At 1223 K, } \log P_{O_2} = -15.0 + 2 \log (P_{CO_2}/P_{CO})$$

For initial gas mixture:

$$CO ; 1.2\%$$

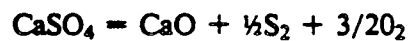
$$CO_2 ; 98.8\%$$

$$P_{CO_2}/P_{CO} = 82.3$$

Thus,

$$\underline{P_{O_2} = 10^{-11.2} \text{ atm}}$$

#### (2) Calculation of the sulfur partial pressure inside the powder bed.



$$\text{At 1223 K, } \log P_{S_2} = -37.8 - 3 \log P_{O_2}$$

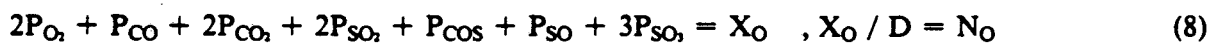
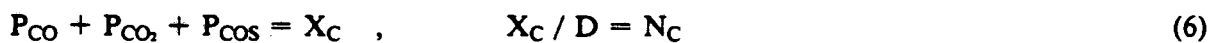
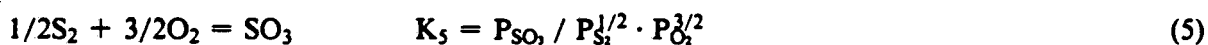
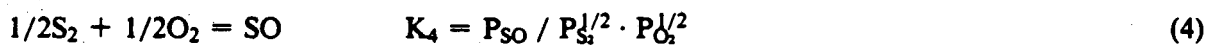
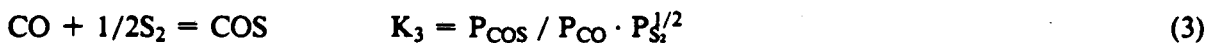
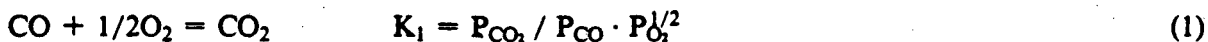
For a fixed oxygen partial pressure of  $10^{-11.2}$  atm,

$$\underline{P_{S_2} = 10^{-4.2} \text{ atm}}$$

8.2. Calculation of oxygen and sulfur partial pressure in the CO-CO<sub>2</sub>-SO<sub>2</sub>-Ar gas mixtures.

3 components : C, S, O

8 species : O<sub>2</sub>, S<sub>2</sub>, COS, SO, SO<sub>2</sub>, SO<sub>3</sub>, CO, CO<sub>2</sub>



Approximately at 1223 K,

$$\log P_{\text{O}_2} = -15.054 + 2 \log(P_{\text{CO}_2}/P_{\text{CO}})$$

$$\log P_{\text{S}_2} = -23.292 + 2 \log(P_{\text{SO}_2}/P_{\text{O}_2})$$

For initial gas mixtures ; (vol %)

| environment no. | 1     | 2    | 3     | 4     | 5    |
|-----------------|-------|------|-------|-------|------|
| CO              | 0.5   | 0.6  | 0.5   | 2.2   | 0.1  |
| CO <sub>2</sub> | 37.4  | 49.4 | 37.4  | 70.3  | 37.4 |
| SO <sub>2</sub> | 2.58  | 0.80 | 0.25  | 0.44  | 2.6  |
| Ar              | 59.52 | 49.2 | 61.85 | 27.06 | 59.9 |

use certified grade premixed gas cylinder ;

0.3% CO- CO<sub>2</sub>, 1.2% CO- CO<sub>2</sub>, 3.0% CO- CO<sub>2</sub>

1.6% SO<sub>2</sub>- Ar, 4.1% SO<sub>2</sub>- Ar

|                                | 1     | 2     | 3     | 4     | 5     |
|--------------------------------|-------|-------|-------|-------|-------|
| <b>fraction</b>                |       |       |       |       |       |
| X <sub>C</sub>                 | 0.379 | 0.500 | 0.379 | 0.725 | 0.375 |
| X <sub>O</sub>                 | 0.804 | 1.010 | 0.758 | 1.436 | 0.801 |
| X <sub>S</sub>                 | 0.026 | 0.008 | 0.002 | 0.004 | 0.026 |
| <b>determinant</b>             |       |       |       |       |       |
| D                              | 1.210 | 1.518 | 1.139 | 2.166 | 1.202 |
| <b>concentration</b>           |       |       |       |       |       |
| N <sub>C</sub>                 | 0.313 | 0.329 | 0.332 | 0.334 | 0.312 |
| N <sub>O</sub>                 | 0.664 | 0.665 | 0.665 | 0.663 | 0.666 |
| N <sub>S</sub>                 | 0.021 | 0.015 | 0.002 | 0.002 | 0.002 |
| <b>partial pressure</b>        |       |       |       |       |       |
| log P <sub>O<sub>2</sub></sub> | -11.2 | -11.2 | -11.2 | -12.0 | -10.0 |
| log P <sub>S<sub>2</sub></sub> | -4.0  | -5.0  | -6.0  | -4.0  | -6.4  |

Approximately at 1123 K,

$$\log P_{O_2} = -17.202 + 2 \log ( P_{CO_2} / P_{CO} )$$

$$\log P_{S_2} = -26.02 + 2 \log ( P_{SO_2} / P_{O_2} )$$

|                                  |                                | environment no. |       |
|----------------------------------|--------------------------------|-----------------|-------|
|                                  |                                | 6               | 7     |
| initial gas mixtures,<br>(vol %) | CO                             | 0.1             | 0.1   |
|                                  | CO <sub>2</sub>                | 37.4            | 37.4  |
|                                  | SO <sub>2</sub>                | 2.6             | 1.0   |
|                                  | Ar                             | 59.9            | 61.5  |
| fraction,                        | X <sub>C</sub>                 | 0.375           | 0.375 |
|                                  | X <sub>O</sub>                 | 0.801           | 0.769 |
|                                  | X <sub>S</sub>                 | 0.026           | 0.010 |
| determinant,                     | D                              | 1.202           | 1.154 |
| concentration,                   | N <sub>C</sub>                 | 0.312           | 0.325 |
|                                  | N <sub>O</sub>                 | 0.666           | 0.666 |
|                                  | N <sub>S</sub>                 | 0.022           | 0.009 |
| partial pressure,                | log P <sub>O<sub>2</sub></sub> | -12.2           | -12.2 |
|                                  | log P <sub>S<sub>2</sub></sub> | -4.9            | -5.7  |

### 8.3 Approximate calculation of $D_s$ in the scale and alloy.

In Figure 40, the penetration depth of Cr-rich sulfide particles in the underlying alloy was about  $47 \mu\text{m}$ , and the scale thickness measured was about  $20 \mu\text{m}$ .

The previously published diffusion coefficients of sulfur in the Fe-Cr alloys at 1223 K are given in Table 20.

$$D_s \text{ (in Fe-26Cr)} = 1.5 \times 10^{-9} \text{ cm}^2 / \text{sec (T = 1223 K)}$$

The diffusion time of sulfur in alloy can be calculated by using the following equation.

$$\text{penetration depth} = 2 \times (D_s \times \text{time})^{1/2}$$

$$47 \times 10^{-4} = 2 \times (1.5 \times 10^{-9} \times \text{time})^{1/2}$$

$$t = 3682 \text{ sec} = 1 \text{ hour}$$

The minimum elapsed time for diffusion in the alloy is at least 1 hour.

Assuming that the change of scale thickness is negligible during 500 hours oxidation in the low  $P_{\text{O}_2}$  and high  $P_{\text{S}_2}$  atmosphere ( $P_{\text{O}_2} = 10^{-11.2}$ ,  $P_{\text{S}_2} = 10^{-4} \text{ atm}$ ), compared to the 100 hours oxidation in air ( $P_{\text{O}_2} = 0.21 \text{ atm}$ ), since scale grows very slowly in 500 hours oxidation.

The maximum elapsed time for diffusion in  $\text{Cr}_2\text{O}_3$  is about 499 hours. The scale thickness measured is about  $20 \mu\text{m}$ .

$$20 \times 10^{-4} = 2 \times (D_s \times 499 \times 3600)^{1/2}$$

$$D_s = 5.5 \times 10^{-13} \text{ cm}^2 / \text{sec}$$

The minimum estimated value of the sulfur diffusion coefficient in  $\text{Cr}_2\text{O}_3$  is about  $5.5 \times 10^{-13} \text{ cm}^2/\text{sec}$  at 1223 K.

*Acknowledgement*

I extend my deepest gratitude to Dr. John Stringer for his guidance and many valuable suggestions throughout this study. I would also like to extend my sincere thanks to Professor Alan W. Search for his guidance and encouragement during the course of the work. I am very grateful to Professor D. P. Whittle\* for his support and guidance during this research. I also wish to express my sincere thanks to Professor Leo Brewer and Professor J. W. Evans for many useful suggestions. Thanks are also extended to the technical staff of the LBL, who in many ways contributed towards the completion of this work.

This work was supported by the Office of Basic Energy Science, U.S. Department of Energy under contract number DE-AC03-76SF00098.

---

\*deceased

Table 1. Chemical compositions of alloys tested.

(unit; weight percentage)\*

| nominal<br>composition | Fe    | Cr    |
|------------------------|-------|-------|
| Fe-15Cr                | 84.40 | 15.60 |
| Fe-18Cr                | 81.82 | 18.18 |
| Fe-20Cr                | 79.24 | 20.76 |
| Fe-25Cr                | 74.22 | 25.78 |
| Fe-30Cr                | 69.63 | 30.37 |

\* analyzed in EDX.



Table 2. Experimental conditions in crucible test.

|  |   |  |
|--|---|--|
| alloys tested                                      | : | Fe-15Cr, Fe-20Cr, Fe-25Cr  |
| temperature  | : | 1223 K   |
| external environment                               | : | 1.2% CO - 98.8% CO <sub>2</sub> ,<br>P <sub>O<sub>2</sub></sub> = 10 <sup>-11.2</sup> atm              |
| gas flow rate                                      | : | 0.1 cm/sec   |
| powder bed   | : | CaSO <sub>4</sub> /CaO<br>(38 mm diameter × 38 mm height)  |
| environment inside bed*<br>(near specimen surface) | : | P <sub>O<sub>2</sub></sub> = 10 <sup>-11.2</sup> , P <sub>S<sub>i</sub></sub> = 10 <sup>-4.5</sup> atm |
| duration   | : | 25, 50, 100, 150, 200 hours  |

\* thermodynamically calculated value.

Table 3. Experimental results in crucible test.

| alloy   | duration<br>hours | weight<br>gain<br>mg/cm <sup>2</sup> | scale thickness<br>μm |           | penetration<br>depth<br>μm | scaling characteristics  |
|---------|-------------------|--------------------------------------|-----------------------|-----------|----------------------------|--|
|         |                   |                                      | typical               | two-layer |                            |  |
| Fe-25Cr | 25                | 1.87                                 | 2                     | ---       | 0                          | Cr <sub>2</sub> O <sub>3</sub>   |
|         | 50                | 2.84                                 | 5-8                   | ---       | 0                          | (Cr,Fe) <sub>2</sub> O <sub>3</sub> , CaO + Cr <sub>2</sub> O <sub>3</sub> |
|         | 100               | 3.10                                 | 7-10                  | ---       | 0                          | "  |
|         | 150               | 3.14                                 | 12-15                 | ---       | 0                          | "  |
|         | 200               | 6.42                                 | 14-15                 | ---       | 0                          | "  |
| Fe-20Cr | 25                | 0.84                                 | 2                     | ---       | 0                          | Cr <sub>2</sub> O <sub>3</sub>   |
|         | 50                | 1.37                                 | 5-7                   | ---       | 0                          | (Cr,Fe) <sub>2</sub> O <sub>3</sub> , CaO + Cr <sub>2</sub> O <sub>3</sub> |
|         | 100               | 2.07                                 | 6-8                   | ---       | 0                          | (Cr,Fe) <sub>2</sub> O <sub>3</sub> , CaO + Fe <sub>2</sub> O <sub>3</sub> |
|         | 150               | 28.26                                | 13-18                 | 1000      | 10-20                      | internal sulfidation   |
|         | 200               | 100.8                                | 15-20                 | 2000      | 20-30                      | "  |
| Fe-15Cr | 25                | 455.7                                | *                     | *         | *                          | all oxidized   |
|         | 50                | 451.0                                | *                     | *         | *                          | "  |

Table 4. Characterization of corrosion products.

| <i>Morphology</i>                   | <i>Structure</i>         | <i>Analysis</i>                     |
|-------------------------------------|--------------------------|-------------------------------------|
| <b>Visual examination</b>           | <b>X-ray diffraction</b> | <b>Chemical analysis</b>            |
| - general appearance                | - structure              |                                     |
| - colour                            | - preferred orientation  |                                     |
| - uniformity                        |                          | <b>Electron probe microanalysis</b> |
| - spalling etc.                     |                          | -Dispersive                         |
| <b>Optical microscopy</b>           |                          | - composition                       |
| - local thickness                   |                          | - diffusion profiles                |
| - topography                        |                          |                                     |
| - general morphology                |                          | <b>Auger electron spectrometry</b>  |
| - internal corrosion                |                          | - analysis                          |
| <b>Scanning electron microscopy</b> |                          | - diffusion profiles                |
| - thickness                         |                          |                                     |
| - morphology                        |                          |                                     |
| - porosity                          |                          |                                     |
| - fracture sections                 |                          |                                     |

Table 5. *Experimental conditions in the mixed gas atmospheres.*

Alloys tested : Fe-30Cr, Fe-25Cr, Fe-20Cr, Fe-18Cr, Fe-15Cr

| environment<br>no. | gas mixture, vol. % |                 |                 |      | calc., atm                     |                                | duration, hours         | temperature<br>K |
|--------------------|---------------------|-----------------|-----------------|------|--------------------------------|--------------------------------|-------------------------|------------------|
|                    | CO                  | CO <sub>2</sub> | SO <sub>2</sub> | Ar   | log P <sub>O<sub>2</sub></sub> | log P <sub>S<sub>2</sub></sub> |                         |                  |
| 1                  | 0.5                 | 37.4            | 2.6             | 59.5 | -11.2                          | -4.0                           | 25, 50, 100, 150        | 1223             |
| 2                  | 0.6                 | 49.4            | 0.8             | 49.2 | -11.2                          | -5.0                           | 25, 50, 100, 165<br>200 |                  |
| 3                  | 0.5                 | 37.4            | 0.2             | 61.9 | -11.2                          | -6.0                           | 100, 200                |                  |
| 4                  | 2.2                 | 70.3            | 0.4             | 27.1 | -12.0                          | -4.0                           | 100, 200                |                  |
| 5                  | 0.1                 | 37.4            | 2.6             | 59.9 | -10.0                          | -6.4                           | 100, 200                |                  |
| 6                  | 0.1                 | 37.4            | 2.6             | 59.9 | -12.2                          | -4.9                           | 100, 200                | 1123             |
| 7                  | 0.1                 | 37.4            | 1.0             | 61.5 | -12.2                          | -5.7                           | 100                     |                  |

Table 6. Experimental results in the mixed gas atmospheres at 1223 K.

| environment,<br>gas pressures<br><br>in atm                                    | alloy  | duration<br><br>hours | weight<br>gain<br><br>mg/cm <sup>2</sup> | scale thickness<br>μm |           | penetration<br>depth<br><br>μm                            | scaling characteristics  |                                |
|--|--|-----------------------|--|-----------------------|-----------|---|--|--------------------------------|
|  |  |                       |  | typical               | two-layer |   |  |                                |
| 1<br><br>$P_{O_2}=10^{-11.2}$<br><br>$P_{S_2}=10^{-4}$<br><br>$P_{SO_2}=0.026$ | Fe-30Cr  | 50                    | -0.85                                    | 16-24                 | —         | 10-16   | Cr <sub>2</sub> O <sub>3</sub> , internal sulfid.  |                                |
|  | Fe-25Cr  | 25                    | 2.04                                     | 13-15                 | 24-31     | 20-25   | Cr <sub>2</sub> O <sub>3</sub> , Fe-/Cr-oxide, sulfid. M <sub>2</sub> O <sub>3</sub> -type |                                |
|  |  | 50                    | 1.41                                     | 10-15                 | 35-50     | 35-40   | Cr <sub>2</sub> O <sub>3</sub> , Fe-/Cr-oxide, sulfid. "                                   |                                |
|  | Fe-20Cr  | 100                   | 3.01                                     | 11-16                 | 30-50     | 15-40   | Cr <sub>2</sub> O <sub>3</sub> , Fe-/Cr-oxide, sulfid. "                                   |                                |
|  |  | 150                   | -7.03                                    | 10-26                 | 20-60     | 20-40   | Cr <sub>2</sub> O <sub>3</sub> , Fe-/Cr-oxide, sulfid. "                                   |                                |
|  | Fe-18Cr  | 25                    | 2.46                                     | 4-14                  | 14        | 15  | Cr <sub>2</sub> O <sub>3</sub>   |                                |
|  |  | 50                    | 1.82                                     | 4-16                  | 16-26     | 14-20   | Cr <sub>2</sub> O <sub>3</sub> , Fe-/Cr-oxide, sulfid. M <sub>2</sub> O <sub>3</sub> -type |                                |
|  |  | 100                   | 2.54                                     | 5-25                  | 14-35     | 12-23   | Cr <sub>2</sub> O <sub>3</sub> , Fe-/Cr-oxide, sulfid. "                                   |                                |
|  |  | 150                   | 44.18                                    | 42                    | 1000      | 50  | Cr <sub>2</sub> O <sub>3</sub> , Fe-/Cr-oxide, sulfid. "<br>thick Fe-/Fe-Cr oxide nodule   |                                |
|  | Fe-15Cr  | 100                   | 194.3                                    | 6-10                  | 1000      | 40  | nearly all of metal consumed   |                                |
|  |  | 25                    | 120.7                                    | 550                   | 1000      | 15  | Fe-/Fe-Cr-oxide, sulfid.   |                                |
|  |  | 50                    | 189.2                                    | 600                   | 900       | 80  | Fe-/Fe-Cr-oxide, sulfid.   |                                |
|  | 2<br><br>$P_{O_2}=10^{-11.2}$<br><br>$P_{S_2}=10^{-5}$<br><br>$P_{SO_2}=0.008$ | Fe-30Cr               | 100                                      | 240.2                 | •         | •   | •  | all metal consumed             |
|  |  |                       | 200                                      | 0.31                  | 10-13     | —   | 0  | Cr <sub>2</sub> O <sub>3</sub> |
|  |  | Fe-25Cr               | 25                                       | 0.63                  | 5         | —   | 0  | Cr <sub>2</sub> O <sub>3</sub> |
| 50   |  |                       | 1.15                                     | 6-7                   | —         | 0   | "  |                                |
| 100  |  |                       | 1.67                                     | 9-10                  | —         | 0   | "  |                                |
| 165  |  |                       | -1.65                                    | 12                    | —         | 0   | "  |                                |
| 200  |  |                       | 2.83                                     | 16-18                 | —         | 0   | "  |                                |
| Fe-20Cr  |  | 25                    | 0.63                                     | 4                     | —         | 0   | Cr <sub>2</sub> O <sub>3</sub>   |                                |
|  |  | 50                    | 1.19                                     | 5-6                   | —         | 0   | "  |                                |
|  |  | 100                   | 1.35                                     | 8-9                   | —         | 0   | "  |                                |
|  | 165  | 2.67                  | 12-14                                    | —                     | 0         | "   |  |                                |
|  | 200  | 1.80                  | 12-18                                    | 700                   | 12-20     | Cr <sub>2</sub> O <sub>3</sub> , two-layer at corner only |  |                                |

Table 6. continued:

| environment<br>gas pressures<br><br>in atm                               | alloy   | duration,<br><br>hours | weight<br>gain<br><br>mg/cm <sup>2</sup> | scale thickness<br>μm |           | penetration<br><br>μm          | scaling characteristics  |
|--|---------|------------------------|--|-----------------------|-----------|--------------------------------|--|
|  |         |                        |  | typical               | two-layer |                                |  |
| 3<br><br>$P_{O_2}=10^{-11.2}$<br>$P_{S_2}=10^{-6}$<br>$P_{SO_2}=0.002$   | Fe-18Cr | 100                    | 1.15                                     | 5-6                   | —         | 0                              | Cr <sub>2</sub> O <sub>3</sub>   |
|  |         | 200                    | 290.5                                    | •                     | •         | •                              | all metal consumed   |
|  | Fe-15Cr | 25                     | 64.45                                    | 250-450               | 600       | 20                             | Fe-/Fe-Cr-oxide  |
|  |         | 50                     | 225.2                                    | •                     | •         | •                              | all metal consumed   |
|  | Fe-30Cr | 100                    | -0.35                                    | 10-12                 | —         | 0                              | Cr <sub>2</sub> O <sub>3</sub>   |
|  |         | 200                    | -0.18                                    | 10-12                 | —         | 0                              | •  |
| Fe-25Cr  | 100     | -1.19                  | 7-8                                      | —                     | 0         | Cr <sub>2</sub> O <sub>3</sub> |  |
|  | 200     | -2.99                  | 16-18                                    | —                     | 0         | •                              |  |
| Fe-20Cr  | 100     | 1.47                   | 6-7                                      | —                     | 0         | Cr <sub>2</sub> O <sub>3</sub> |  |
|  | 200     | 1.41                   | 7-10                                     | —                     | 0         | •                              |  |
| 4<br><br>$P_{O_2}=10^{-12.0}$<br>$P_{S_2}=10^{-4}$<br>$P_{SO_2}=0.004$   | Fe-30Cr | 200                    | -4.98                                    | 16-18                 | —         | 0                              | Cr <sub>2</sub> O <sub>3</sub>   |
|  |         | Fe-25Cr                | 100                                      | 0.40                  | 5-9       | —                              | 0  |
|  | 200     |                        | -1.97                                    | 12-16                 | —         | 0                              | •  |
|  | Fe-20Cr | 100                    | 1.31                                     | 3-7                   | —         | 0                              | Cr <sub>2</sub> O <sub>3</sub>   |
|  |         | 200                    | 109.3                                    | 7-8                   | 1000      | 10-12                          | Cr <sub>2</sub> O <sub>3</sub> , catastrophic corrosion at ends.                           |
|  | Fe-18Cr | 100                    | 282.4                                    | •                     | •         | •                              | all metal consumed   |
| 5<br><br>$P_{O_2}=10^{-10.0}$<br>$P_{S_2}=10^{-6.6}$<br>$P_{SO_2}=0.026$ | Fe-25Cr | 100                    | -2.54                                    | 10-12                 | 60        | 30-40                          | Cr <sub>2</sub> O <sub>3</sub> , Fe-/Cr-oxide, sulfid. M <sub>2</sub> O <sub>3</sub> -type |
|  | Fe-20Cr | 100                    | 1.03                                     | 4-6                   | 10-18     | 10-15                          | Cr <sub>2</sub> O <sub>3</sub> , Fe-/Cr-oxide, slight sulfid.                              |
|  | Fe-18Cr | 100                    | 199.6                                    | •                     | •         | •                              | all metal consumed   |

Table 7. Scaling characteristics in the sulfidation/oxidation type corrosive environment.

(  $P_{O_2} = 10^{-11.2}$ ,  $P_{S_2} = 10^{-4}$  atm )

|   | Fe-20Cr  | Fe-15Cr                             |
|---|--|-------------------------------------|
| spalling tendency                             | light  | heavy                               |
| progress of internal sulfidation              | late   | early                               |
| formation of an outer Fe-oxide above Cr-oxide | common after internal sulfidation              |                                     |
| breakdown behavior                            | susceptible to <sup>*</sup> chemical breakdown | susceptible to mechanical breakdown |
| accelerated corrosion                         | rapid <sup>**</sup>                            | slow                                |

\* susceptible to chemical breakdown after failure of initial  $Cr_2O_3$  scale, even if good protective behavior at the early stage with good resistance to mechanical breakdown

\*\* by forming the thick two-layer scale composed of an outer Fe-oxide, an inner Fe-Cr oxide, and an innermost thin Cr-rich oxide.

Table 8. The extent of corrosive attack in the high  $P_{S_2}$  environment.

( $P_{O_2} = 10^{-11.2}$ ,  $P_{S_2} = 10^{-4}$  atm)

| alloy   | duration<br>hours | scale thickness<br>$\mu\text{m}$ |          |       | penetration<br>depth<br>$\mu\text{m}$ | extent of<br>corrosion |
|---------|-------------------|----------------------------------|----------|-------|---------------------------------------|------------------------|
|         |                   | Fe-oxide                         | Cr-oxide | total |                                       |                        |
| Fe-20Cr | 100               | 10                               | 25       | 35    | 23                                    | L                      |
|         | 150               | 12                               | 30       | 42    | 50                                    | S                      |
| Fe-25Cr | 100               | 15                               | 35       | 50    | 40                                    | M                      |
|         | 150               | 23                               | 30       | 53    | 40                                    | M                      |

\* severe: S  
medium: M  
little: L



Table 9. The critical thickness of  $\text{Cr}_2\text{O}_3$  scale in the sulfur-containing environment.

$P_{\text{O}_2} = 10^{-11.2}$  atm

alloy tested : Fe-20Cr

| environment |                         | duration<br>hours | weight<br>gain<br>mg/cm <sup>2</sup> | scale thickness<br>$\mu\text{m}$ |                    | penetration<br>depth<br>$\mu\text{m}$ | scale<br>breakdown | sulfid. |
|-------------|-------------------------|-------------------|--------------------------------------|----------------------------------|--------------------|---------------------------------------|--------------------|---------|
| no.         | $P_{\text{S}_2}$<br>atm |                   |                                      | typical                          | thick<br>two-layer |                                       |                    |         |
| 1           | $10^{-4}$               | 50                | 1.82                                 | 4-6/<br>16-26                    | —                  | 14-20                                 | Yes                | Yes     |
|             |                         | 150               | 44.18                                | 42*                              | 1000               | 50                                    | Yes                | Yes     |
| 2           | $10^{-5}$               | 100               | 1.35                                 | 8-9                              | —                  | —                                     | No                 | No      |
|             |                         | 165               | 2.67                                 | 12-14                            | —                  | —                                     | No                 | No      |

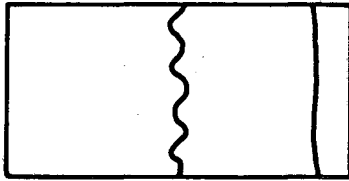
\* Fe-oxide: 12  $\mu\text{m}$   
total: 42  $\mu\text{m}$   
Cr-oxide: 30  $\mu\text{m}$

Table 10. Corrosion Type

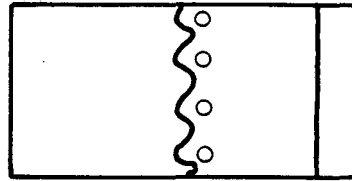
| temperature<br>K | environment |                                    | Cr-content in Fe-Cr alloy        |                             |                        |                   |                        |
|------------------|-------------|------------------------------------|----------------------------------|-----------------------------|------------------------|-------------------|------------------------|
|                  | no.         | P <sub>SO<sub>2</sub></sub><br>atm | 15                               | 18                          | 20                     | 25                | 30                     |
| 1223             | 1           | 0.026                              | very rapid oxid./<br>sulfidation | rapid oxid./<br>sulfidation | oxid./<br>sulfid.      | oxid./<br>sulfid. | slow oxid./<br>sulfid. |
|                  | 5           | 0.026                              | *                                | rapid oxid./<br>sulfid.     | oxid./<br>sulfid.      | oxid./<br>sulfid. | *                      |
|                  | 2           | 0.008                              | very rapid oxid./<br>sulfidation | rapid oxid./<br>sulfidation | oxid./<br>slow sulfid. | slow oxid.        | slow oxid.             |
|                  | 4           | 0.004                              | very rapid oxid./<br>sulfidation | rapid oxid./<br>sulfidation | oxid./<br>slow sulfid. | slow oxid.        | slow oxid.             |
|                  | 3           | 0.002                              | very rapid oxid./<br>sulfidation | *                           | oxidation              | slow oxid.        | slow oxid.             |
| 1123             | 6           | 0.026                              | rapid oxid./<br>sulfid.          | *                           | oxid./<br>sulfid.      | oxid./<br>sulfid. | slow oxid.             |
|                  | 7           | 0.010                              | oxidation                        | *                           | slow oxid.             | slow oxid.        | slow oxid.             |

Table 11. Schematic representation of the variation in the attack modes in the sulfidation/oxidation corrosion on iron-chromium alloys.

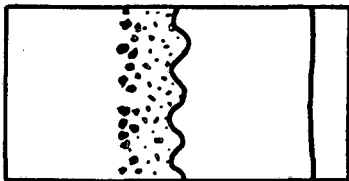
| temperature<br>K | environment<br>no. | Cr-Content in Fe-Cr alloy |        |           |         |     |
|------------------|--------------------|---------------------------|--------|-----------|---------|-----|
|                  |                    | 15                        | 18     | 20        | 25      | 30  |
| 1223             | 1                  | 2,4,6                     | 3,4,6, | 2,3,4,5,6 | 2,3,4,5 | 2,3 |
|                  | 5                  | *                         | 4,6    | 2,3,4,5   | 2,3,4,5 | *   |
|                  | 2                  | 4,6                       | 4,6    | 2,3       | 2       | 2   |
|                  | 4                  | 4,6                       | 4,6    | 1,3       | 1       | 2   |
|                  | 3                  | 4,6                       | *      | 1         | 1       | 2   |
| 1123             | 6                  | *                         | *      | 3,4,5     | 3,4,5   | 2   |
|                  | 7                  | 1                         | *      | 1         | 1       | 1   |



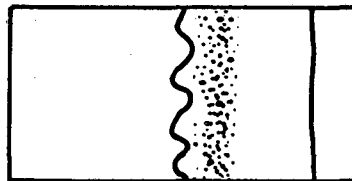
1. Irregular interface.



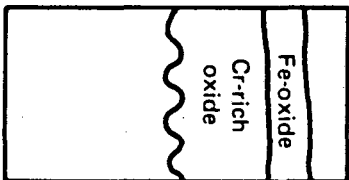
2. Pure base metal within scale.



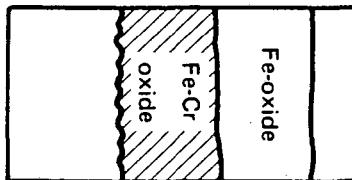
3. Internal sulfide/oxide particles.



4. Sulfur-enriched in Cr-oxide scale.



5. Two layered scale.



6. Thick two-layer scale.

Table 11(continued).

XBL 856-10039

Table 12. Experimental results in the mixed gas atmospheres at 1123 K.

alloys tested : Fe-30Cr, Fe-25Cr, Fe-20Cr

| environment,<br>gas pressures<br><br>in atm                                      | alloy   | duration<br><br>hours | weight<br>gain<br><br>mg/cm <sup>2</sup> | scale thickness<br>μm |                   | penetration<br>depth<br><br>μm | scaling characteristics  |
|--|---------|-----------------------|--|-----------------------|-------------------|--------------------------------|--|
|  |         |                       |  | typical               | two-layer         |                                |  |
| 6<br><br>$P_{O_2}=10^{-12.2}$<br><br>$P_{S_2}=10^{-4.9}$<br><br>$P_{SO_2}=0.026$ | Fe-30Cr | 200                   | 0.47                                     | 8-12                  | —                 | 0                              | Cr <sub>2</sub> O <sub>3</sub>   |
|  | Fe-25Cr | 200                   | 4.87                                     | 8-14                  | 50-90             | 20-30                          | Cr <sub>2</sub> O <sub>3</sub> , Fe-oxide/Cr-rich oxide<br>Internal sulfid., M <sub>2</sub> O <sub>3</sub> -type |
|  | Fe-20Cr | 200                   | 7.81                                     | 6-12                  | 35-75/<br>110-130 | 20-30                          | Cr <sub>2</sub> O <sub>3</sub> , Fe-oxide/Cr-rich oxide<br>Internal sulfid., M <sub>2</sub> O <sub>3</sub> -type |
| 7<br><br>$P_{O_2}=10^{-12.2}$<br><br>$P_{S_2}=10^{-5.7}$<br><br>$P_{SO_2}=0.010$ | Fe-30Cr | 100                   | 0.50                                     | 3-5                   | —                 | 0                              | Cr <sub>2</sub> O <sub>3</sub>   |
|  | Fe-25Cr | 100                   | 0.34                                     | 3-4                   | —                 | 0                              | Cr <sub>2</sub> O <sub>3</sub>   |
|  | Fe-20Cr | 100                   | 0.83                                     | 2-3                   | —                 | 0                              | Cr <sub>2</sub> O <sub>3</sub>   |

Table 13. Experimental conditions; Transport of sulfur.

Corrosion type : preoxidation in air, and oxidation  
in the CO-CO<sub>2</sub>-SO<sub>2</sub> gas mixtures.

Alloys tested : Fe-30Cr, Fe-25Cr, Fe-20Cr, Fe-18Cr

Mixed gas environments :

| temperature<br>K | gas mixture, vol.% |                 |                 |      | calc., atm                     |                                |
|------------------|--------------------|-----------------|-----------------|------|--------------------------------|--------------------------------|
|                  | CO                 | CO <sub>2</sub> | SO <sub>2</sub> | Ar   | log P <sub>O<sub>2</sub></sub> | log P <sub>S<sub>2</sub></sub> |
| 1223             | 0.5                | 37.4            | 2.6             | 59.5 | -11.2                          | -4.0                           |
| 1123             | 0.1                | 37.4            | 2.6             | 59.9 | -12.2                          | -4.9                           |

Summary of oxidation runs :

| run<br>no. | duration, hours |       | temperature<br>K | transition between<br>preoxid. & oxidation |
|------------|-----------------|-------|------------------|--|
|            | preoxid.        | oxid. |                  |  |
| 1          | 60              | 100   | 1223             | isothermal                                 |
| 2          | 168             | 100   |                  |  |
| 3          | 50              | 100   |                  | cool to room temperature<br>&<br>heat up   |
| 4          | 100             | 100   |                  |  |
| 5          | 100             | 230   |                  |  |
| 6          | 100             | 500   |                  |  |
| 7          | 100             | 100   | 1123             |  |

Table 14a. Experimental results; oxidation of the preoxidized specimens in the mixed gas atmospheres.

Environment : *preoxid. in air & oxid. in the CO-CO<sub>2</sub>-SO<sub>2</sub> gas mixture.*

*isothermal transition*

Temperature : 1223 K

| alloy   | duration, hours |       | weight gain<br>mg/cm <sup>2</sup> | scale thickness<br>μm |           | penetration<br>depth<br>μm | scaling characteristics        |
|---------|-----------------|-------|-----------------------------------|-----------------------|-----------|----------------------------|--------------------------------|
|         | preoxid.        | oxid. |                                   | typical               | two-layer |                            |                                |
| Fe-30Cr | 60              | 100   | 1.38                              | 6-8                   | ---       | 0                          | Cr <sub>2</sub> O <sub>3</sub> |
|         | 168             | 100   | 1.47                              | 5-7                   | ---       | 0                          | "                              |
| Fe-25Cr | 60              | 100   | 1.22                              | 4-5                   | ---       | 0                          | Cr <sub>2</sub> O <sub>3</sub> |
|         | 168             | 100   | 1.49                              | 6-8                   | ---       | 0                          | "                              |
| Fe-20Cr | 60              | 100   | 1.00                              | 4-6                   | ---       | 0                          | Cr <sub>2</sub> O <sub>3</sub> |
|         | 168             | 100   | 1.33                              | 5-6                   | ---       | 0                          | "                              |

Table 14b.

Environment : *preoxid. in air & oxid. in the CO-CO<sub>2</sub>-SO<sub>2</sub> gas mixture.*

*cool to room temperature & heat up*

| temp.<br>K | alloy   | duration |       | weight gain        |       | scale thickness |           | penetration | scaling characteristics  |
|------------|---------|----------|-------|--------------------|-------|-----------------|-----------|-------------|--|
|            |         | hours    |       | mg/cm <sup>2</sup> |       | μm              |           | depth       |  |
|            |         | preoxid. | oxid. | preoxid.           | oxid. | typical         | two-layer | μm          |  |
| 1223       | Fe-30Cr | 50       | 100   | 0.78               | 0.28  | 5-14            | —         | 0           | Cr <sub>2</sub> O <sub>3</sub>   |
|            | Fe-25Cr | 50       | 100   | 0.78               | 0.39  | 5-16            | —         | 0           | Cr <sub>2</sub> O <sub>3</sub>   |
|            |         | 100      | 100   | 1.05               | 0.24  | 6-10            | —         | 0           | "  |
|            |         | 100      | 230   | 1.15               | 0.30  | 8-12            | —         | 0           | "  |
|            |         | 100      | 500   | 1.05               | 1.05  | 11-15           | —         |             | Cr <sub>2</sub> O <sub>3</sub> , internal Cr-rich sulfide particles          |
|            | Fe-20Cr | 50       | 100   | 0.57               | 0.35  | 4-6             | —         | 0           | Cr <sub>2</sub> O <sub>3</sub>   |
|            |         | 100      | 100   | 0.89               | 0.21  | 4-9             | —         | 0           | "  |
|            |         | 100      | 230   | 0.97               | 0.42  | 8-9             | —         | 0           | "  |
|            |         | 100      | 500   | 1.15               | 1.30  | 9-14            | —         | 0           | "  |
|            | Fe-18Cr | 50       | 100   | 0.59               | 0.44  | 5-7             | 45        | 10-14       | Cr <sub>2</sub> O <sub>3</sub> , thick two-layer at corner only.             |
|            |         | 100      | 230   | 0.65               | 1.93  | 8-13            | 40-50     | 6-18        | Cr <sub>2</sub> O <sub>3</sub> , thick two-layer at corner, internal sulfid. |
|            | 1123    | Fe-30Cr  | 100   | 100                | 0.28  | 0.06            | 1         | —           | 0  |
| Fe-25Cr    |         | 100      | 100   | 0.27               | 0.12  | 1               | —         | 0           | Cr <sub>2</sub> O <sub>3</sub>   |
| Fe-20Cr    |         | 100      | 100   | 0.31               | 0.07  | 1               | —         | 0           | Cr <sub>2</sub> O <sub>3</sub>   |



Table 15. Experimental conditions; Internal sulfidation.

Corrosion type : oxidation in the CO-CO<sub>2</sub>-SO<sub>2</sub> gas mixtures,

Alloys tested : Fe-25Cr (cast and homogenized, cold-rolled and annealed)

Fe-20Cr (cast and homogenized, cold-rolled and annealed)

Fe-18Cr (cast and homogenized, cold-rolled and annealed)

Mixed gas environments :

| temperature<br>K | gas mixture, vol. % |                 |                 |      | calc., atm                     |                                |
|------------------|---------------------|-----------------|-----------------|------|--------------------------------|--------------------------------|
|                  | CO                  | CO <sub>2</sub> | SO <sub>2</sub> | Ar   | log P <sub>O<sub>2</sub></sub> | log P <sub>S<sub>2</sub></sub> |
| 1223             | 0.5                 | 37.4            | 2.6             | 59.5 | -11.2                          | -4.0                           |
|                  | 0.6                 | 49.4            | 0.8             | 49.2 | -11.2                          | -5.0                           |
|                  | 2.2                 | 70.3            | 0.4             | 27.1 | -12.0                          | -4.0                           |

Summary of oxidation runs :

| run no. | duration,<br>hours | environment, atm               |                                |
|---------|--------------------|--------------------------------|--------------------------------|
|         |                    | log P <sub>O<sub>2</sub></sub> | log P <sub>S<sub>2</sub></sub> |
| 1       | 100                | -11.2                          | -4.0                           |
| 2       | 100                | -11.2                          | -5.0                           |
| 3       | 200                | "                              | "                              |
| 4       | 100                | -12.0                          | -4.0                           |
| 5       | 200                | "                              | "                              |

Table 16. Grain size of Fe-Cr alloy ingots after annealed at 1473 K for 24 hours. (Grain boundary was revealed by etching at Vilella's reagent.)

| alloy   | grain size, $\mu\text{m}$ |         |                       |          |
|---------|---------------------------|---------|-----------------------|----------|
|         | cast and homogenized      |         | thermomechanical work |          |
|         | measured                  | average | cold-rolled           | annealed |
| Fe-30Cr | 400-750                   | 530     | —                     | —        |
| Fe-25Cr | 350-700                   | 530     | 4-6                   | 70-100   |
| Fe-20Cr | 320-620                   | 440     | 5-7                   | 50-90    |
| Fe-18Cr | 370-650                   | 500     | 5-8                   | 60-110   |
| Fe-15Cr | 500-800                   | 610     | —                     | —        |

Table 17. Experimental results: oxidation of small grained Fe-Cr alloys in mixed gas atmospheres.

| environment,<br>gas pressures<br>in atm                         | alloy   | duration<br>hours | weight<br>gain<br>mg/cm <sup>2</sup> | scale thickness<br>μm |           | penetration<br>depth<br>μm | scaling characteristics  |
|---|---------|-------------------|--------------------------------------|-----------------------|-----------|----------------------------|--|
|   |         |                   |                                      | typical               | two-layer |                            |  |
| $P_{O_2}=10^{-11.2}$<br>$P_{S_2}=10^{-4.0}$<br>$P_{SO_2}=0.026$ | Fe-25Cr | 100               | -3.71                                | 10-12                 | 30-40     | 30-40                      | Cr <sub>2</sub> O <sub>3</sub> , Fe-oxide/Cr-rich oxide<br>internal sulfid., M <sub>2</sub> O <sub>3</sub> -type   |
|   | Fe-20Cr | 100               | 0.69                                 | 6-7                   | 14-30     | 20-25                      | Cr <sub>2</sub> O <sub>3</sub> , Fe-oxide/Cr-rich oxide<br>internal Cr-rich sulfide, M <sub>2</sub> O <sub>3</sub> |
|   | Fe-18Cr | 100               | 165.3                                | *                     | *         | *                          | all metal consumed   |
| $P_{O_2}=10^{-11.2}$<br>$P_{S_2}=10^{-3.0}$<br>$P_{SO_2}=0.008$ | Fe-25Cr | 100               | -1.45                                | 13-16                 | —         | 0                          | thick Cr <sub>2</sub> O <sub>3</sub>   |
|   |         | 200               | -3.75                                | 14-18                 | —         | 10-15                      | Nodules at corner only,<br>sulfide pocketing   |
|   | Fe-20Cr | 100               | 1.11                                 | 6-7                   | —         | 0                          | thin Cr <sub>2</sub> O <sub>3</sub>  |
|   |         | 200               | 1.48                                 | 12-14                 | —         | 0                          | Cr <sub>2</sub> O <sub>3</sub>   |
|   | Fe-18Cr | 100               | 1.71                                 | 7-9                   | —         | 0                          | Cr <sub>2</sub> O <sub>3</sub>   |
|   |         | 200               | 387.9                                | *                     | *         | *                          | all metal consumed   |
| $P_{O_2}=10^{-12.0}$<br>$P_{S_2}=10^{-4.0}$<br>$P_{SO_2}=0.004$ | Fe-25Cr | 100               | -1.83                                | 6-9                   | —         | 0                          | Cr <sub>2</sub> O <sub>3</sub>   |
|   |         | 200               | -5.68                                | 18-21                 | —         | 0                          | Cr <sub>2</sub> O <sub>3</sub>   |
|   | Fe-20Cr | 100               | 0.94                                 | 4-5                   | 7-15      | 9-12                       | Cr <sub>2</sub> O <sub>3</sub> , Fe-oxide/Cr-rich oxide<br>internal Cr-rich sulfide, M <sub>2</sub> O <sub>3</sub> |
|   |         | 200               | 69.4                                 | 5                     | 1000      | 40-50                      | severe oxidation   |
|   | Fe-18Cr | 100               | 26.36                                | 3-4                   | 1000      | 25-35                      | severe oxidation   |
|   |         | 200               | 153.2                                | *                     | *         | *                          | all metal consumed   |

Table 18. The scale thickness and the penetration depth of Fe-Cr alloys, after 100 hours oxidation, in the sulfur-containing environment.

(a) *Fe-20Cr*

| environment<br>no.              | scale thickness, $\mu\text{m}$ |             | penetration depth, $\mu\text{m}$ |             |
|---------------------------------|--------------------------------|-------------|----------------------------------|-------------|
|                                 | coarse grain                   | small grain | coarse grain                     | small grain |
| 1. high $\text{P}_{\text{S}_2}$ | 5/25                           | 6-7/14-30   | 12-23                            | 20-25       |
| 2. low $\text{P}_{\text{S}_2}$  | 8-9                            | 6-7         | 0                                | 0           |
| 4. low $\text{P}_{\text{SO}_2}$ | 3-7                            | 4-5/7-15    | 0                                | 9-12        |

(b) *Fe-25Cr*

| environment<br>no               | scale thickness, $\mu\text{m}$ |             | penetration depth, $\mu\text{m}$ |             |
|---------------------------------|--------------------------------|-------------|----------------------------------|-------------|
|                                 | coarse grain                   | small grain | coarse grain                     | small grain |
| 1. high $\text{P}_{\text{S}_2}$ | 11-16/30-40                    | 10-12/30-40 | 15-40                            | 30-40       |
| 2. low $\text{P}_{\text{S}_2}$  | 9-10                           | 13-16       | 0                                | 0           |
| 4. low $\text{P}_{\text{SO}_2}$ | 5-9                            | 6-9         | 0                                | 0           |

Table 19. Experimental conditions; Oxidation of internal sulfides.

Corrosion type : presulfidation in the CO-CO<sub>2</sub>-SO<sub>2</sub>  
gas mixtures, and oxidation in air.

Alloys tested : Fe-30Cr, Fe-25Cr, Fe-20Cr

Mixed gas environments :

| temperature<br>K | gas mixture, vol. % |                 |                 |      | calc., atm                     |                                |
|------------------|---------------------|-----------------|-----------------|------|--------------------------------|--------------------------------|
|                  | CO                  | CO <sub>2</sub> | SO <sub>2</sub> | Ar   | log P <sub>O<sub>2</sub></sub> | log P <sub>S<sub>2</sub></sub> |
| 1223             | 0.5                 | 37.4            | 2.6             | 59.5 | -11.2                          | -4.0                           |

Summary of oxidation runs :

| run<br>no. | duration, hours |       |
|------------|-----------------|-------|
|            | presulfid.      | oxid. |
| 1          | 100             | 100   |
| 2          | 100             | 240   |
| 3          | 100             | 500   |

Table 20. Diffusion coefficients of sulfur in Fe-Cr alloys  
and interdiffusion coefficients of alloy.

(unit : cm<sup>2</sup>/sec)

(a) Diffusion coefficient of sulfur.

| Cr-content, wt.% | $D_s$                          | $D_s(T=1223 \text{ K})$ |
|------------------|--------------------------------|-------------------------|
| 18               | $0.166 \cdot \exp(-22,131/T)$  | $2.3 \times 10^{-9}$    |
| 26               | $0.0306 \cdot \exp(-20,568/T)$ | $1.5 \times 10^{-9}$    |
| 34               | $0.0618 \cdot \exp(-21,289/T)$ | $1.7 \times 10^{-9}$    |

(b) Interdiffusion coefficients of alloy.

| Cr-content, wt.% | $D_{\text{alloy}}(T=1273 \text{ K})$ |
|------------------|--------------------------------------|
| 18               | $1.1 \times 10^{-9}$                 |
| 27.4             | $4.1 \times 10^{-10}$                |
| 37.4             | $2.0 \times 10^{-10}$                |
| 59.9             | $2.9 \times 10^{-11}$                |

Table 21. The solubility of sulfur in various oxides.

| oxide                          | sulfur solubility wt. % | temperature °C | method of analysis          | reference |
|--------------------------------|-------------------------|----------------|-----------------------------|-----------|
| CaO                            | 0.011                   | 1650           |                             | 1         |
|                                | 0.036                   | 1650           |                             | 2         |
|                                | 0.8<br>0.003            | 1550<br>1500   | combustion &<br>gravimetric | 3<br>1    |
| CoO                            | 0.05                    | 1000           | combustion                  | 4         |
| Cr <sub>2</sub> O <sub>3</sub> | 9.0                     | 900            | electron probe              | 5         |
| Cu <sub>2</sub> O              | 0.1-0.8                 | 1000           | X-ray fluorescence          | 6         |
|                                | 0.02                    | 1000           | combustion                  | 7         |
| CuO                            | 0.1-0.5                 | 800            | X-ray fluorescence          | 6         |
| FeO                            | 0.014                   | 1250           | combustion                  | 8         |
|                                | 0.042                   | 1100           |                             | 9         |
|                                | 0.011                   | 1050           | combustion                  | 10        |
|                                | 0.03-0.4                | 800            | electron probe              | 11        |
| Fe <sub>3</sub> O <sub>4</sub> | 0.03                    | 500            | electron probe              | 11        |
| MnO                            | 0.66                    | 1232           |                             | 12        |
| NiO                            | 0.02-0.2                | 900-1000       | combustion                  | 4, 7      |
|                                | 5.0                     | 800            | electron probe              | 13        |
|                                | 2-3                     | 688            | electron probe              | 14        |
|                                | 0.09-0.12               | 600-700        | electron probe              | 5         |
| SrO                            | 0.04                    | 1650           |                             | 1         |
|                                | 0.016                   | 1500           |                             | 1         |

Table 21. (continued) References list;

1. G.J.W.Kor. and F.D.Richardson, *Trans. Inst. Min. Met.*, 79(1970)C148
2. R.A.Sharma and F. D.Richardson, *TAIME*, 233(1965)1586
3. G.R.St.Pierre and J.Chipman, *TAIME*,206(1956)1474
4. M.C.Pope and N.Birks, *Oxid. Metals*, 12(1978)191
5. M.G.Hocking and V.Vasantasree, *Corr.Sci.*, 16(1976)279
6. N.Birks and N.Tattam, *Corr.Sci.*, 10(1970)857
7. M.C.Pope, *Ph.D.Thesis, Sheffield Univ.*,1975
8. G.J.W.Kor. and E.T.Turkdogan, *Met.Trans.*, 2(1971)1571
9. T.Leonard and G.St.Pierre, See S.McCormick et al, *Met.Trans.*, 6B(1975)55
10. G.J.W.Kor., *Met. Trans.*, 3(1972)2343
11. T.Flatley and N.Birks, *J.I.S.I.*, 209(1971)523
12. H.C.Chao, Y.E.Smith and L.H.van Vlack, *TMS-AIME*, 227(1963)796
13. M.R.Wooton and N.Birks, *Corr.Sci.*, 12(1972)829
14. C.B.Alcock, M.G.Hocking and S.Zador, *Corr.Sci.*, 9(1969)111



**Figure captions**

- Figure 1. Mechanism of behavior.
- Figure 2. Fe-Cr phase diagram.
- Figure 3. Schematic diagram of experimental apparatus.
- Figure 4. Depiction of measurements to determine corrosion.
- Figure 5. The weight gain of Fe-20Cr and Fe-25Cr as a function of exposure time.
- Figure 6. Optical cross-section morphology of Fe-20Cr oxidized in the  $CaSO_4/CaO$  mixture in the low external  $P_{O_2}$  environment ( $P_{O_2}=10^{-11.2}$  atm) at 1223 K.
- (a) for 25 hours,
  - (b) for 50 hours,
  - (c) for 100 hours,
  - (d), (e), (f) for 200 hours.
- Figure 7. Scanning micrograph showing the cross-section morphology of Fe-20Cr oxidized for 150 hours in the  $CaSO_4/CaO$  mixture in the low external  $P_{O_2}$  environment ( $P_{O_2}=10^{-11.2}$  atm) at 1223 K.
- Figure 8. Scanning micrograph showing the cross-section morphology of Fe-20Cr oxidized in the  $CaSO_4/CaO$  mixture in the low external  $P_{O_2}$  environment ( $P_{O_2}=10^{-11.2}$  atm) for 200 hours at 1223 K.
- (a) S-line scan through the two-layer scale.
  - (b) S-map
- Figure 9. Scanning micrograph showing the cross-section morphology of Fe-20Cr oxidized in the  $CaSO_4/CaO$  mixture in the low external  $P_{O_2}$  environment ( $P_{O_2}=10^{-11.2}$  atm) for 200 hours at 1223 K. Fe-, Cr-, Ca- and S- line scan through the scale.

Figure 10. The  $\text{CaO-Cr}_2\text{O}_3$  system.

Figure 11. A schematic of the corrosion induced in Fe-Cr alloys in the presence of  $\text{CaSO}_4$  and a low oxygen partial pressure atmosphere.

Figure 12. Schematic thermodynamic phase stability diagram for Cr-O-S system. Region 1 represent the condition studied by investigators interested in gasification processes; Region 2 represent the condition studied by investigators interested in conventional combustion; Region 3 represents the condition relevant to in-bed corrosion in fluidized bed combustion.

Figure 13. Schematic diagram of the experimental apparatus for the mixed gas environments.

Figure 14. Thermodynamic phase stability diagram for Cr-O-S system and Fe-O-S system, showing the oxygen and sulfur activities of the atmospheres used in the present study.

(a) 1223 K

(b) 1123 K

Figure 15. The weight gain of Fe-15Cr, Fe-20Cr and Fe-25Cr as a function of exposure time, in the low  $P_{S_2}$  atmosphere ( $P_{S_2}=10^{-5}$ ,  $P_{O_2}=10^{-11.2}$  atm), environment number 2, at 1223 K.

Figure 16. The weight gain of Fe-20Cr as a function of exposure time, in the two different  $P_{S_2}$  atmosphere at the same  $P_{O_2}$  atmosphere at 1223 K.

Figure 17 The variation of the thickness of the typical scale of Fe-20Cr and Fe-25Cr as a function of exposure time, in the four different environments at 1223 K.

(a) Fe-20Cr

(b) Fe-25Cr.

Figure 18. The maximum penetration depth of the Fe-Cr alloys as a function of exposure time, in two atmospheres with the same  $P_{O_2}$  but different  $P_{S_2}$ .

(a) Fe-20Cr

(b) Fe-25Cr.

Figure 19. Optical micrographs showing the cross-section morphology of Fe-15Cr oxidized for 25 hours in the two different  $P_{S_2}$  atmospheres at the same  $P_{O_2}$  ( $P_{O_2}=10^{-11.2}$  atm) at 1223 K.

(a) at  $P_{S_2}=10^{-4}$  atm

(b) at  $P_{S_2}=10^{-5}$  atm.

Figure 20. The breakaway process of an Fe-20Cr alloy in the high  $P_{S_2}$  atmosphere at 1223 K.

Figure 21. SEM topography and optical cross-section morphology of the scale produced on Fe-20Cr oxidized for 50 hours in the high  $P_{S_2}$  atmosphere at 1223 K.

Figure 22. Scanning electron micrograph exhibiting the cross-section morphology of an Fe-20Cr alloy oxidized for 100 hours in the high  $P_{S_2}$  atmosphere at 1223 K.

Figure 23. SEM micrograph of the scale-alloy interface, revealed by deep etching technique, of Fe-20Cr oxidized for 100 hours in the two different  $P_{S_2}$  atmospheres at the same  $P_{O_2}$  ( $P_{O_2}=10^{-11.2}$  atm) at 1223 K.

(a) at  $P_{S_2}=10^{-4}$  atm

(b) at  $P_{S_2}=10^{-5}$  atm

Figure 24. SEM topography of the descaled substrate of an Fe-20Cr alloy oxidized for 200 hours in the very low  $P_{S_2}$  atmosphere ( $P_{O_2}=10^{-11.2}$ ,  $P_{S_2}=10^{-6}$  atm) at 1223 K.

Figure 25. Scanning micrograph showing the cross-section morphology of Fe-25Cr oxidized for 25 hours in the high  $P_{S_2}$  atmosphere ( $P_{S_2}=10^{-4}$  atm) at 1223 K.

Figure 26. The cross-section morphology of Fe-25Cr oxidized for 50 hours in the high  $P_{S_2}$  atmosphere at 1223 K.

(a) Optical micrograph

(b) SEM micrograph with X-ray elemental mapping

Figure 27. The cross-section morphology, etched by Villela's reagent, of Fe-25Cr oxidized for 100 hours in the high  $P_{S_2}$  atmosphere at 1223 K.

(a) Optical micrograph

(b) SEM micrograph with X-ray elemental mapping

Figure 28. Underview of the scale produced on Fe-25Cr oxidized for 100 hours in the very low  $P_{S_2}$  atmosphere ( $P_{S_2}=10^{-6}$  atm) at 1223 K. Small amounts of sulfur were detected locally on the inner surface of the Cr-oxide scale.

Figure 29. SEM fractography of the scale formed on Fe-25Cr oxidized at 1223 K,

(a) for 200 hours in the low  $P_{SO_2}$  atmosphere ( $P_{O_2}=10^{-12.0}$ ,  $P_{S_2}=10^{-4}$ ,  $P_{SO_2}=0.004$  atm)

(b) for 150 hours in the high  $P_{S_2}$  atmosphere ( $P_{O_2}=10^{-11.2}$ ,  $P_{S_2}=10^{-4}$ ,  $P_{SO_2}=0.026$  atm)

(c) for 150 hours in the high  $P_{S_2}$  atmosphere, X-ray elemental mapping (S, Cr, Fe).

- Figure 30. Optical micrograph of the cross-section of an Fe-30Cr alloy oxidized for 50 hours in the high  $P_{S_2}$  atmosphere at 1223 K.
- Figure 31. SEM topography of the outer surfaces of the scales produced on Fe-20Cr and Fe-25Cr oxidized for 100 hours, respectively, in the three different  $P_{S_2}$  atmospheres ( $P_{S_2}=10^{-4}$ ,  $10^{-5}$ ,  $10^{-6}$  atm) at the same  $P_{O_2}$  ( $P_{O_2}=10^{-11.2}$  atm) at 1223 K.
- Figure 32. The functional relationship between the scale thickness and the (Fe/Cr) ratio at the external surface of scale. Fe-20Cr and Fe-25Cr were oxidized for varying times in the two different  $P_{S_2}$  atmospheres at the same  $P_{O_2}$  at 1223 K.
- Figure 33. Spalling tendency of the scales on Fe-20Cr and Fe-25Cr formed in the three different  $P_{S_2}$  atmospheres ( $P_{S_2}=10^{-4}$ ,  $10^{-5}$ ,  $10^{-6}$  atm) at the same  $P_{O_2}$  ( $P_{O_2}=10^{-11.2}$ ) at 1223 K.
- Figure 34. SEM fractography of the scale formed on Fe-25Cr oxidized for 200 hours in the low  $P_{SO_2}$  atmosphere ( $P_{SO_2}=0.004$ ,  $P_{O_2}=10^{-12}$ ,  $P_{S_2}=10^{-4}$  atm) at 1223 K.
- Figure 35. Topography of the scale produced on Fe-25Cr oxidized for 50 hours in the high  $P_{S_2}$  atmosphere ( $P_{O_2}=10^{-11.2}$ ,  $P_{S_2}=10^{-4}$  atm) at 1223 K. CrS agglomerates were detected locally on the surface of the descaled alloy substrate.
- Figure 36. Schematic representation of the development of the corrosion.
- (i) Precipitation of Cr-rich sulfides
  - (ii) Coarsening of the sulfides and development of a two-layer scale.
  - (iii) Intrusion of Cr-rich oxide into the metal as a result of the oxidation

of the Cr-rich sulfides and the development of a mixed Fe-Cr oxide layer beneath the outer Fe-oxide layer.

(iv) Thickening and sideways growth of the two-layer scale nodules.

Figure 37. A schematic of the "critical microstructure".

Figure 38. SEM micrograph showing the cross-section morphology of an Fe-18Cr alloy preoxidized for 50 hours in air and then oxidized for 100 hours in the high  $P_{S_2}$  atmosphere at 1223 K.

Figure 39. Comparison of the spalling tendency of the scale formed on the Fe-20Cr alloy.

(a) 100 hours preoxidation in air and 100 hours oxidation in the high  $P_{S_2}$  atmosphere.

(b) 100 hours oxidation in the high  $P_{S_2}$  atmosphere.

Figure 40. SEM fractography of the scale and metal for an Fe-25Cr alloy preoxidized for 100 hours in air and then oxidized for 500 hours in the high  $P_{S_2}$  atmosphere at 1223 K.

Figure 41. Change of lattice constant of  $\alpha$ - $Cr_2O_3$  (hexagonal crystal structure) scale in terms of Cr-content in Fe-Cr alloy.

Figure 42. The variation of half-width and lattice constant as a function of scattering angle at the three different voltages. Fe-20Cr alloy preoxidized for 100 hours in air and then oxidized for 100 hours in the high  $P_{S_2}$  atmosphere at 1223 K.

(a) Half-widths,  $\delta(2\theta)$ , of the (110), (116), (300), (220) peaks for  $\alpha$ - $Cr_2O_3$ .

(b) Lattice constants.

Figure 43. The cross-section morphology of the small grained Fe-20Cr alloy oxidized for 200 hours in the low  $P_{SO_2}$  atmosphere ( $P_{SO_2}=0.004$ ,  $P_{O_2}=10^{-12}$ ,  $P_{S_2}=10^{-4}$  atm) at 1223 K.

(a) Optical micrograph

(b) SEM micrograph

Figure 44. The cross-section morphology of the coarse grained Fe-20Cr alloy oxidized for 200 hours in the low  $P_{SO_2}$  atmosphere ( $P_{SO_2}=0.004$ ,  $P_{O_2}=10^{-12}$ ,  $P_{S_2}=10^{-4}$  atm) at 1223 K.

(a) Optical micrograph

(b) SEM micrograph

Figure 45. Cross-section morphology of the coarse grained Fe-25Cr alloy oxidized for 100 hours in the high  $P_{S_2}$  atmosphere at 1223 K.

(a) SEM micrograph. point #1-3: CrS, point #4:  $Cr_2O_3$ , point #5: Cr(S,O).

(b) Auger spectrum corresponding to #1-5.

Figure 46. SEM micrograph showing the cross-section morphology of the coarse grained Fe-20Cr alloy presulfidized for 100 hours in the high  $P_{S_2}$  atmosphere and then oxidized in air for 500 hours at 1223 K.

Figure 47. Cross-section morphology of the coarse grained Fe-25Cr alloy presulfidized for 100 hours in the high  $P_{S_2}$  atmosphere and then oxidized in air for 500 hours at 1223 K.

(a) Optical micrograph. point #1-4: CrS, point #5:  $Cr_2O_3$ , point #0: Cr(O,S).

(b) Auger spectrum corresponding to #0-5,

(c) Elemental mapping (S, O, Cr, Fe, C).

Figure 48. Optical micrograph showing the cross-section morphology of coarse grained Fe-25Cr alloy presulfidized for 100 hours in the high  $P_{S_2}$  atmosphere and then oxidized in air at 1223 K.

Figure 49. Schematic representation of development of "critical microstructure".

Figure 50. Thermodynamic phase stability diagram for Ca-O-S system at 1123 K and at 1223 K.

Figure 51. The maximum penetration depth of Fe-Cr alloys as a function of Cr-content at 1223 K.

Figure 52. The possible reaction paths for formation and distribution of sulfides in the scale and alloy.

Figure 53. Schematic diagram of the possible transport paths of sulfur in the scale and alloy.

Figure 54. The diffusion coefficients of chromium, oxygen and sulfur in  $Cr_2O_3$ .

Figure 55. The chromium concentration gradient and the size of internal sulfides as a function of distance from the scale-alloy interface.

Figure 56. Mechanism of the formation of porous  $Cr_2O_3$  and inward movement of liberated sulfur.

Figure 57. Schematic of major compositional and microstructural changes occurring during breakaway process.

(a) Mechanical breakdown in oxidizing atmosphere.

(b) Chemical breakdown in sulfur-containing atmosphere.

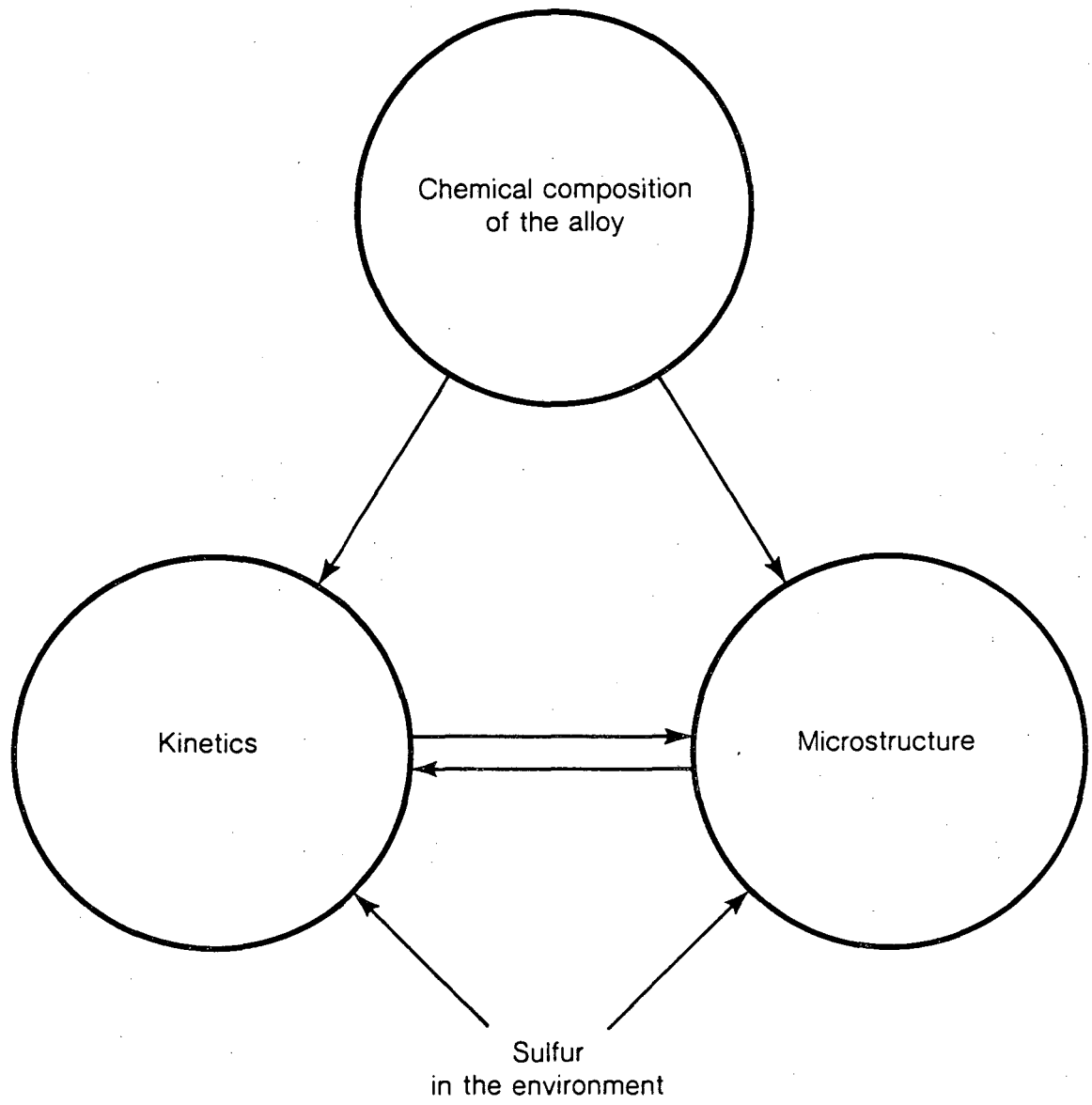
Figure 58. Schematic description of breakaway process occurring during formation



of the "critical microstructure".

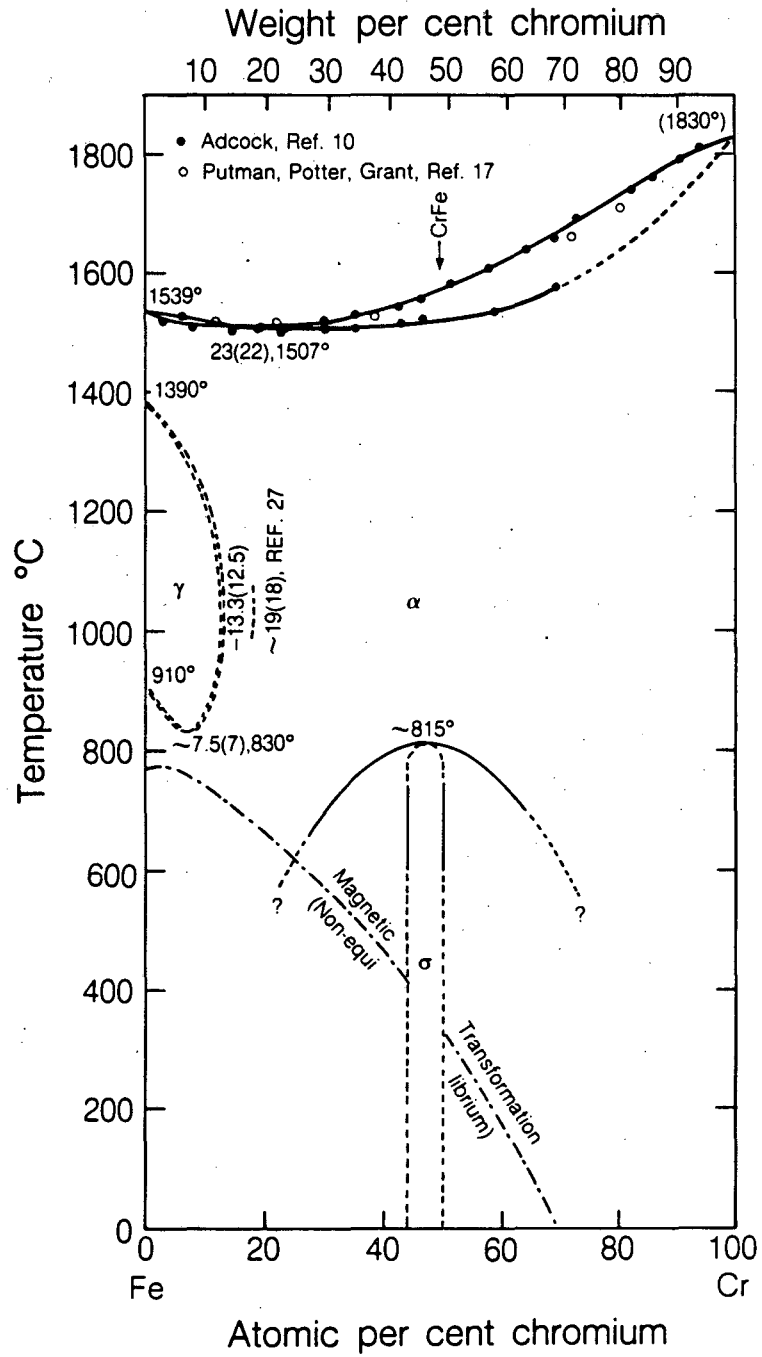
- (a) Breakaway kinetics for sulfidation/oxidation corrosion.
- (b) The general form of the rate-curve for a breakaway process.

Figure 59. Scale failure modes as a function of thickness and impressed strain.



XBL 856-10024

Figure 1.



XBL 856-10022

Figure 2.

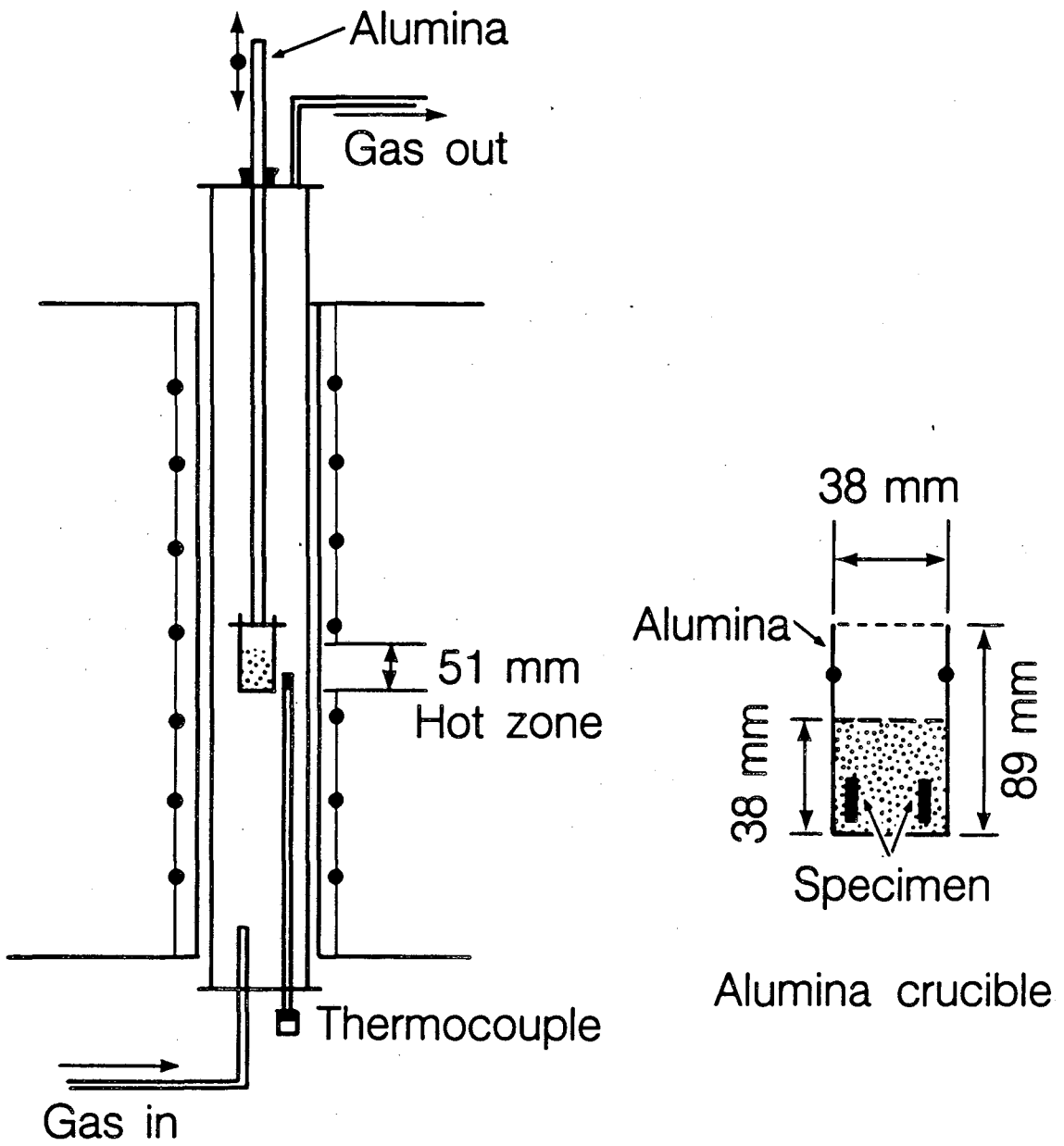
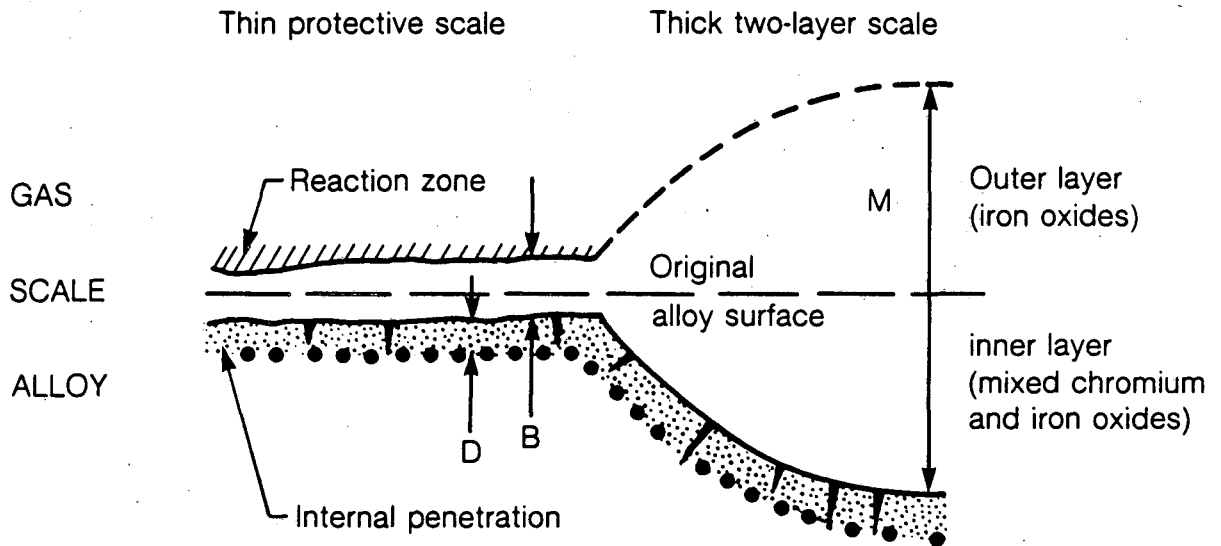


Figure 3.

XBL 856-10023



B : typical scale thickness of the thin protective scale

D : penetration depth into the metal

M : thickness of thick two-layer scale

XBL 856-10038

Figure 4.

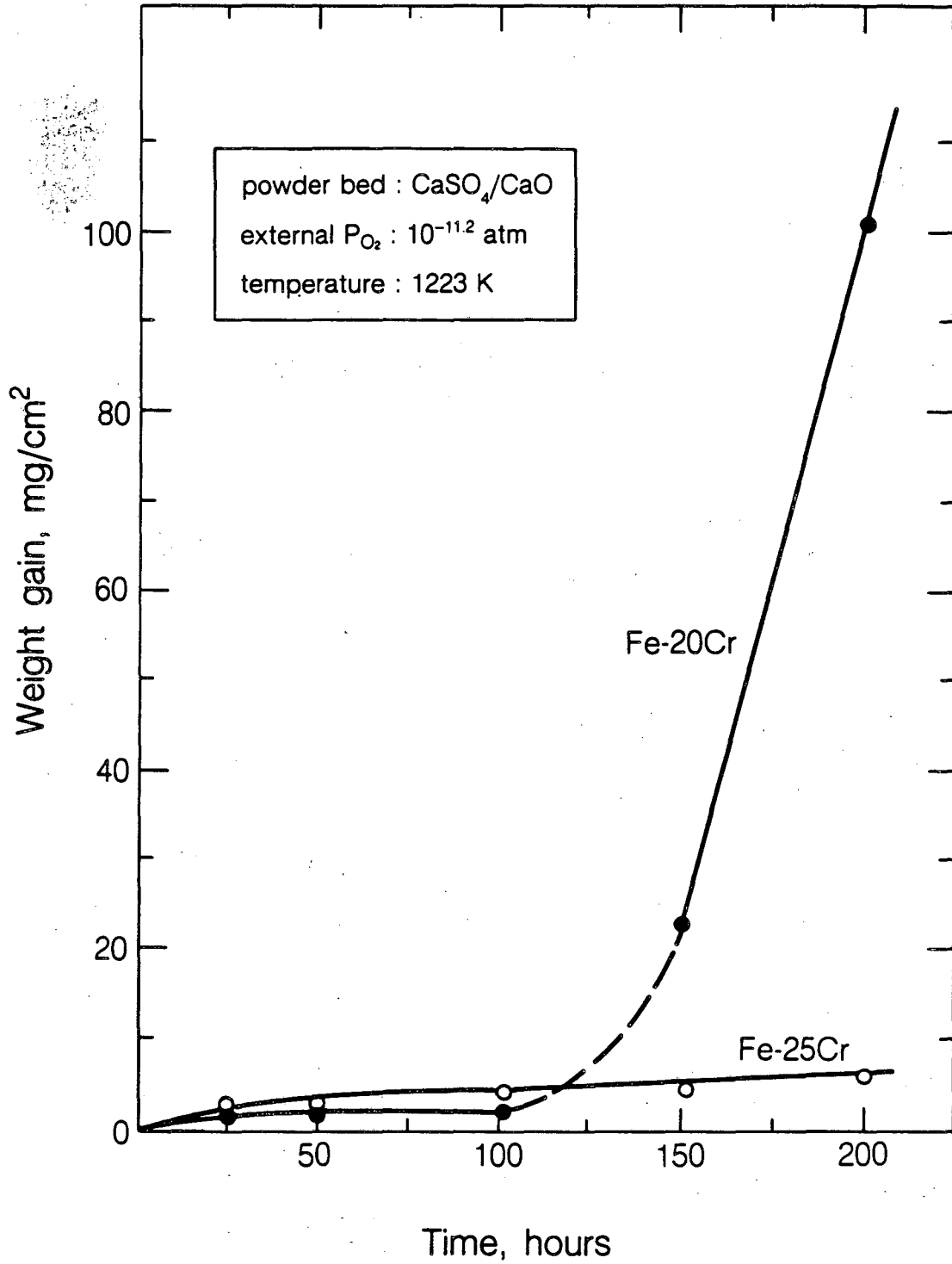
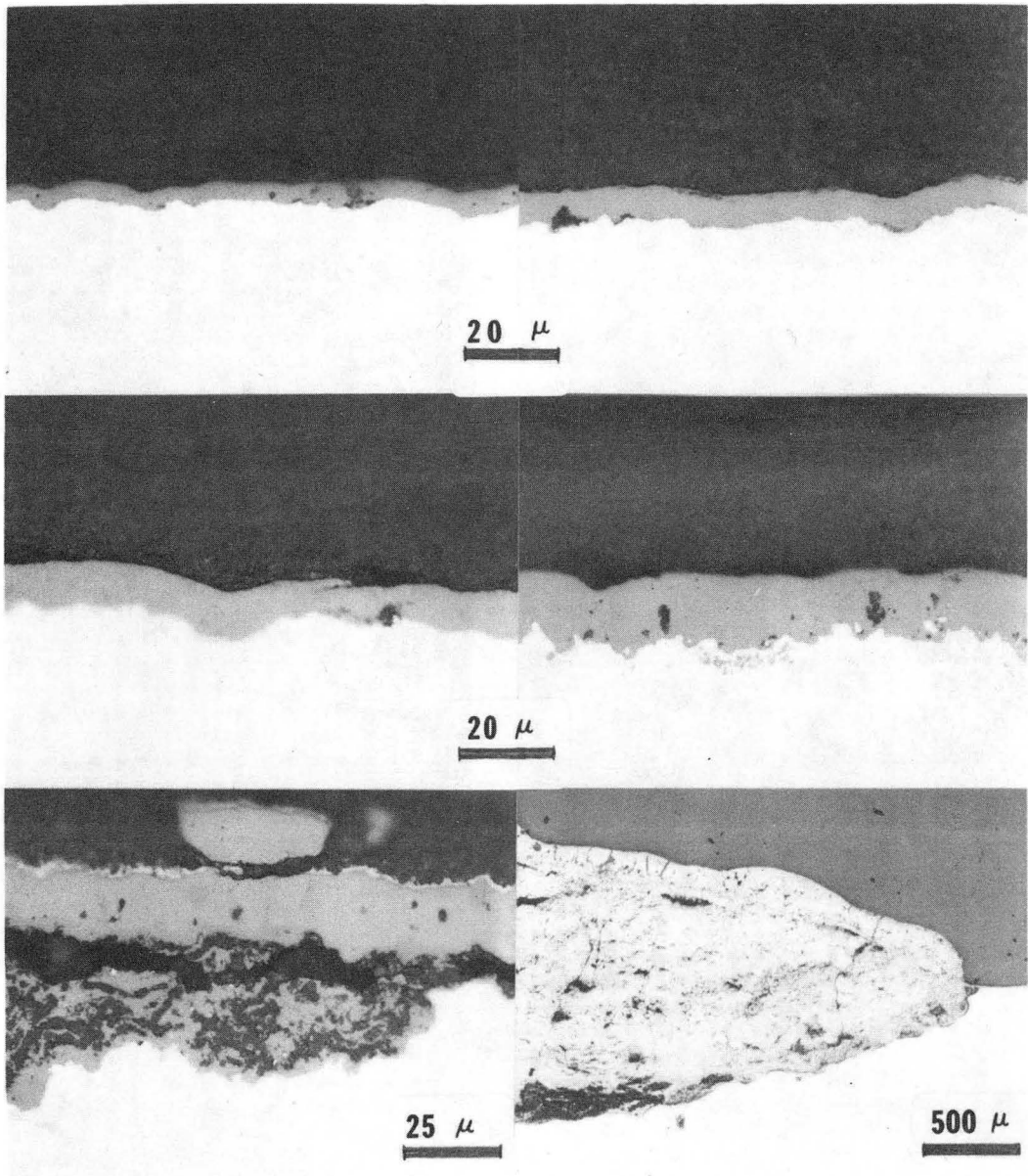


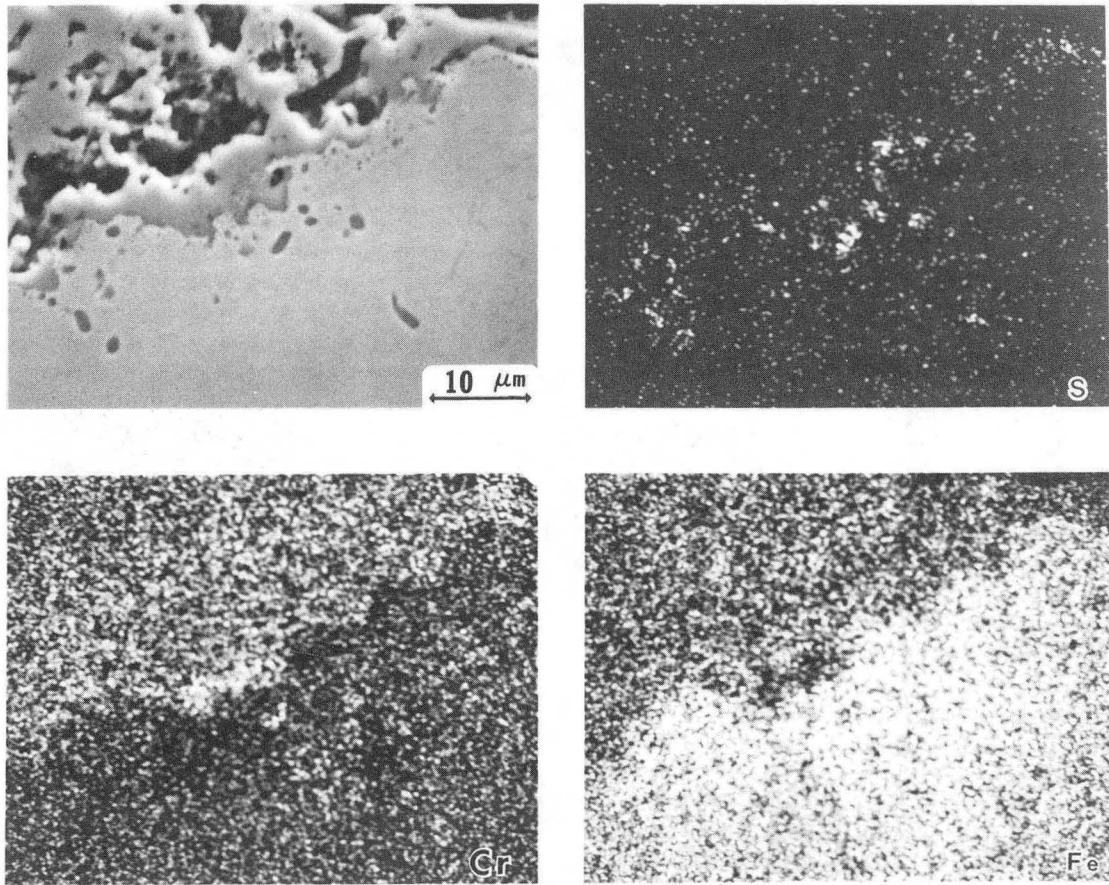
Figure 5.

XBL 856-10021



XBB 838-7057

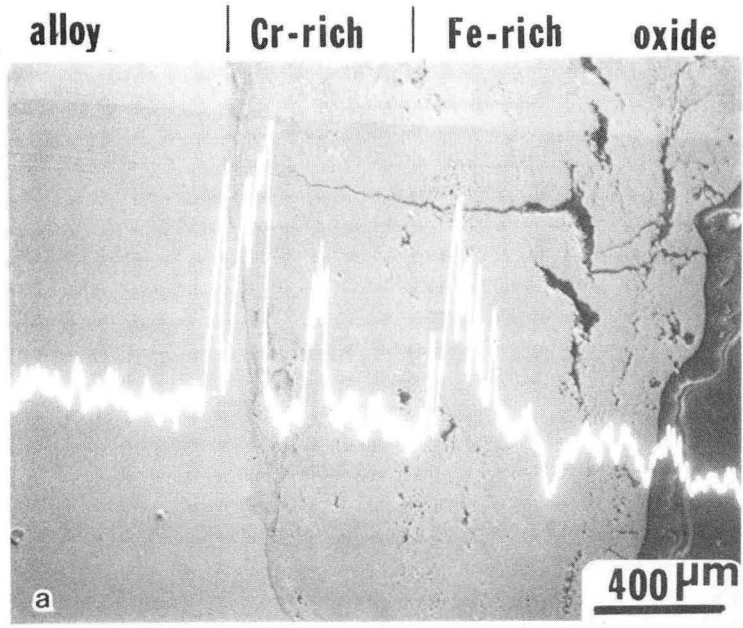
Figure 6.



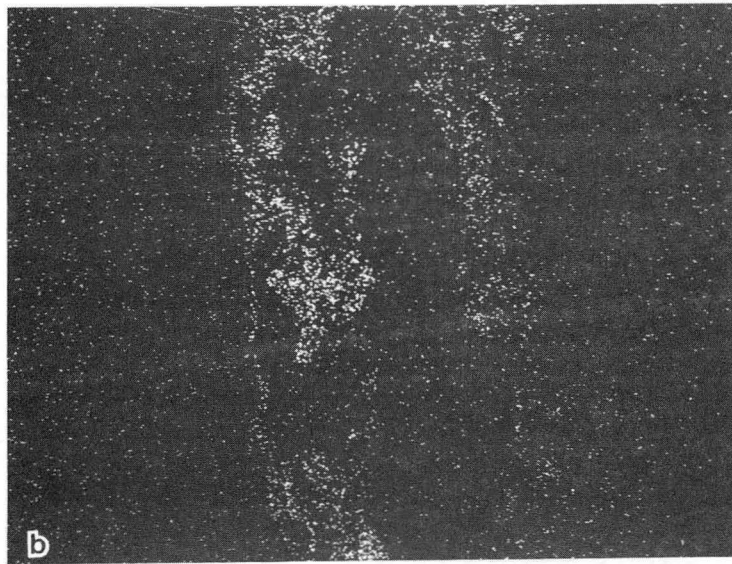
XBB 856-4556

Figure 7.





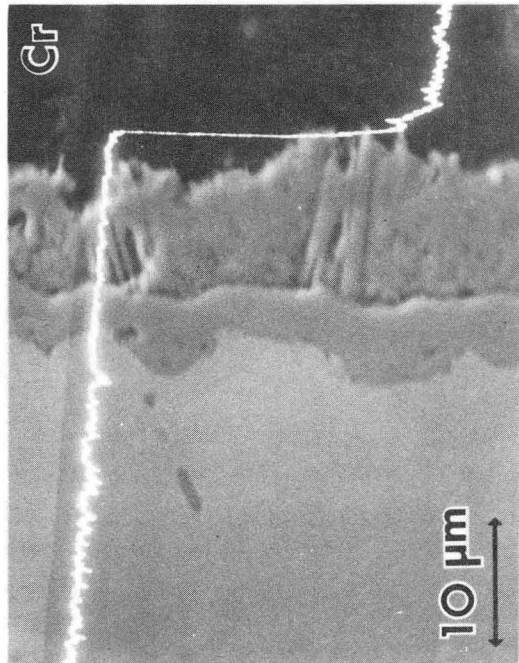
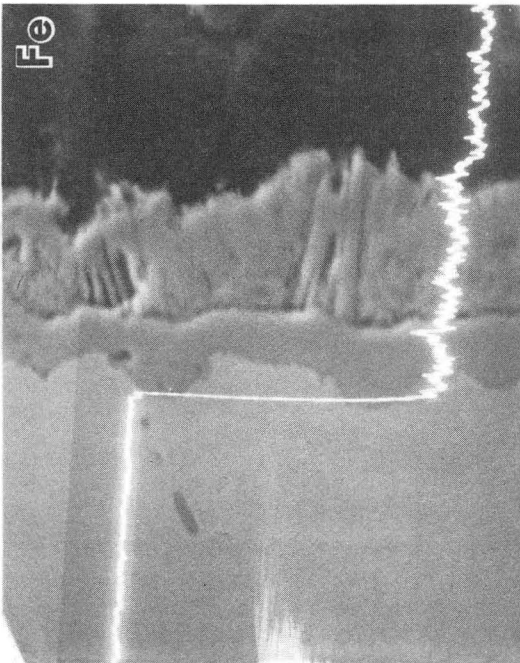
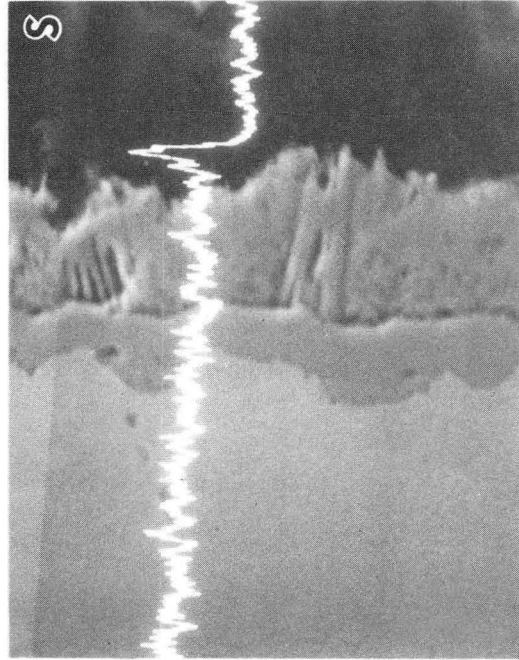
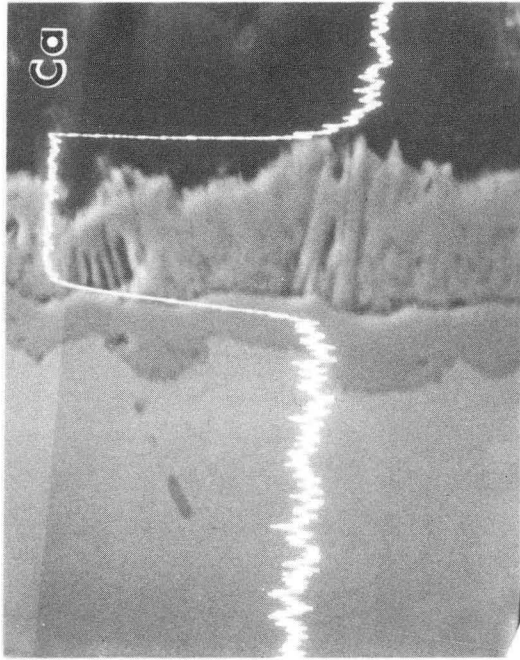
**S-line**



**S-map**

XBB 856-4577

Figure 8.



10  $\mu\text{m}$

XBB 856-4583

Figure 9.

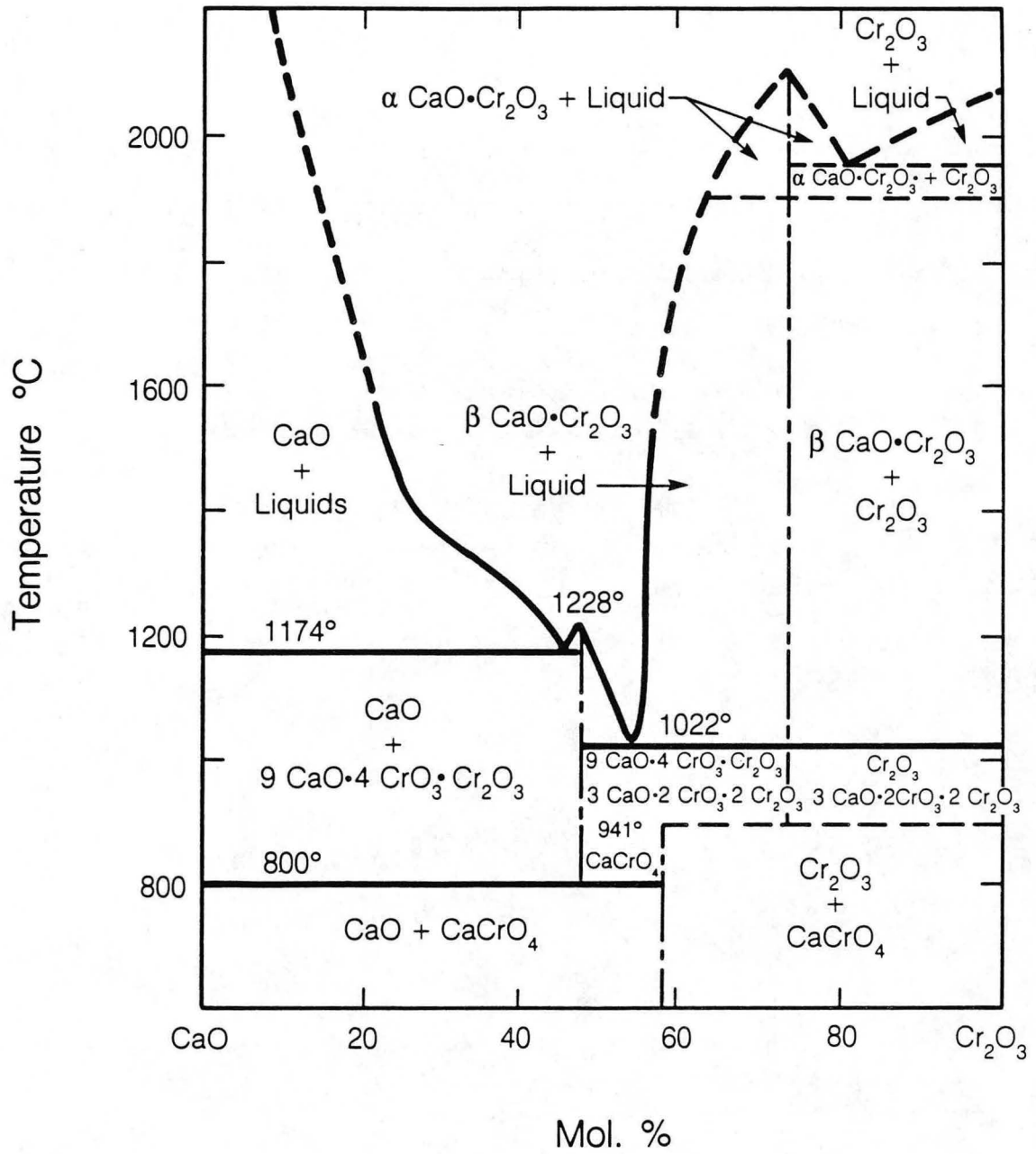
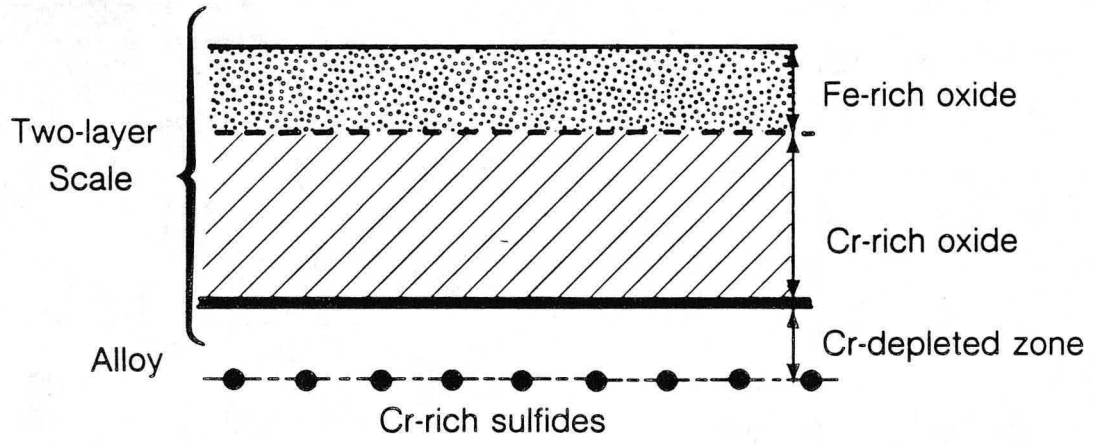


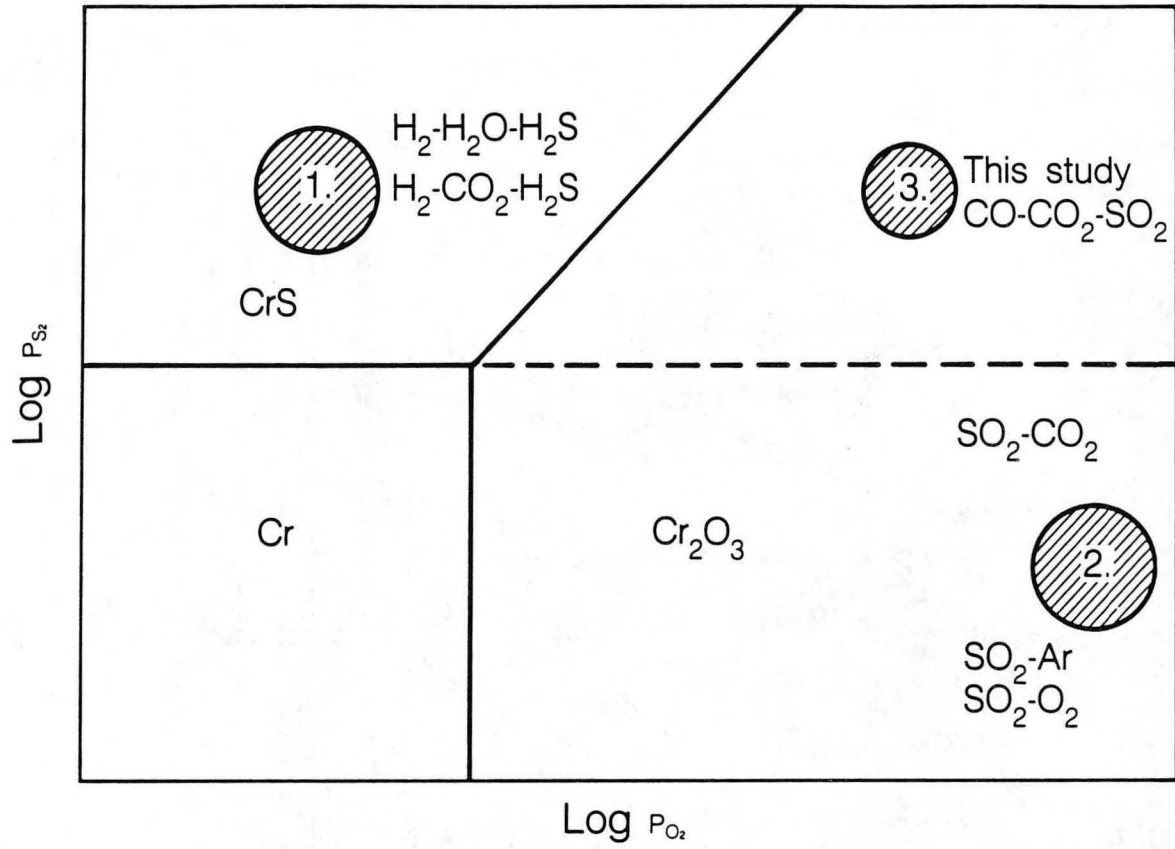
Figure 10.

XBL 856-10003



XBL 856-10018

Figure 11.



XBL 856-10019

Figure 12.

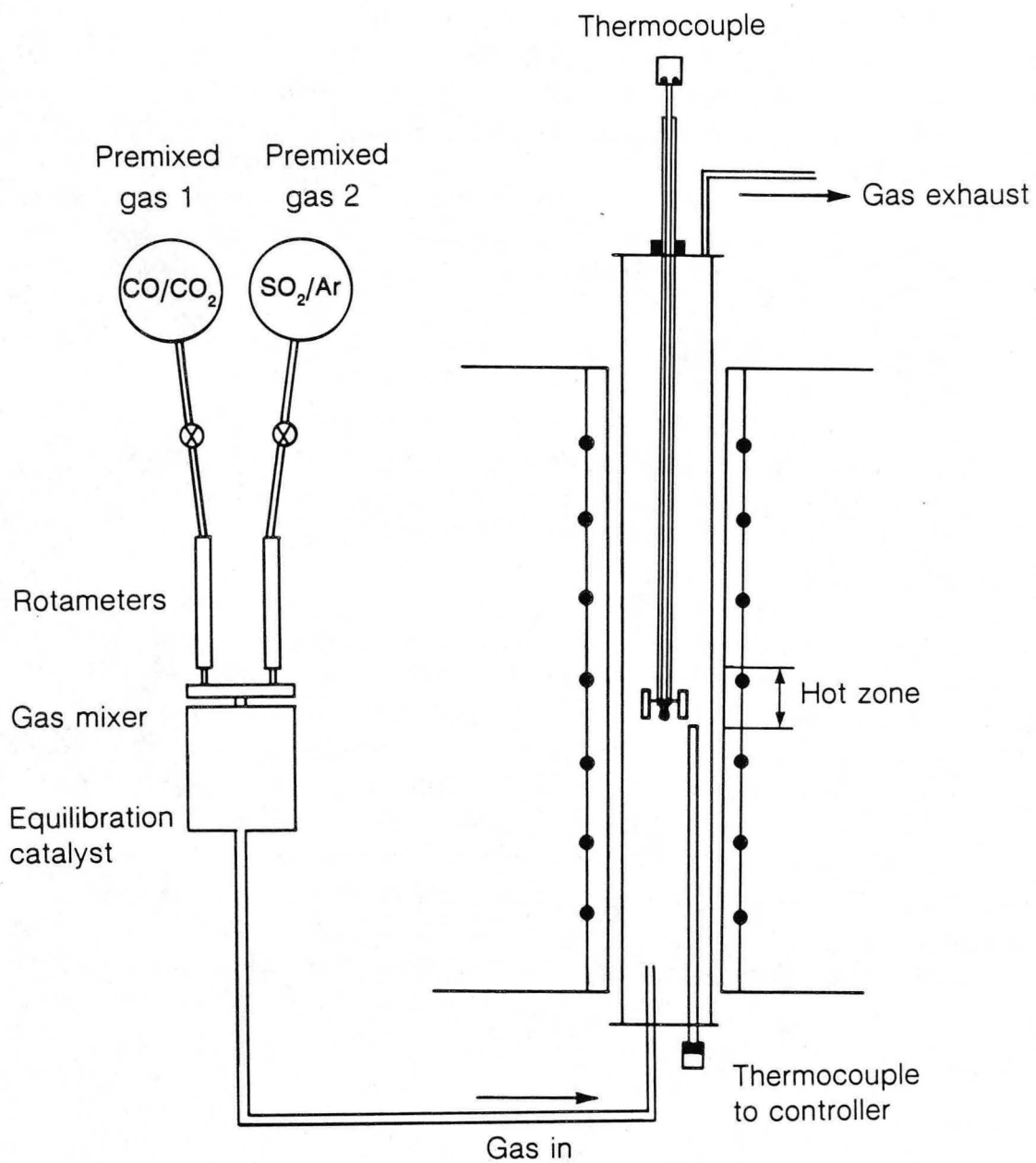


Figure 13.

XBL 856-10020

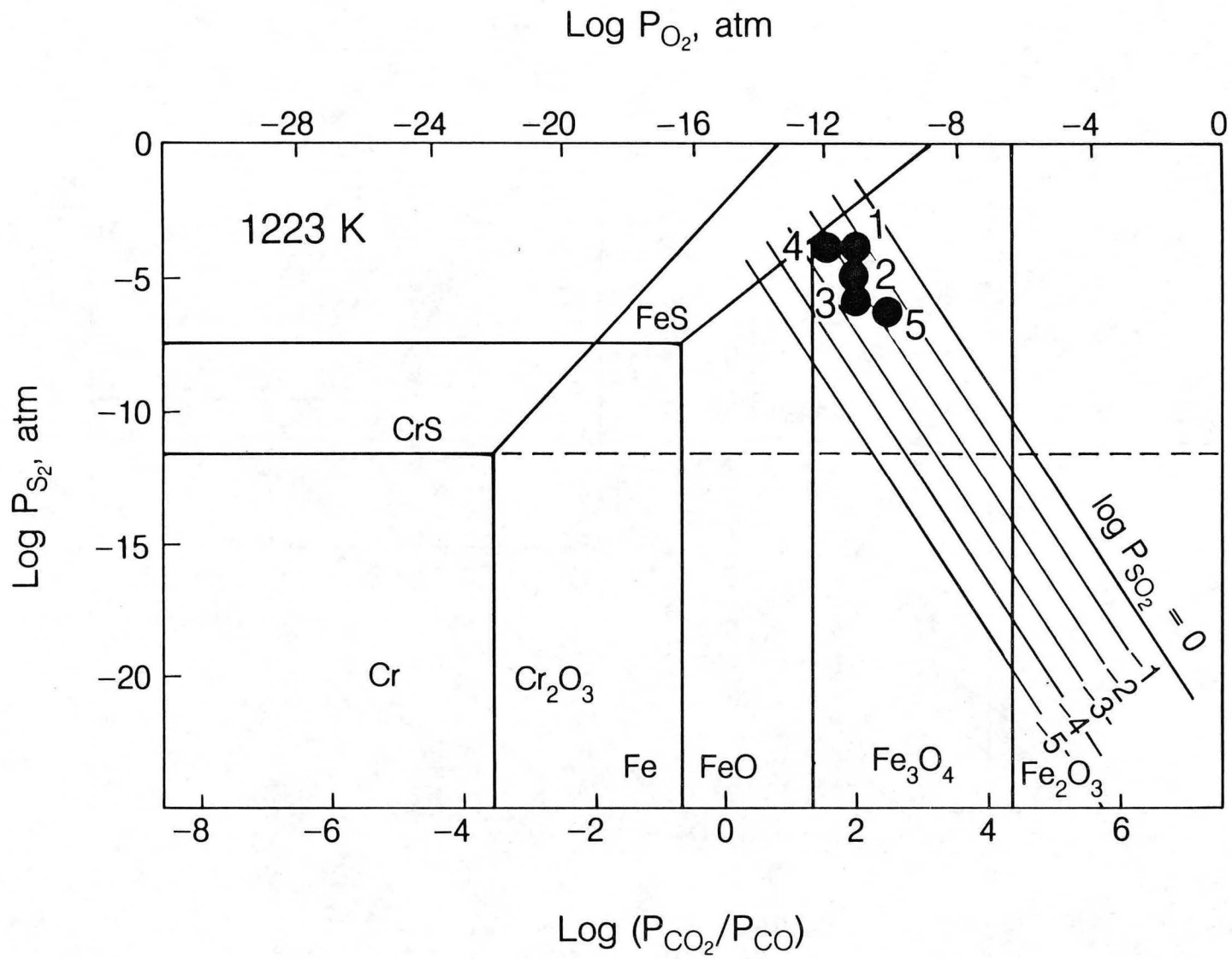


Figure 14a.

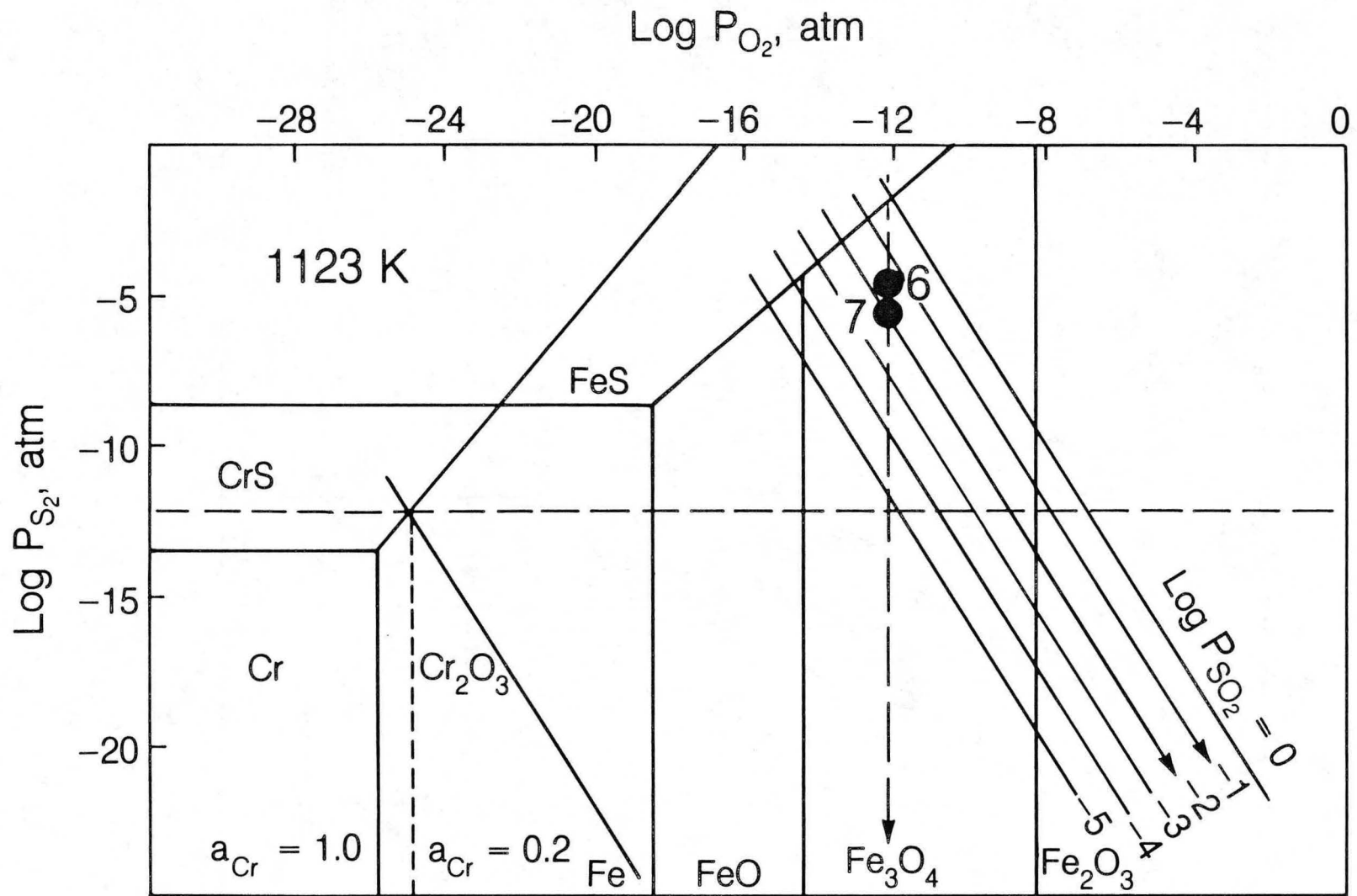


Figure 14b.

XBL 856-10016



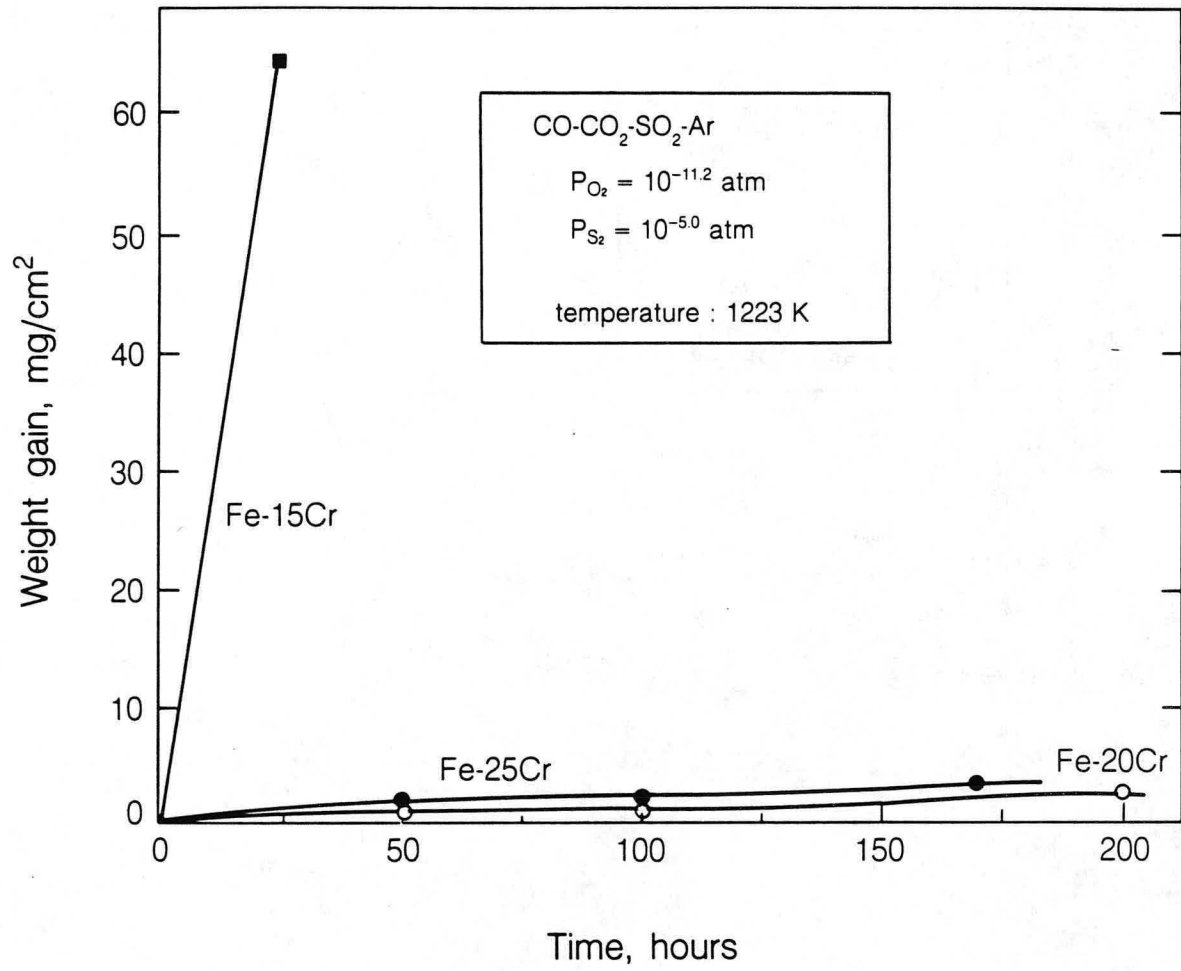


Figure 15.

XBL 856-10015

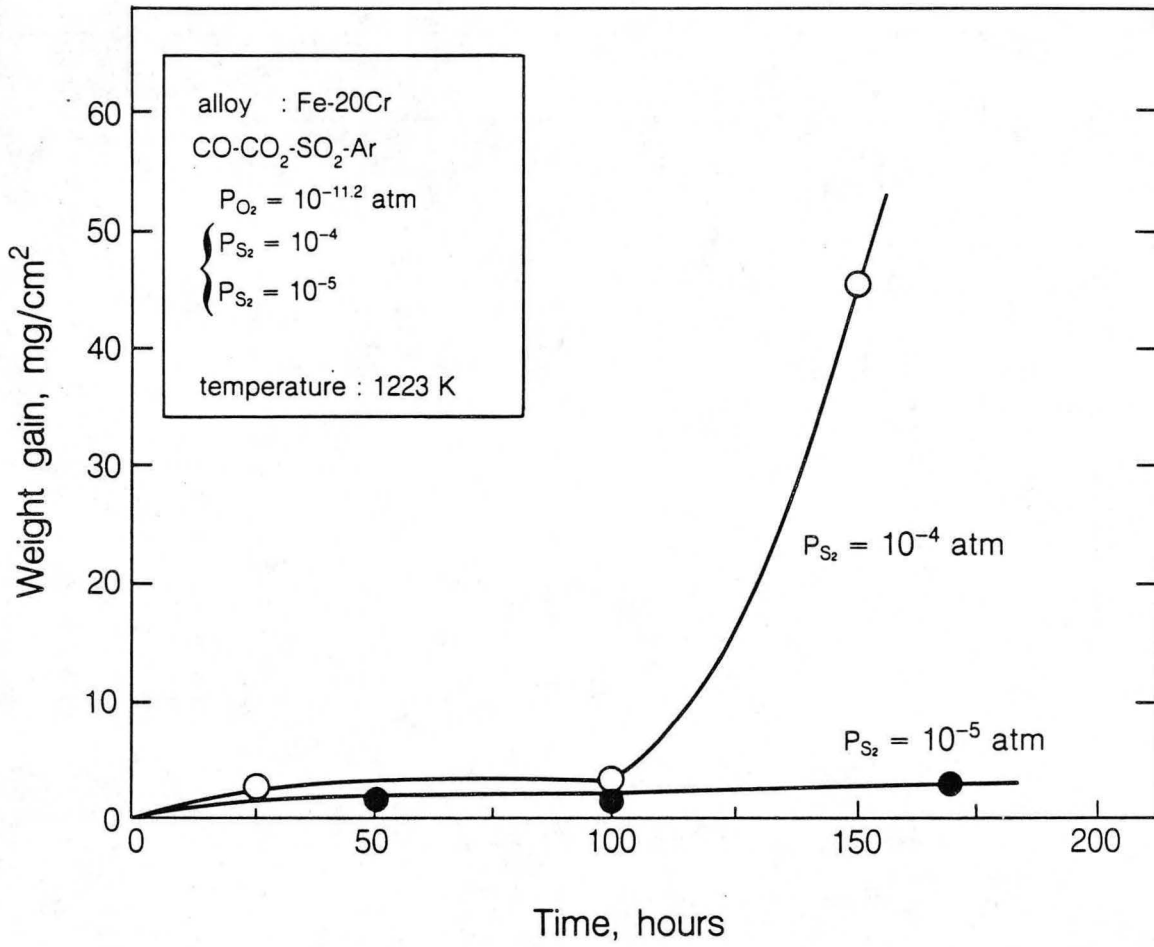
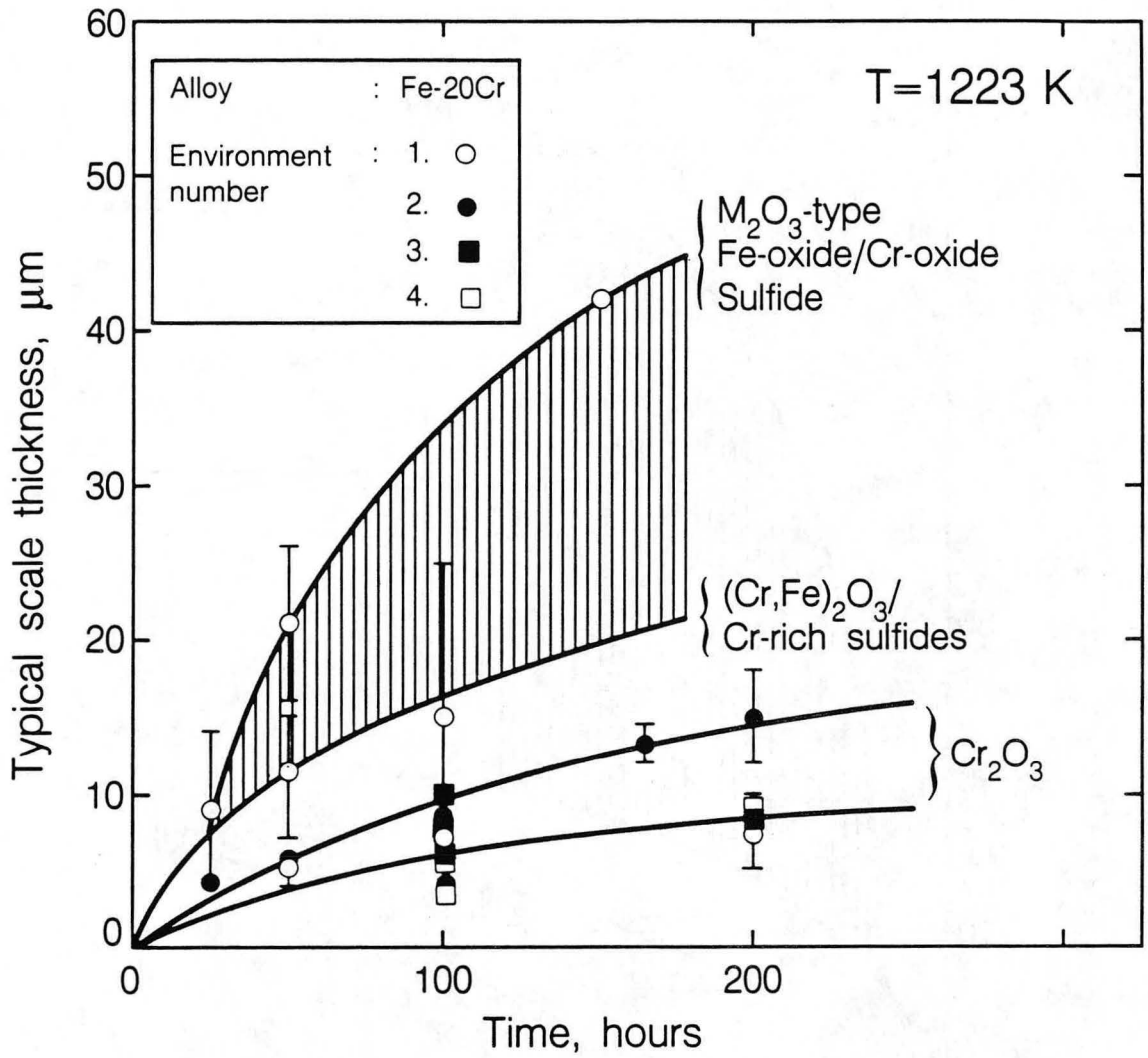


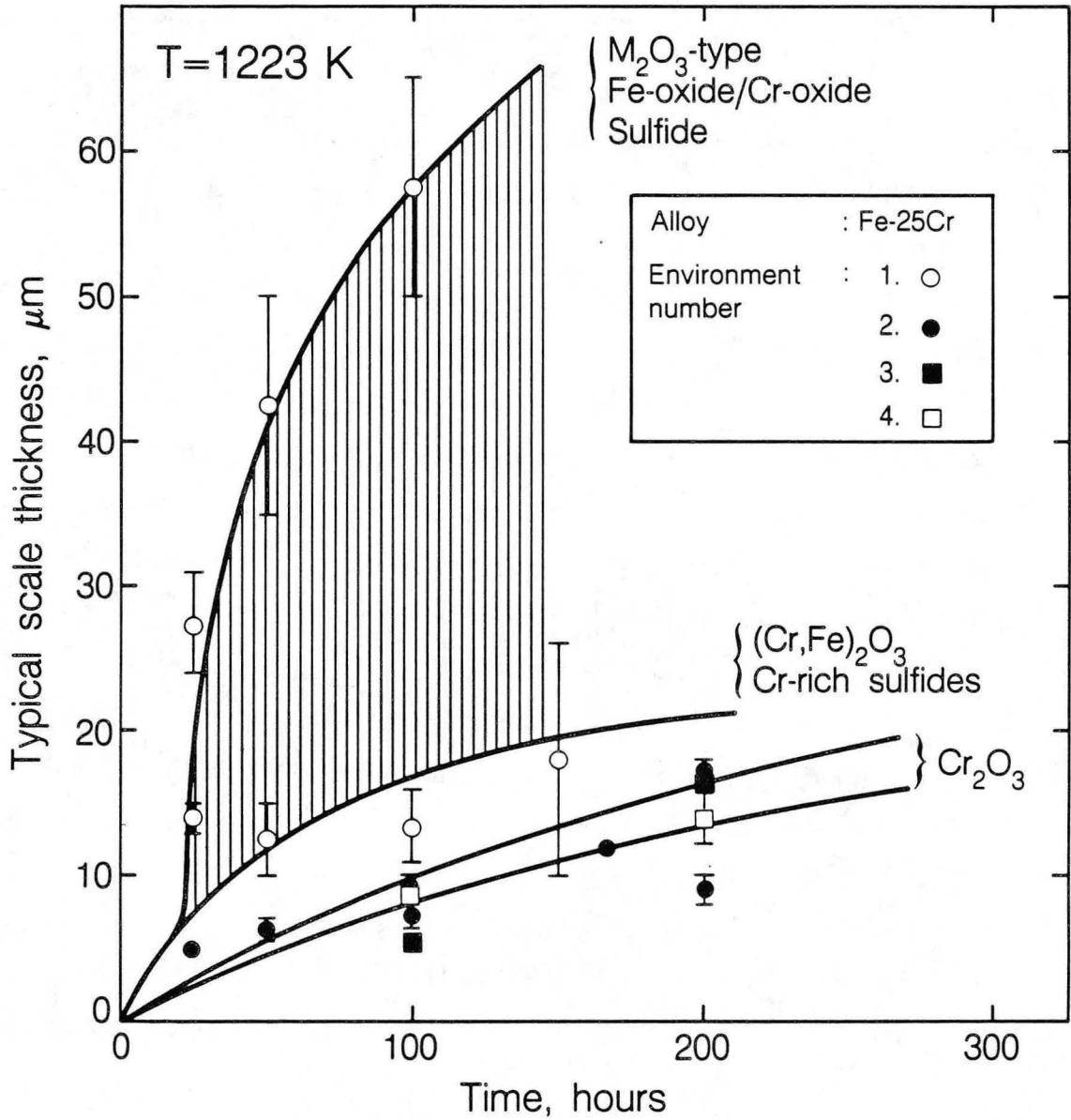
Figure 16.

XBL 856-10014



XBL 856-10034

Figure 17a.



XBL 856-10035

Figure 17b.

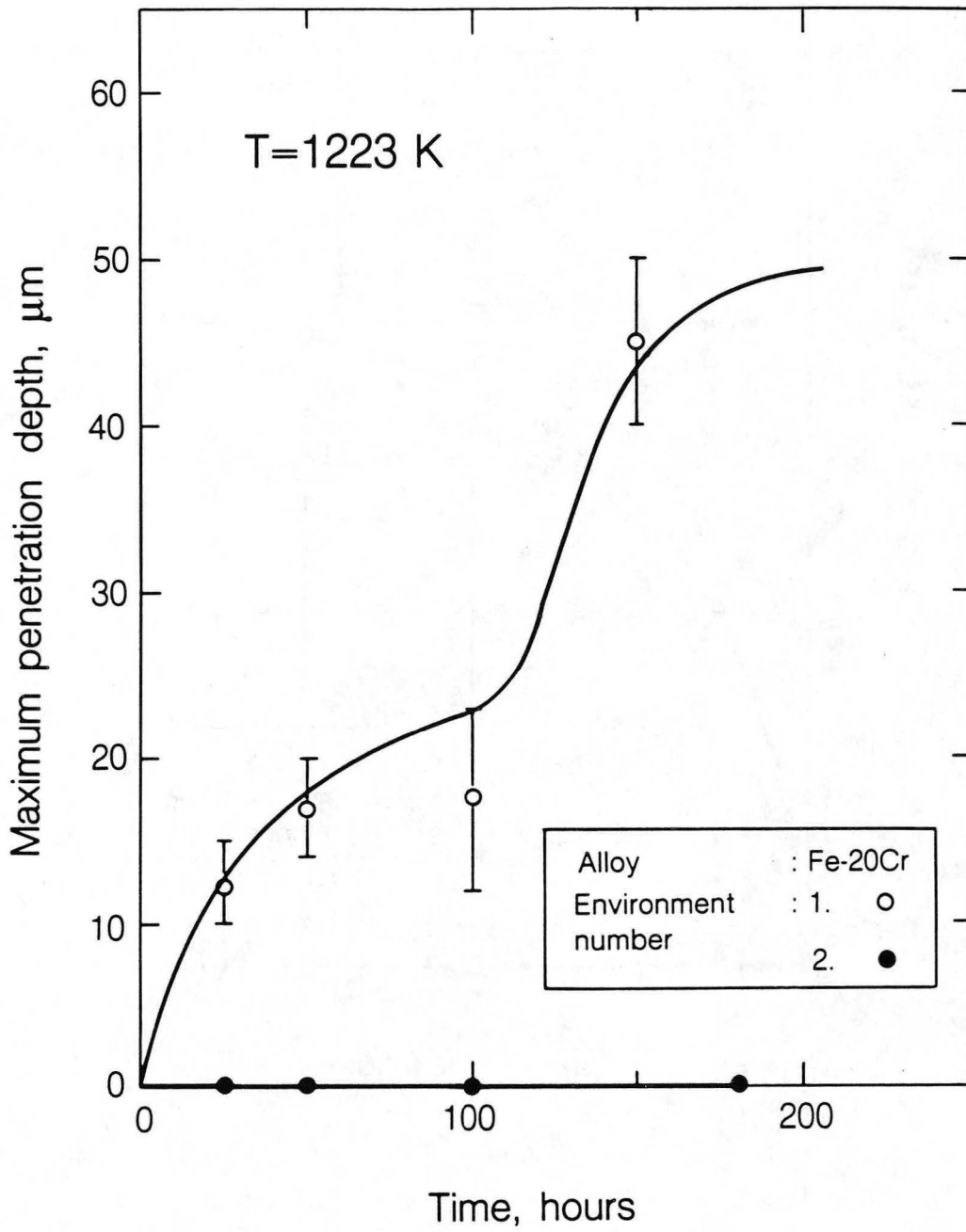


Figure 18a.

XBL 856-10036

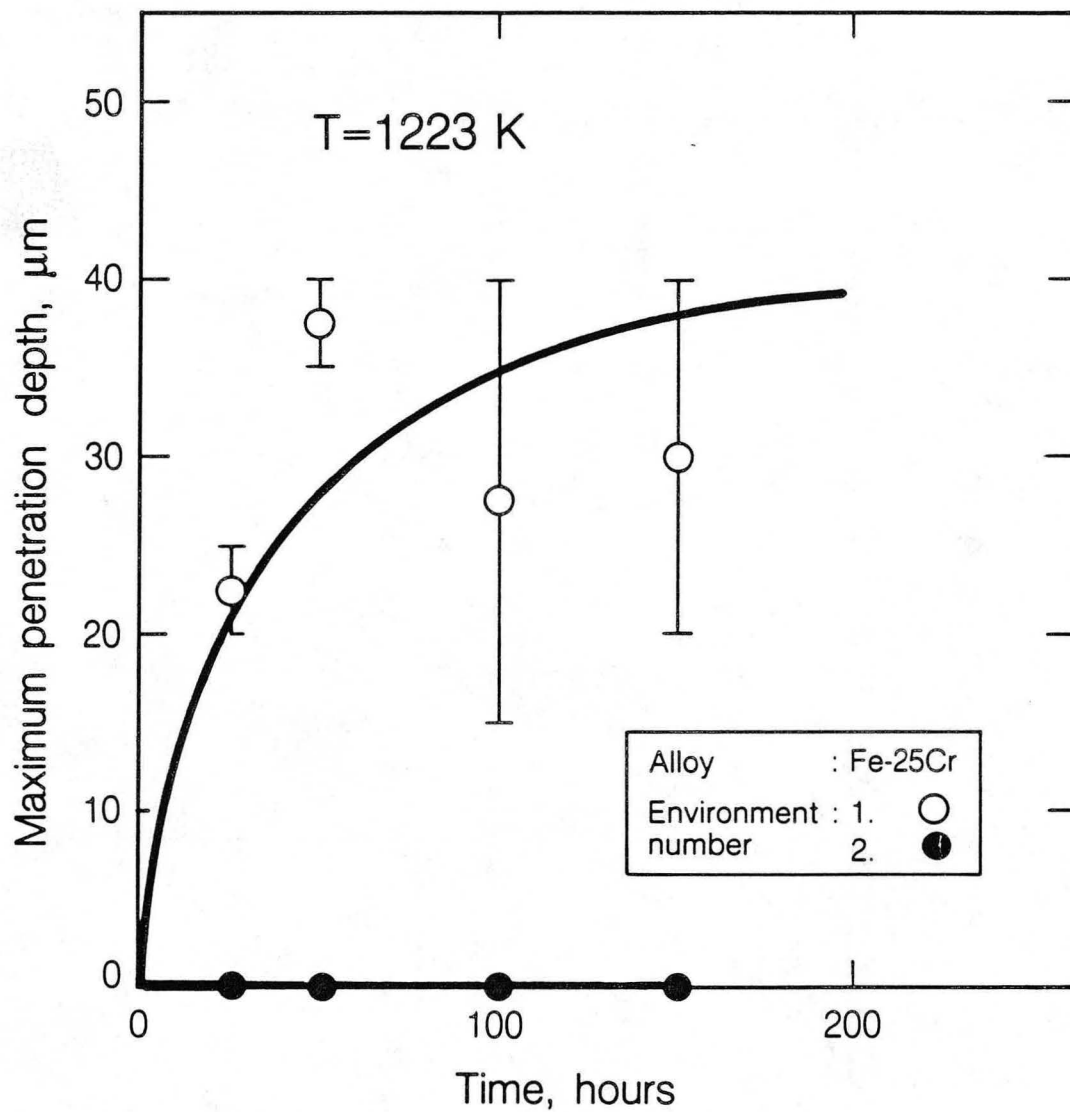
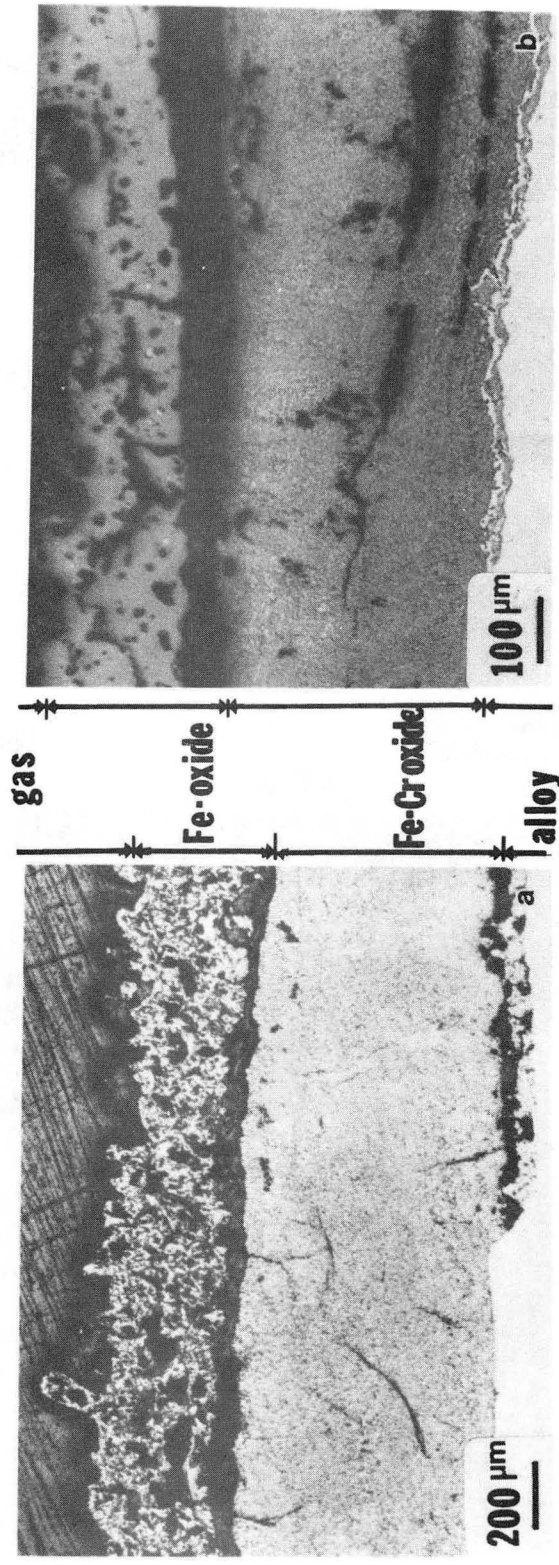


Figure 18b.

XBL 856-10037

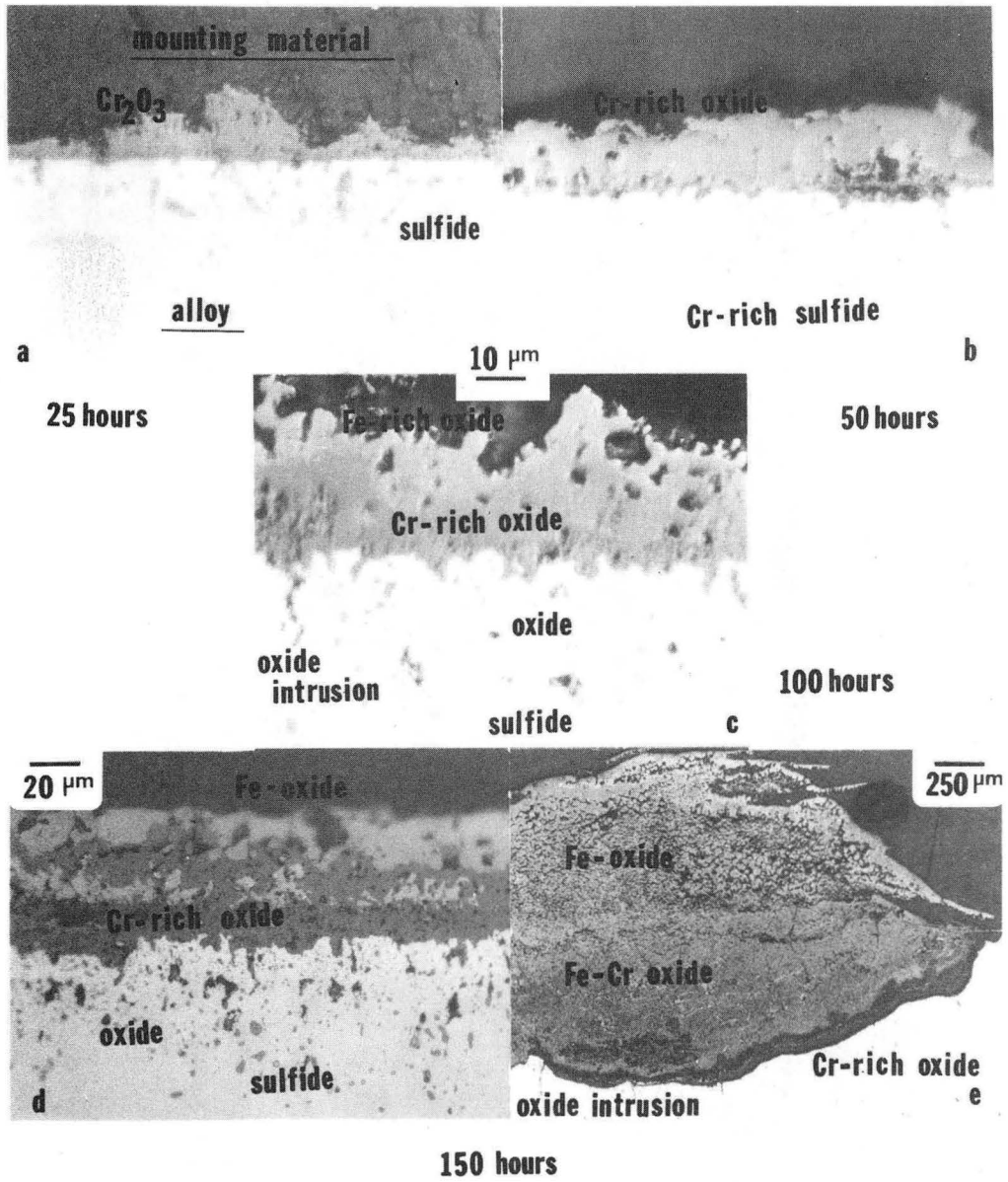


a.  $\log P_{S_2} = -4$

b.  $\log P_{S_2} = -5$

XBB 856-4611

Figure 19.



XBB 856-4562

Figure 20.



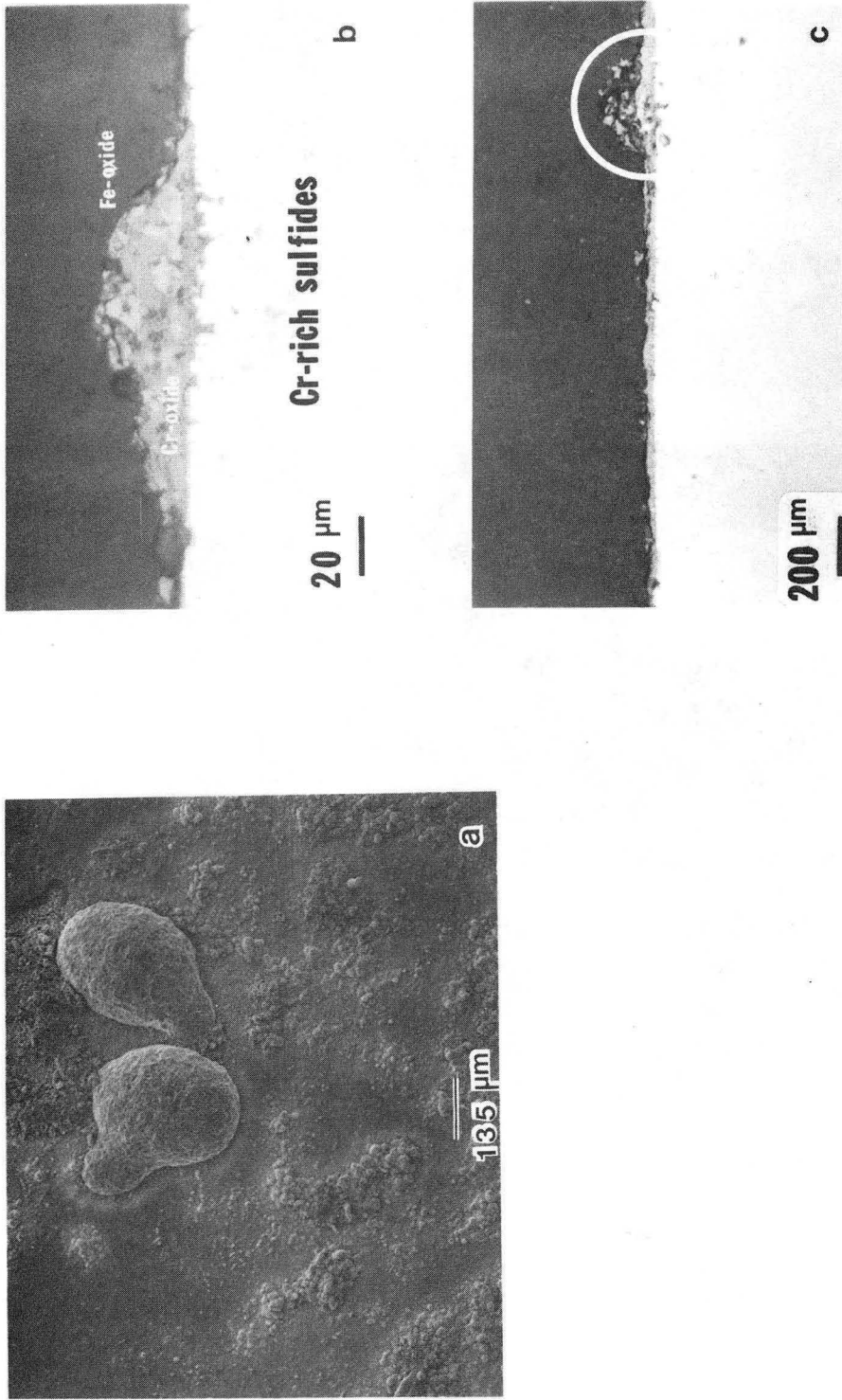
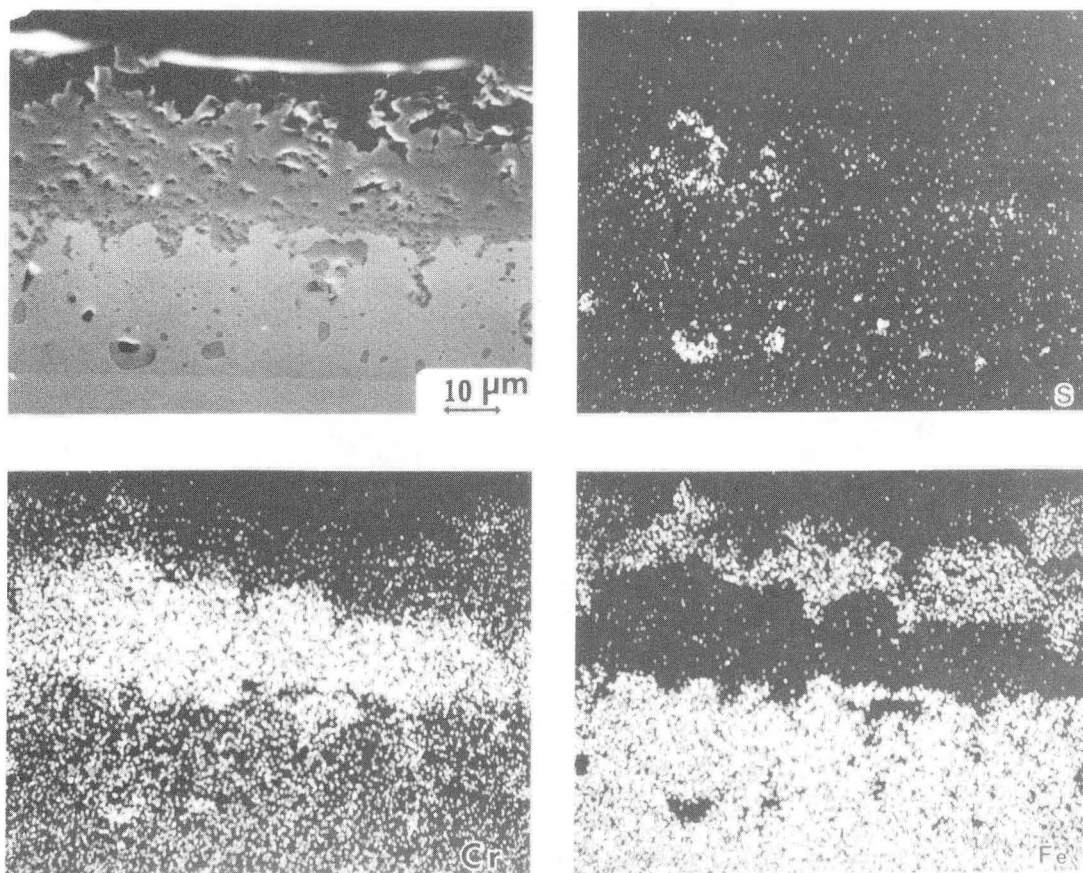


Figure 21.

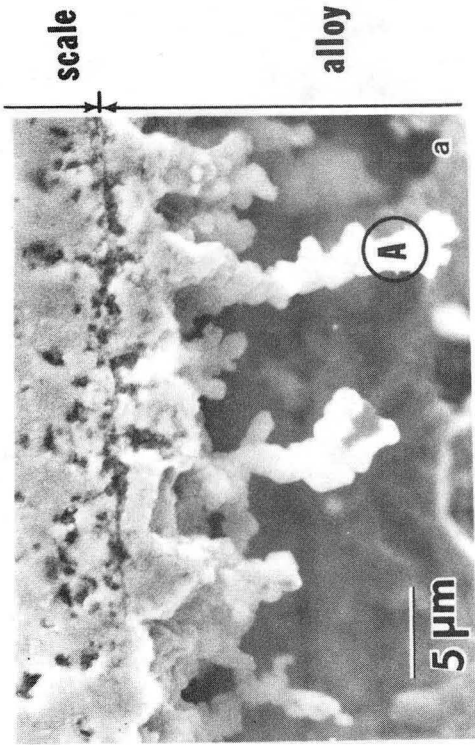
XBB 856-4582



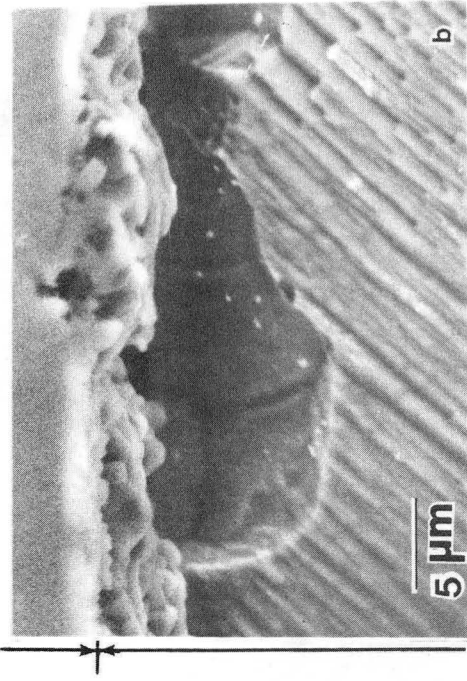
XBB 856-4560

Figure 22.

a.  $\log P_{S_2} = -4$



b.  $\log P_{S_2} = -5$



XBB 856-4606

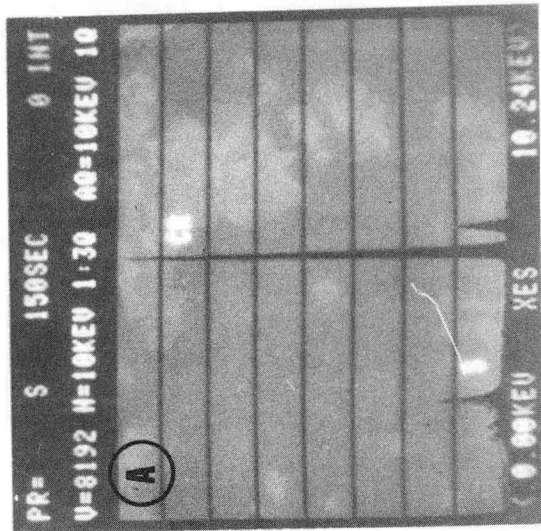
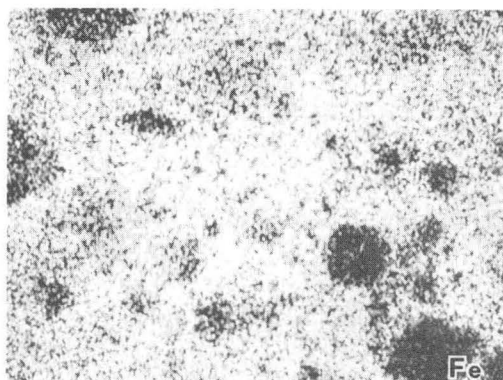
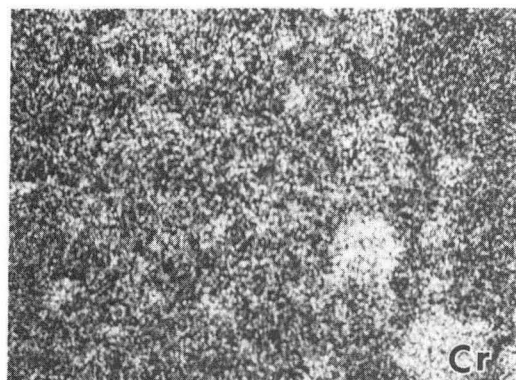
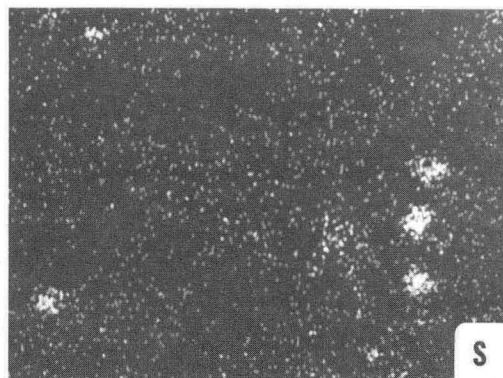
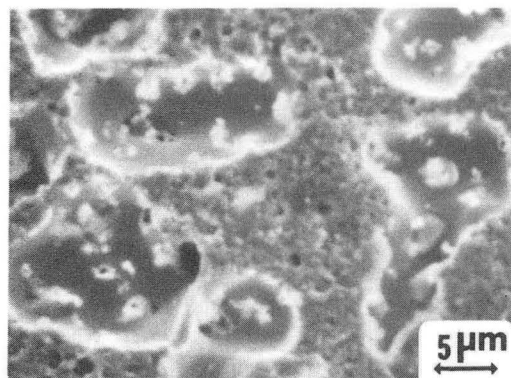
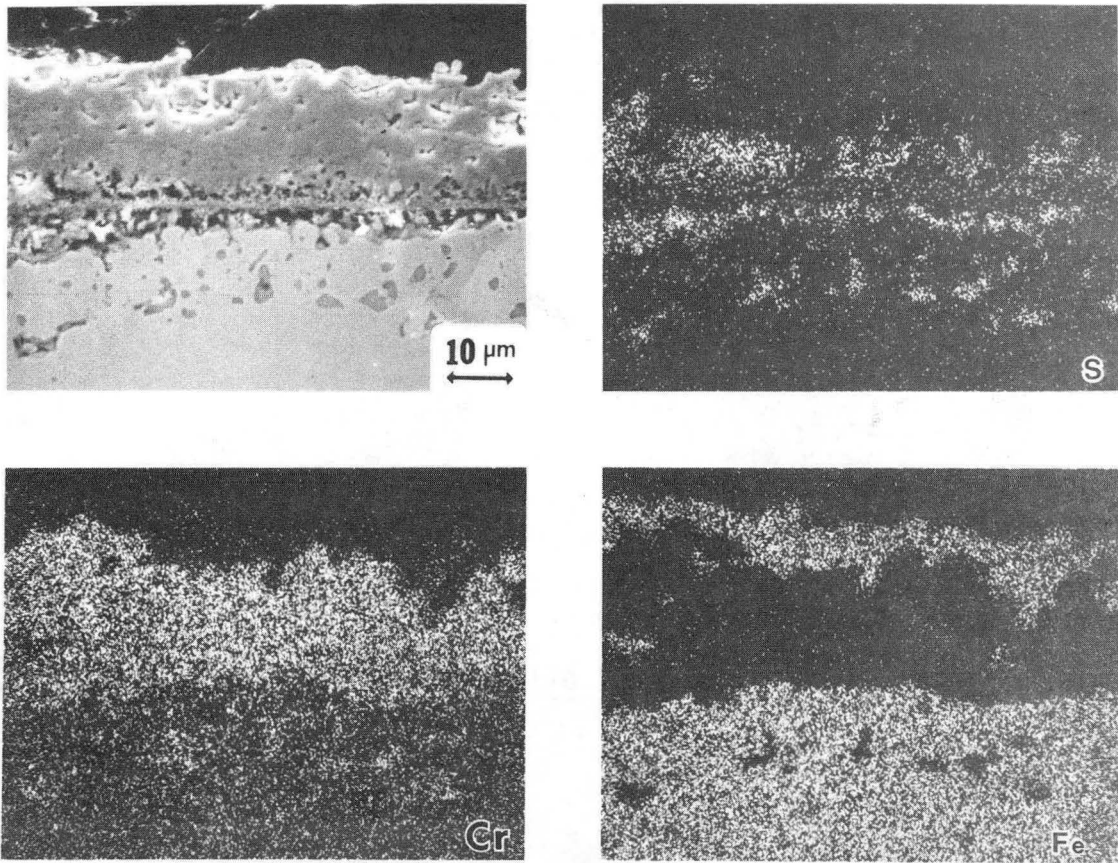


Figure 23.



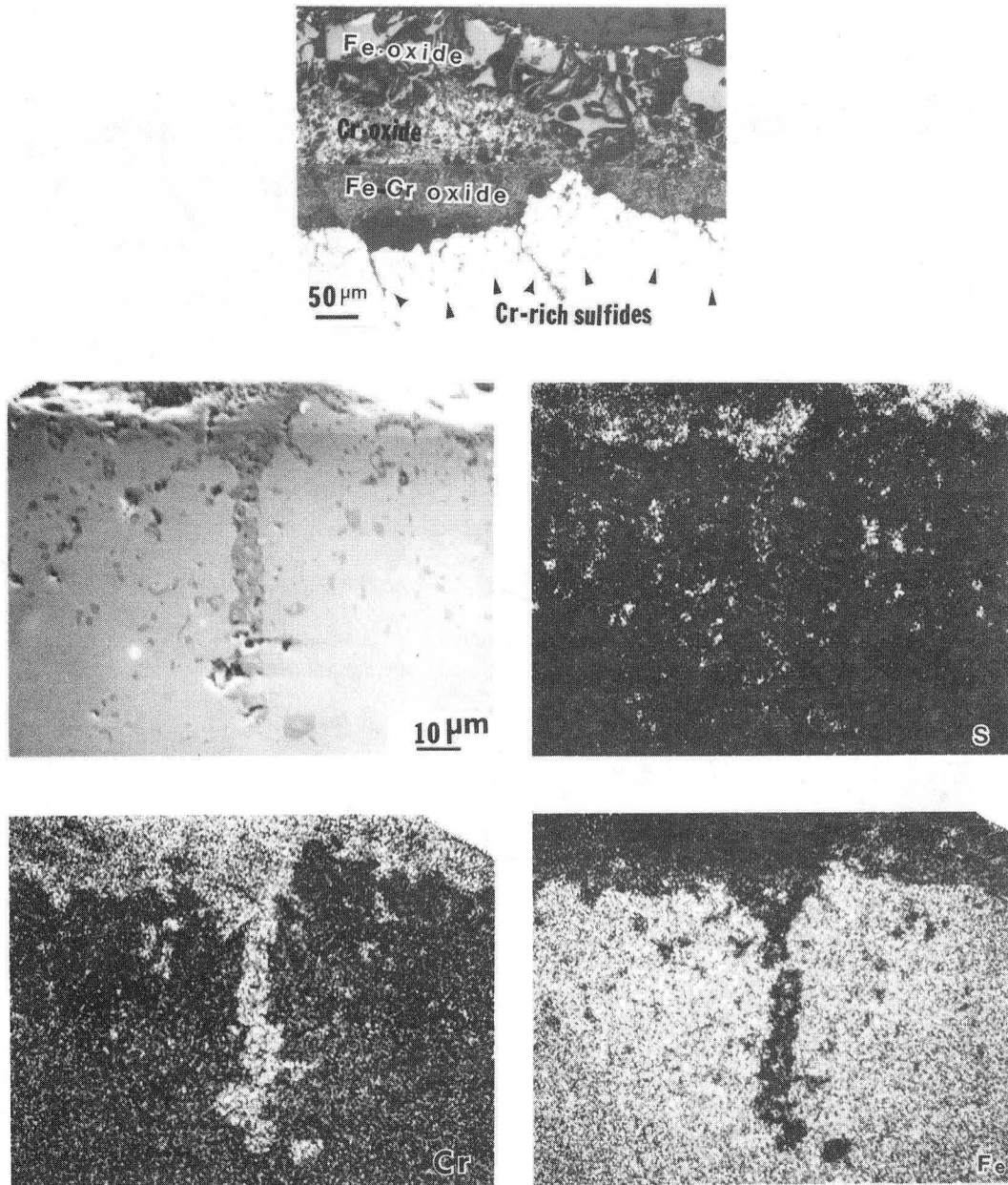
XBB 856-4555

Figure 24.



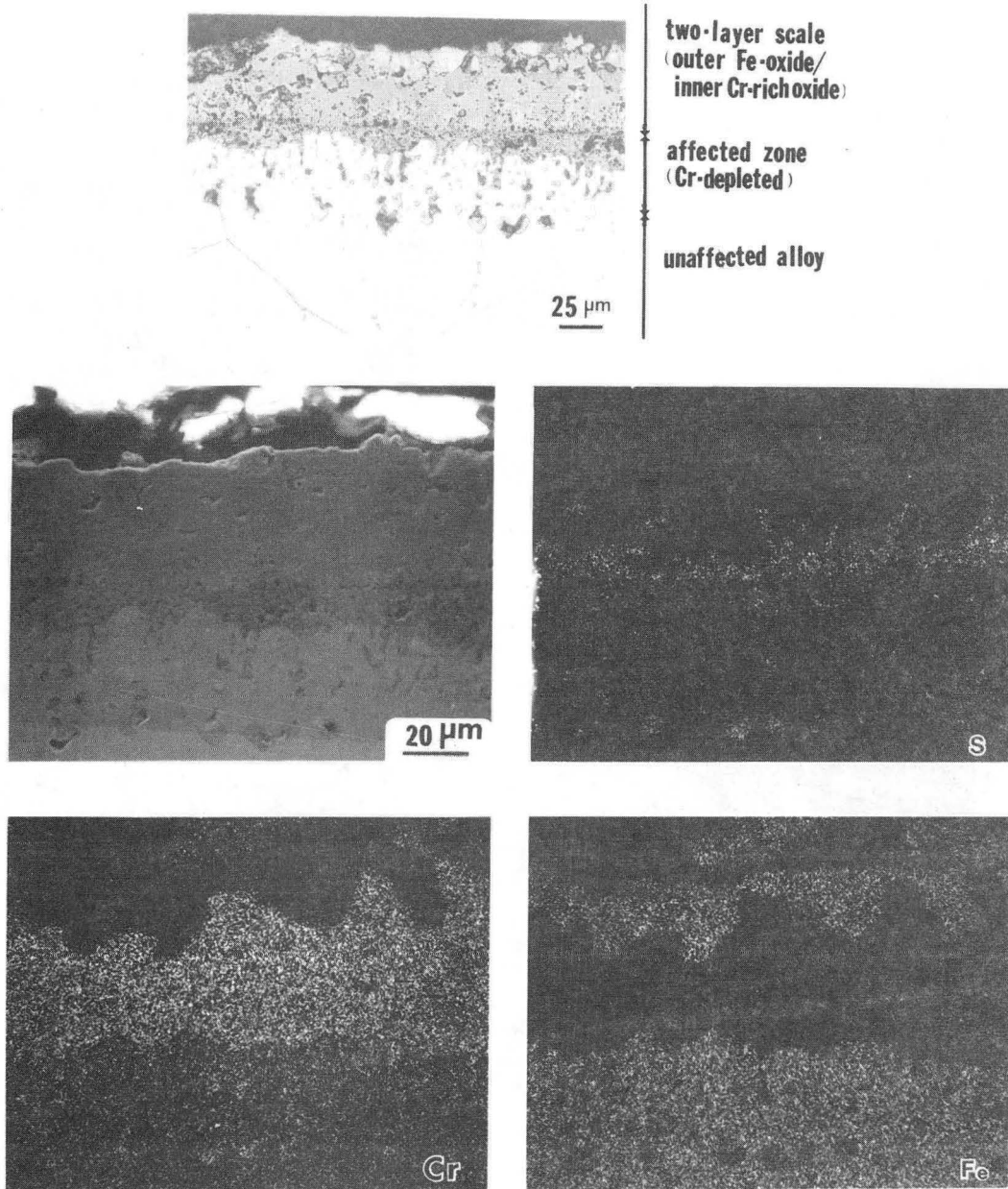
XBB 856-4557

Figure 25.



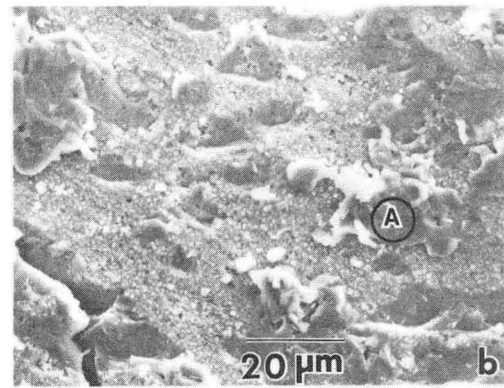
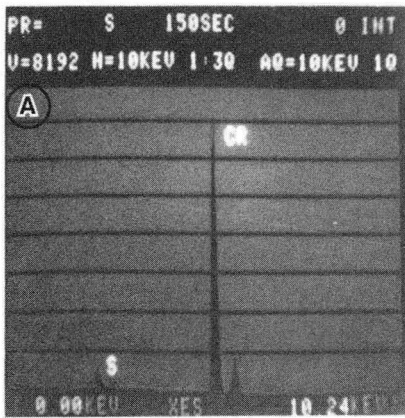
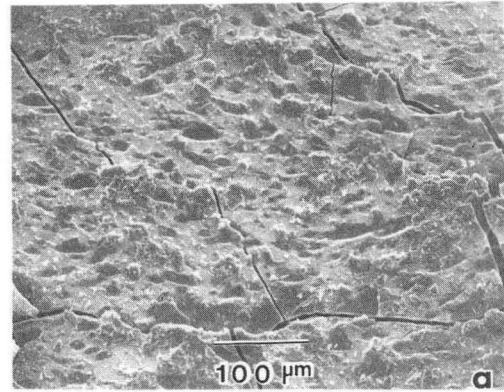
XBB 856-4578

Figure 26.



XBB 856-4609

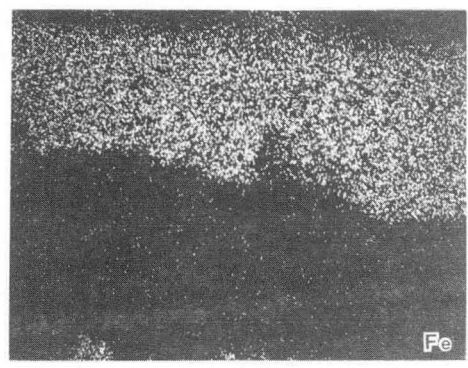
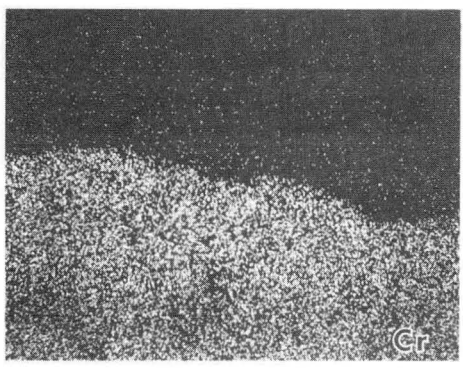
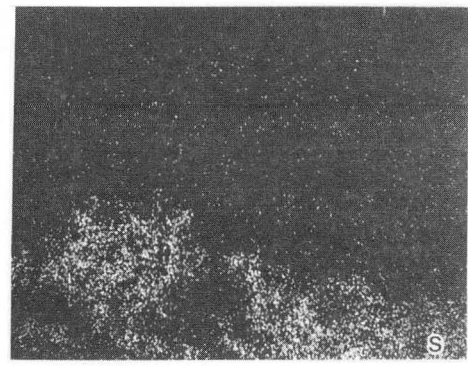
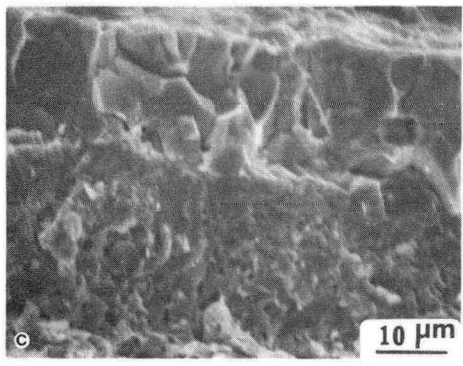
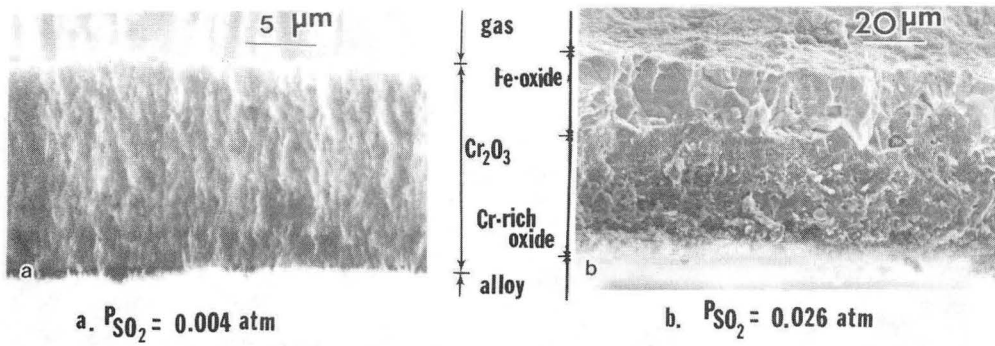
Figure 27.



XBB 856-4561

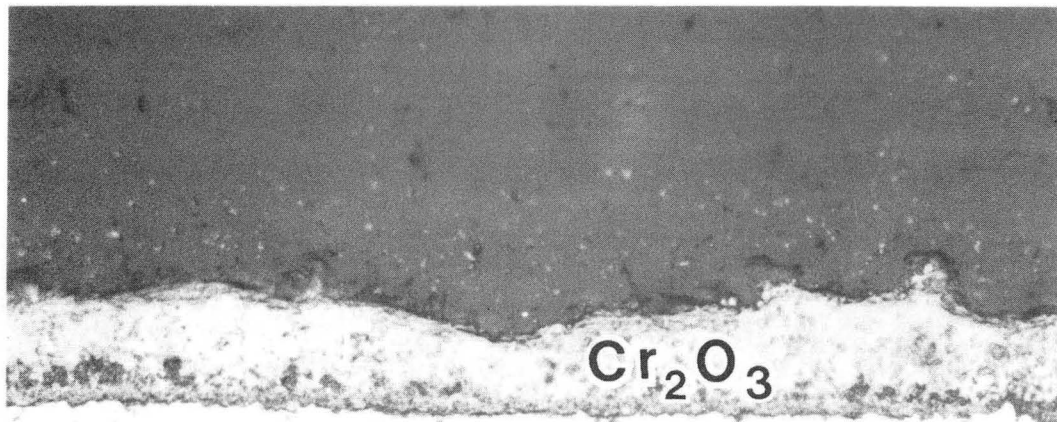
Figure 28.





XBB 856-4610

Figure 29.



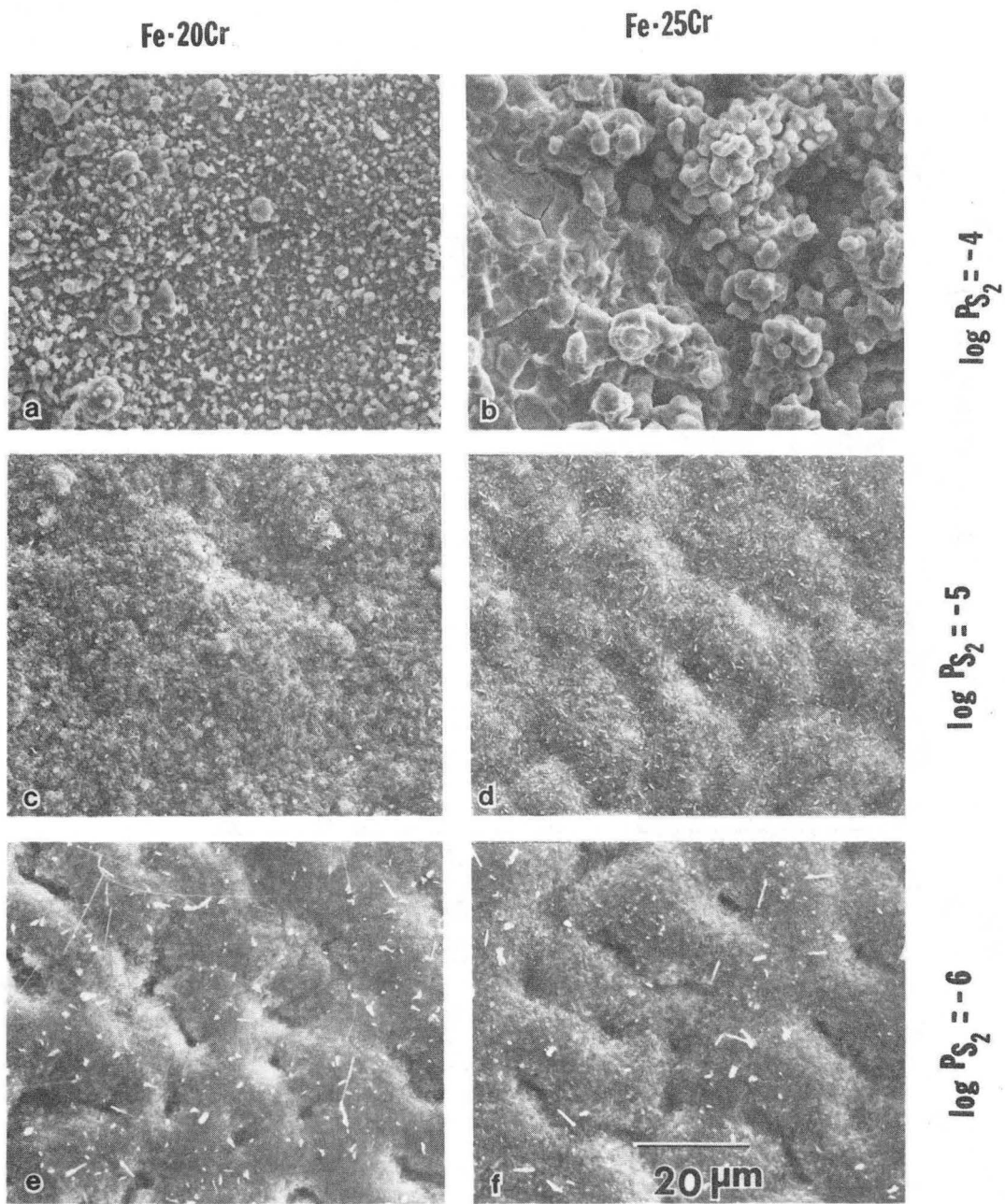
**Cr-rich sulfides**

**Alloy**

**20  $\mu\text{m}$**

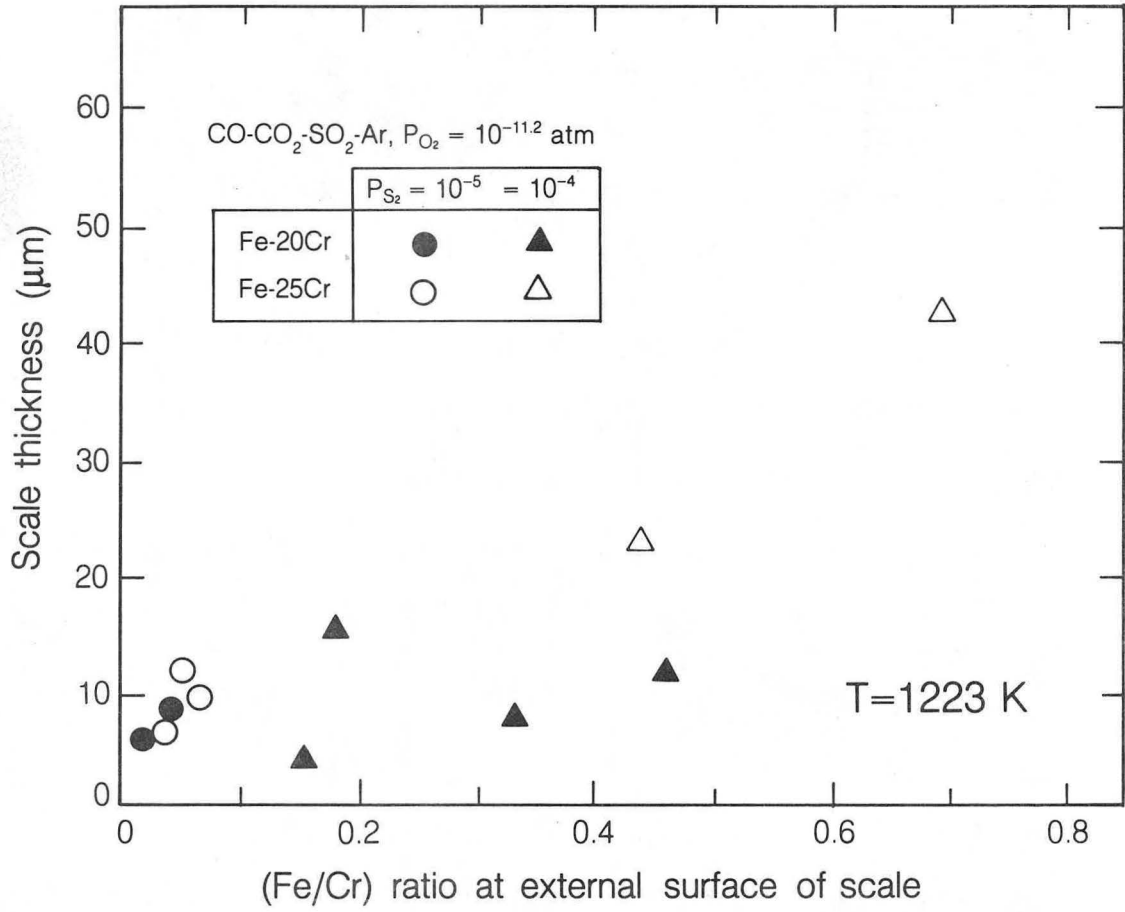
XBB 856-4581

Figure 30.



XBB 856-4607

Figure 31.

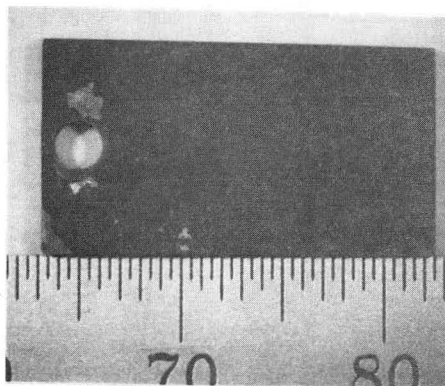
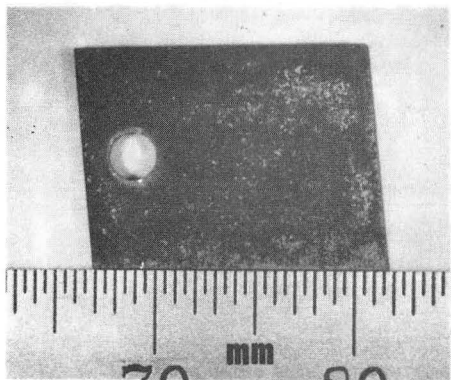


XBL 856-10012

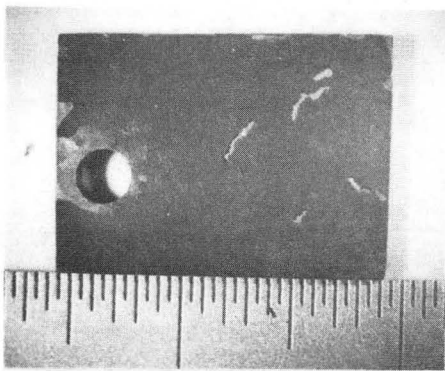
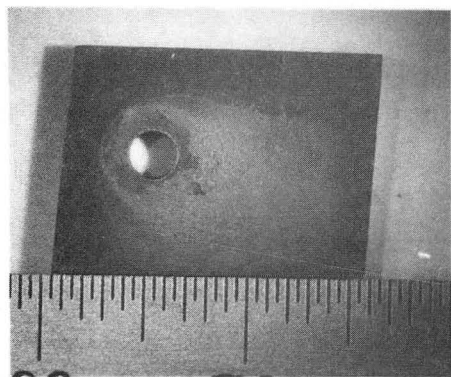
Figure 32.

Fe-20Cr

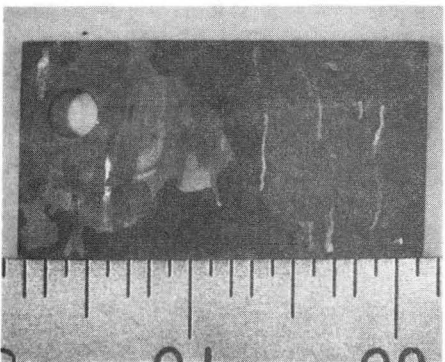
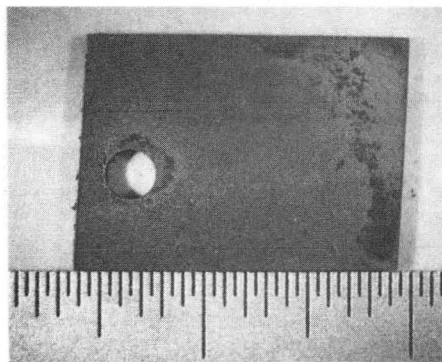
Fe-25Cr



$\log P_{S_2} = -4$



$\log P_{S_2} = -5$

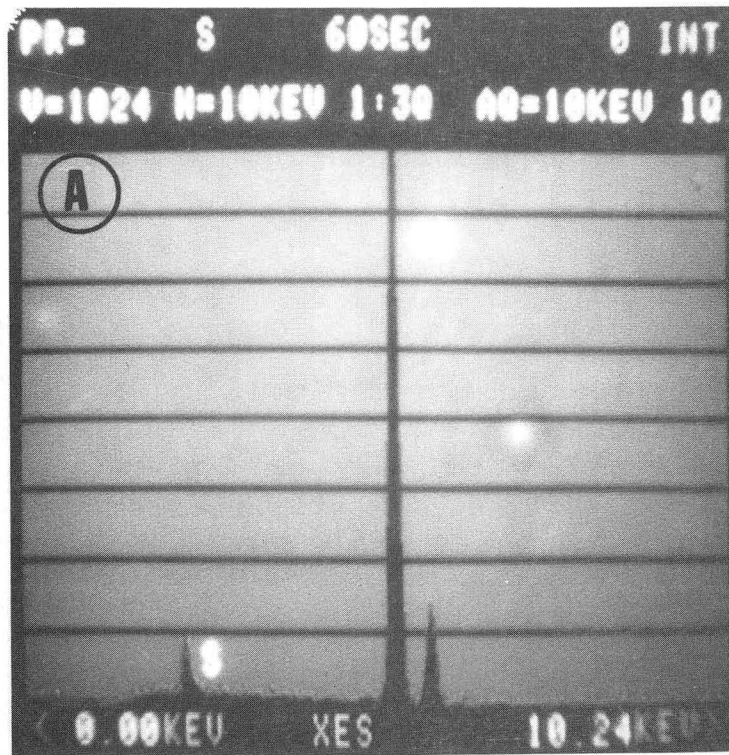
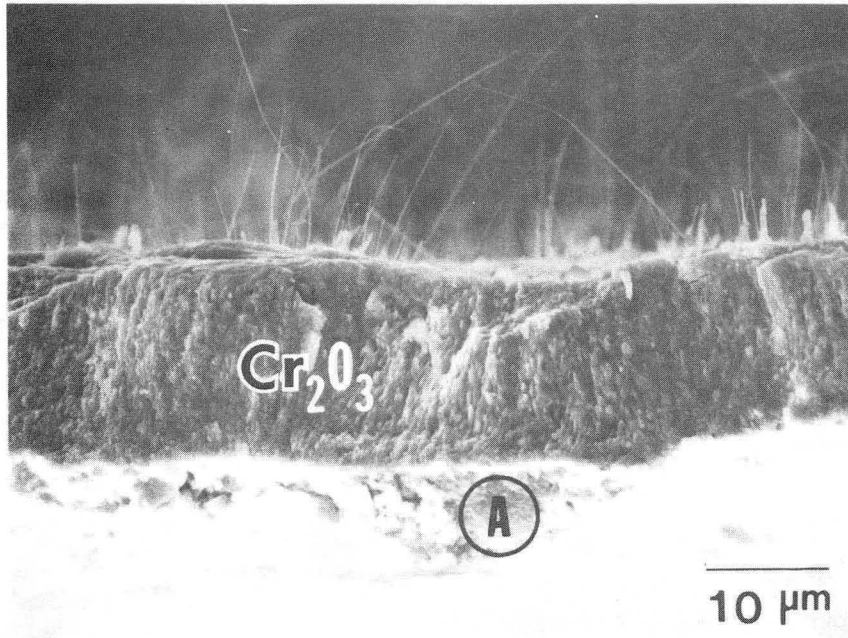


$\log P_{S_2} = -6$

100 hours oxidation

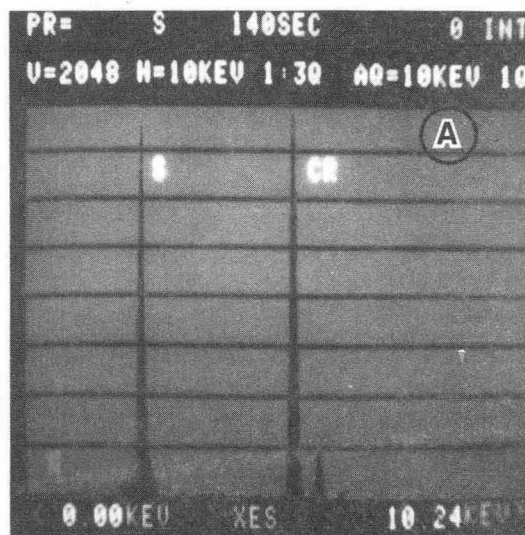
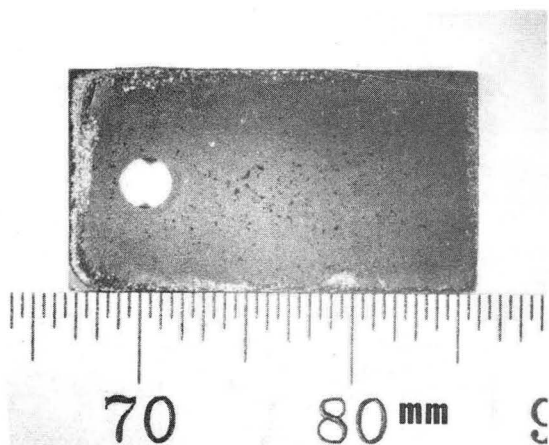
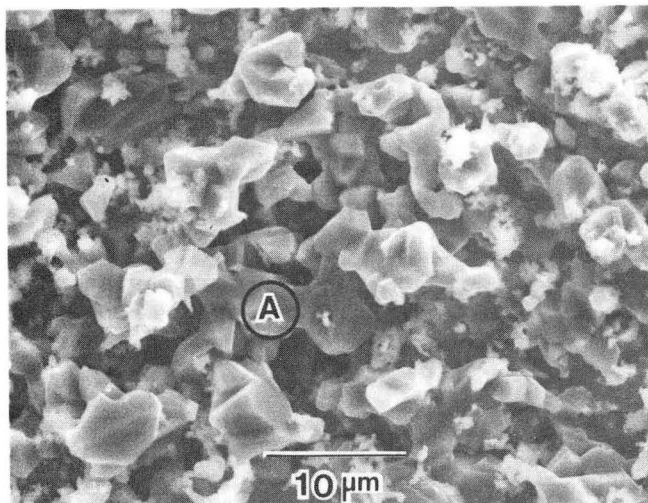
XBB 856-4576

Figure 33.



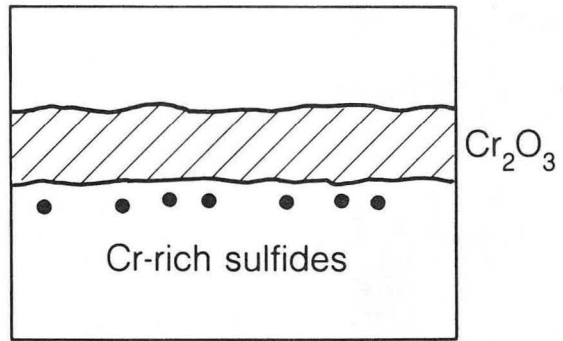
XBB 856-4563

Figure 34.

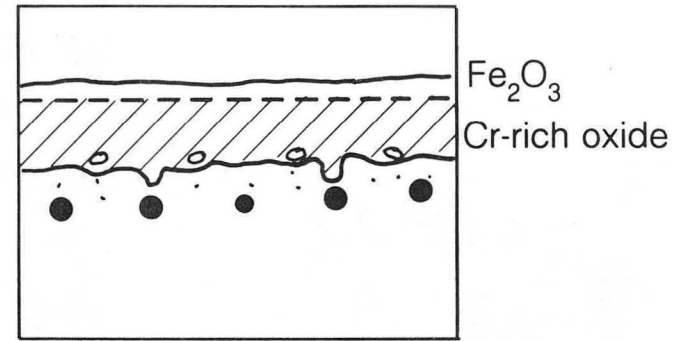


XBB 856-4566

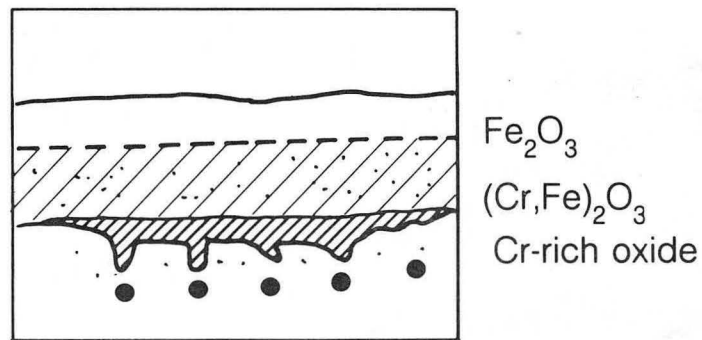
Figure 35.



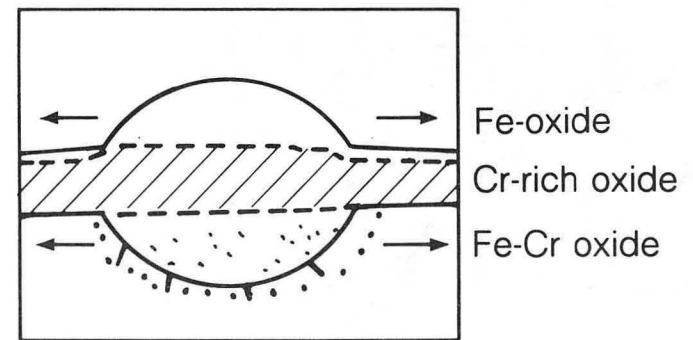
(i)



(ii)



(iii)

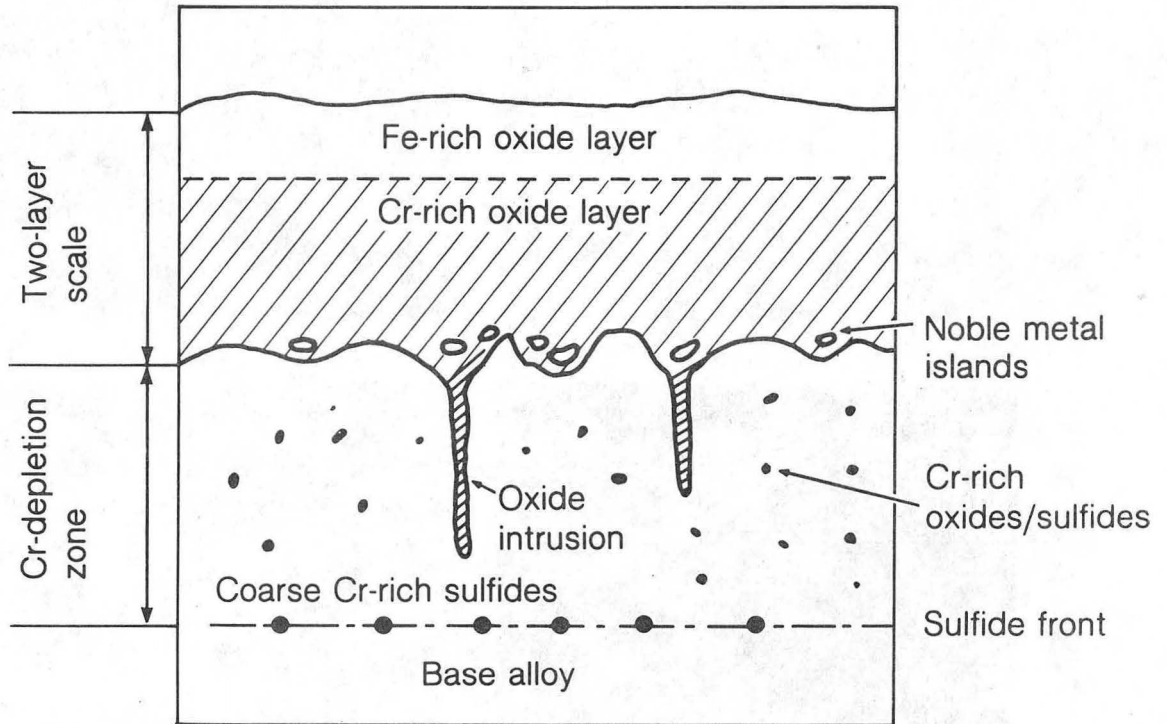


(iv)

Figure 36.

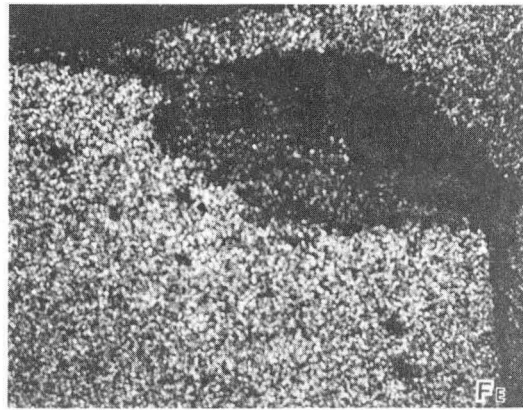
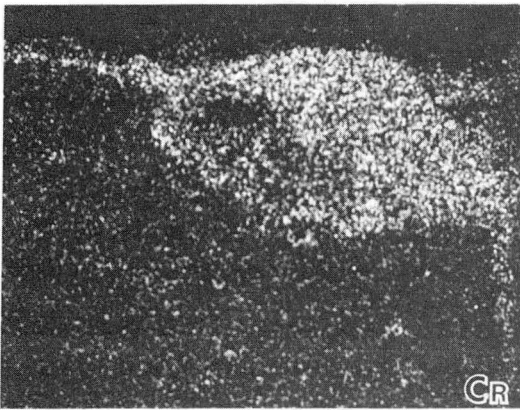
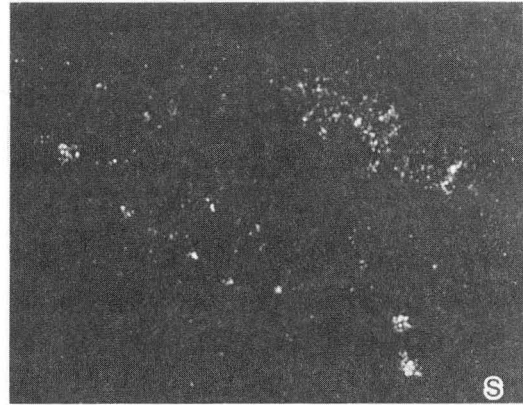
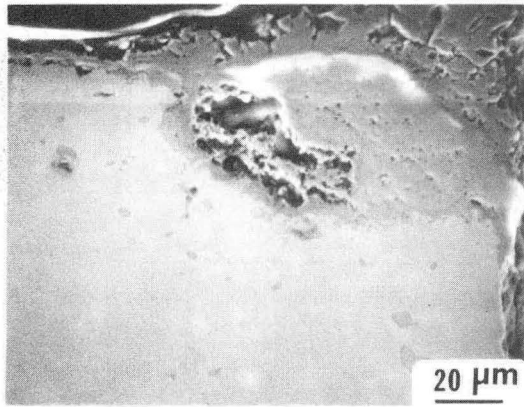
XBL 856-10013





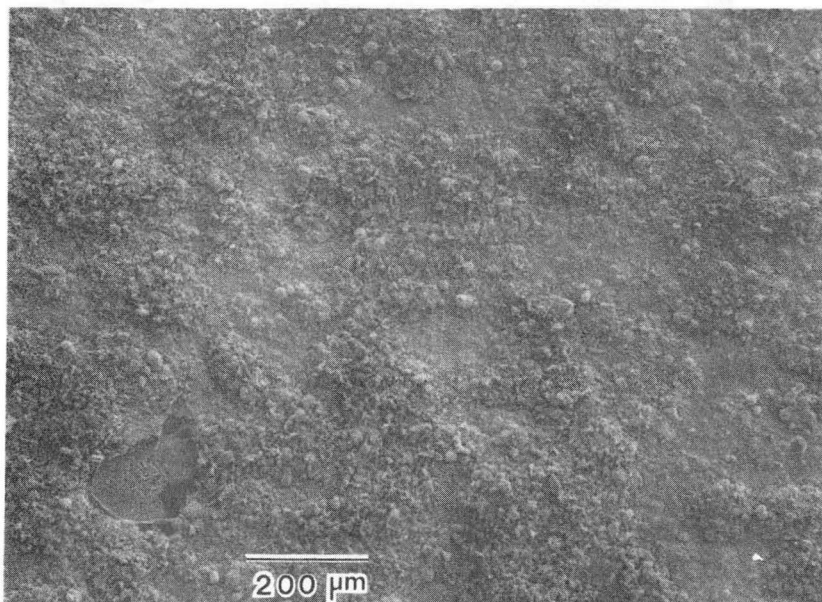
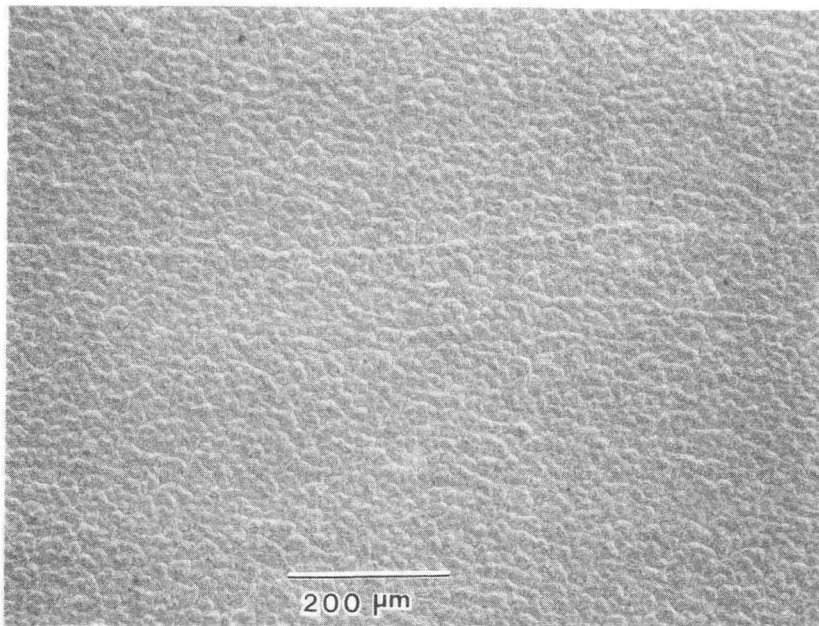
XBL 856-10006

Figure 37.



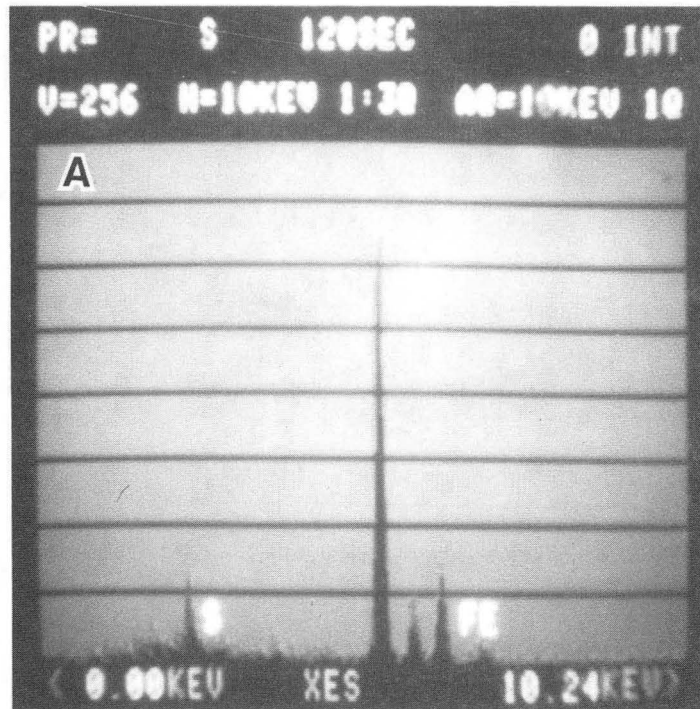
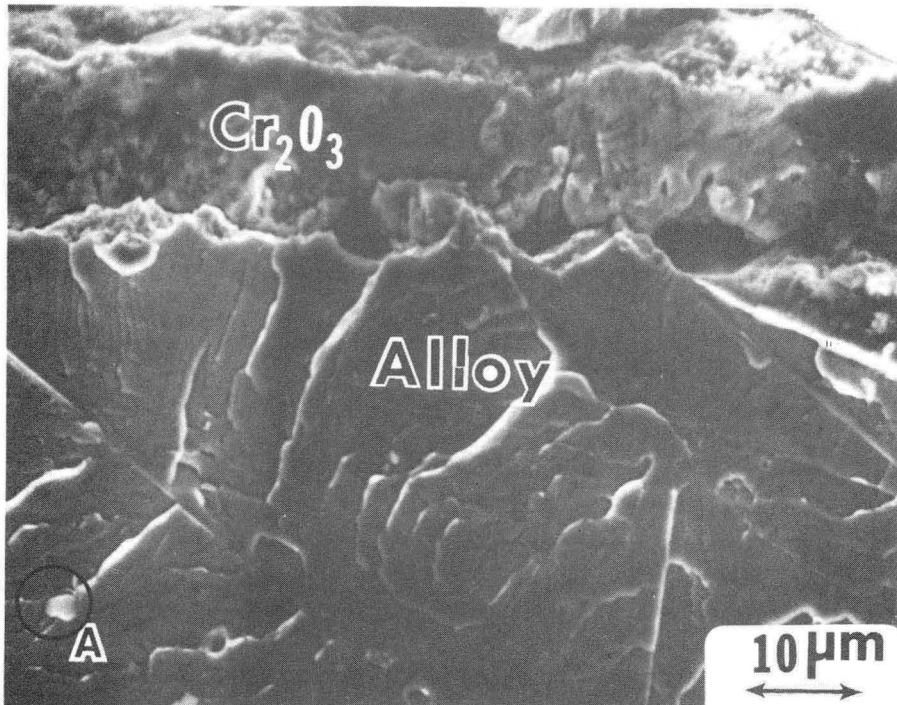
XBB 856-4559

Figure 38.



XBB 856-4565

Figure 39.



XBB 856-4564

Figure 40.

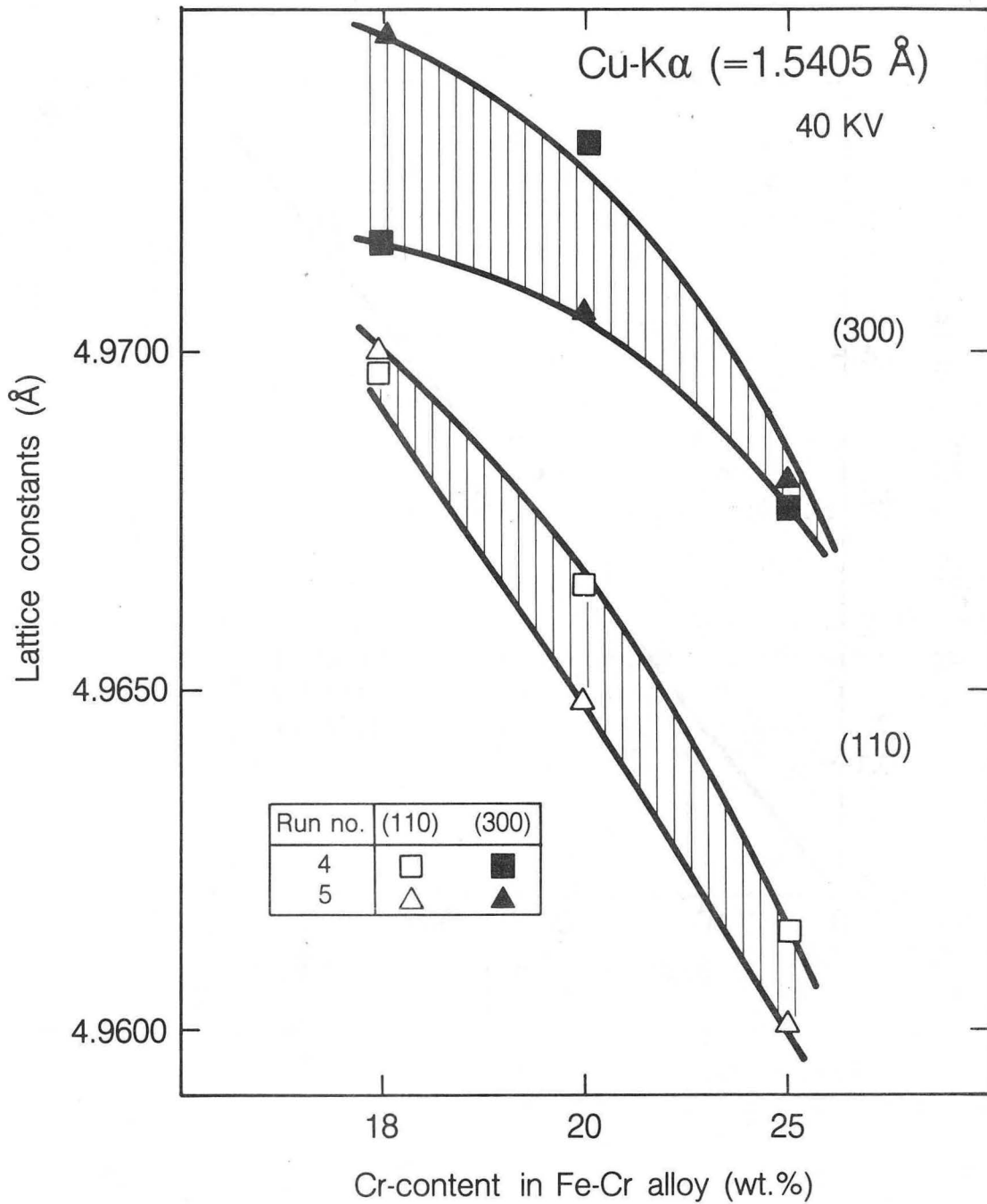
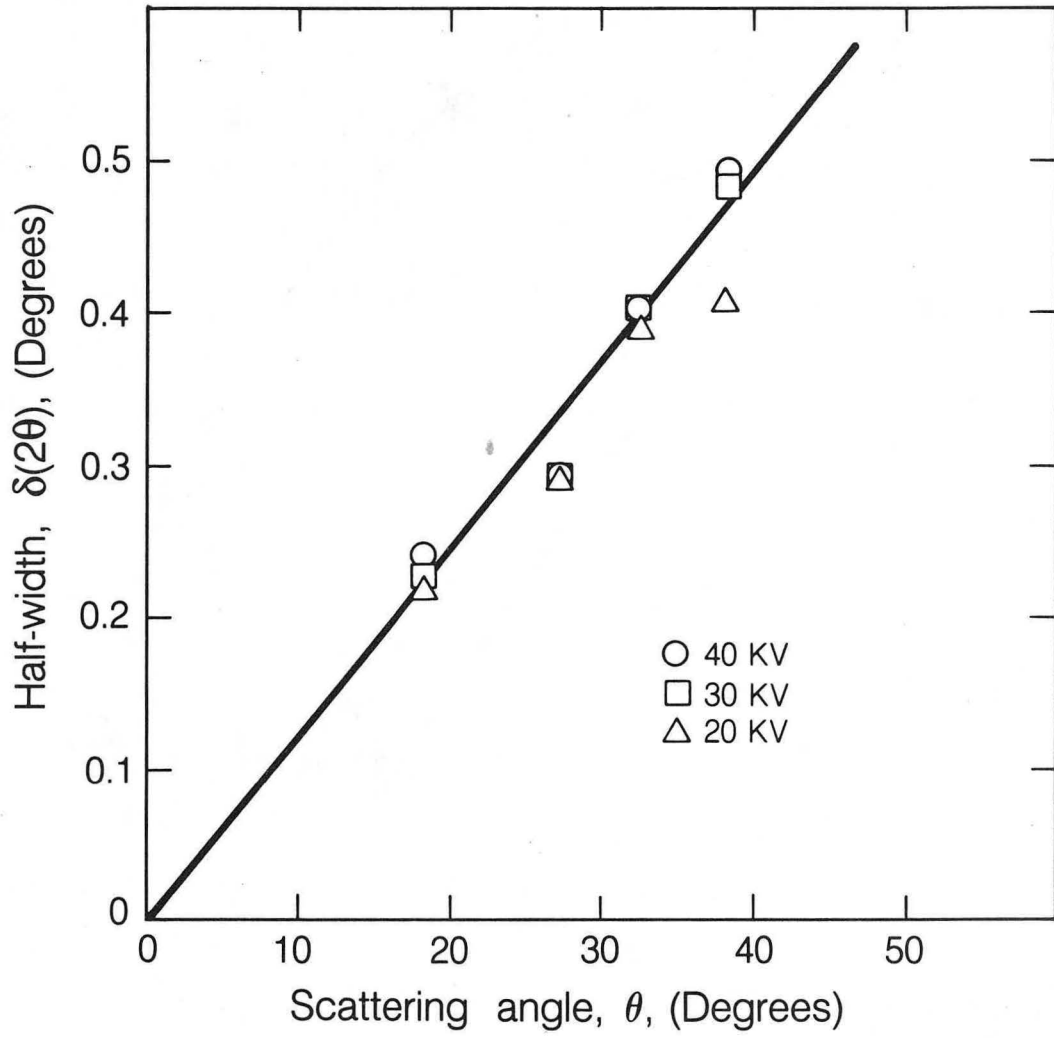


Figure 41.

XBL 856-10033



XBL 856-10032

Figure 42a.

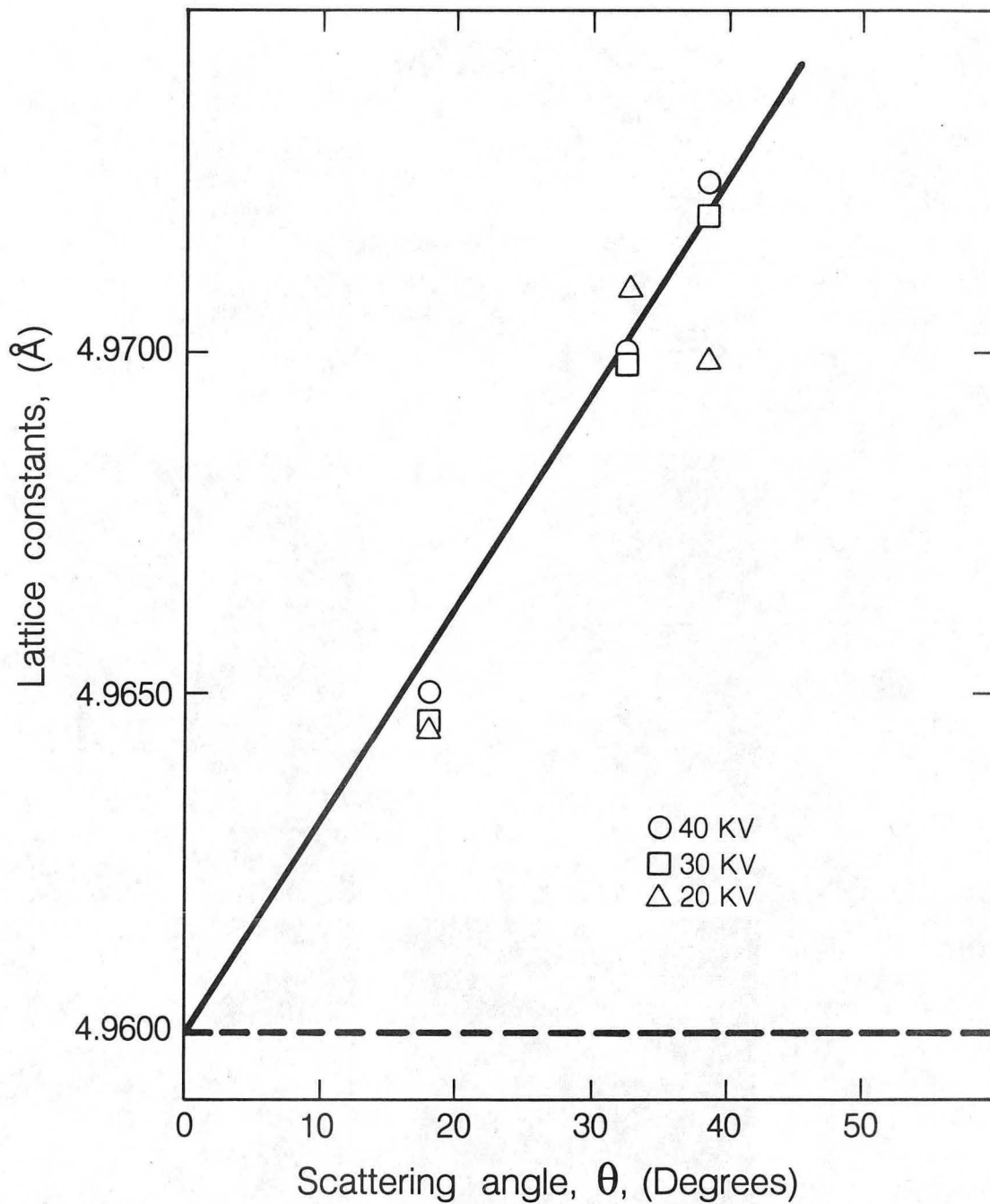
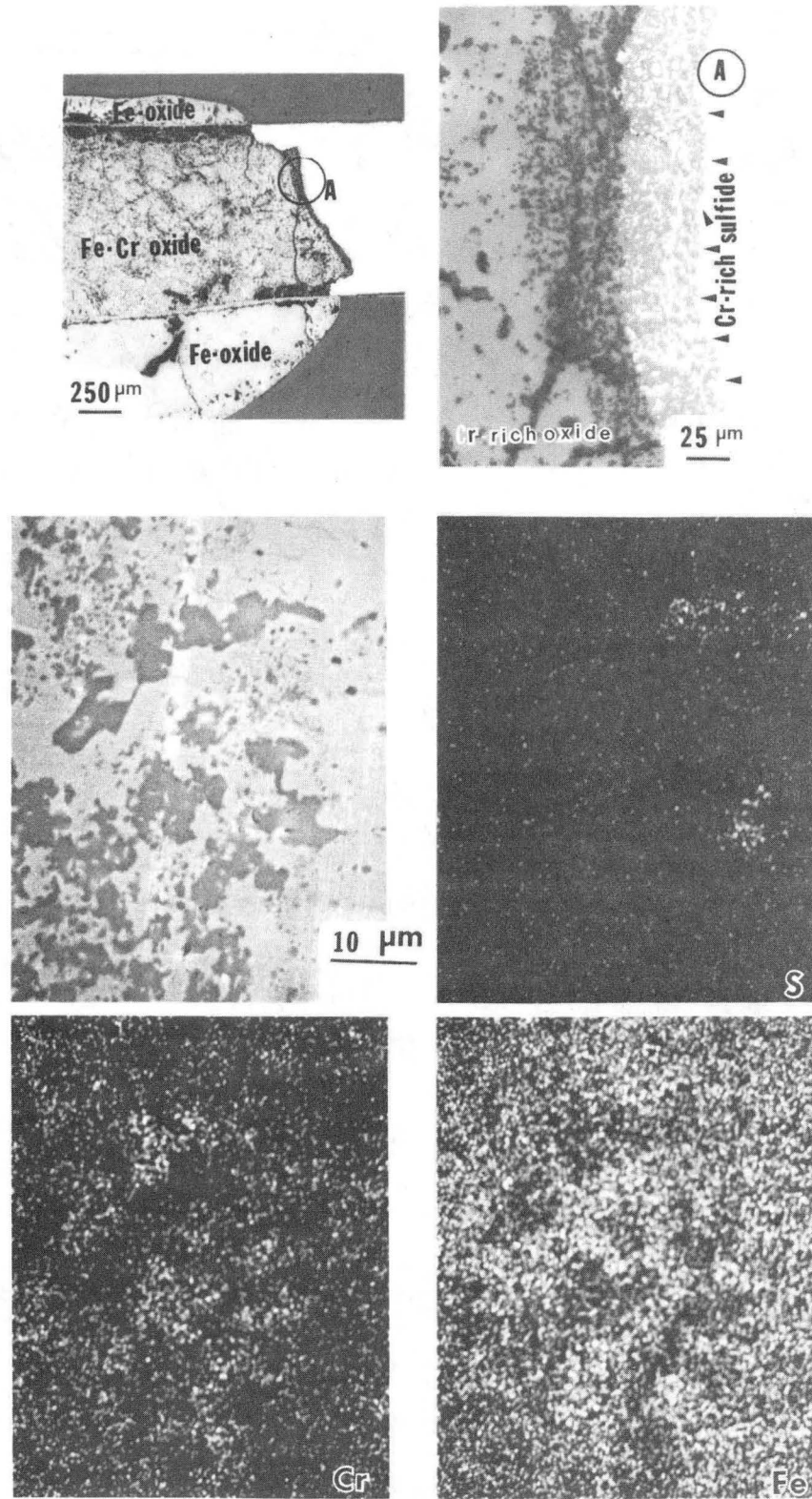


Figure 42b.

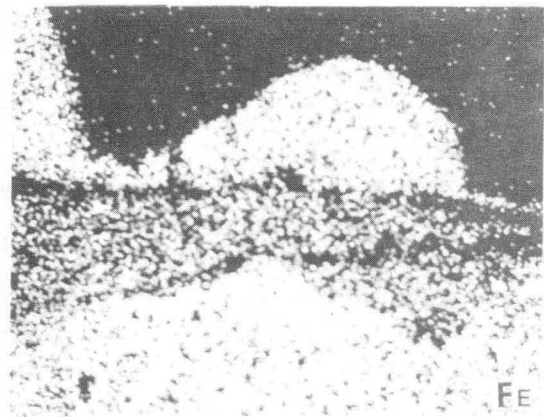
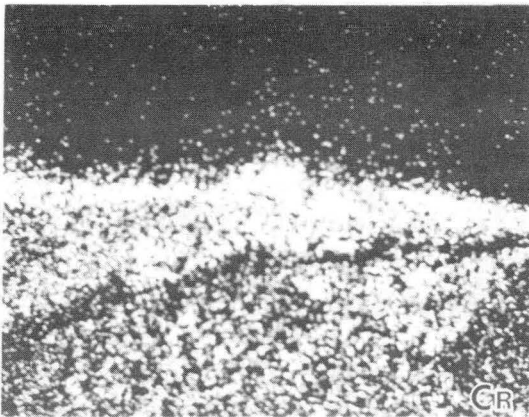
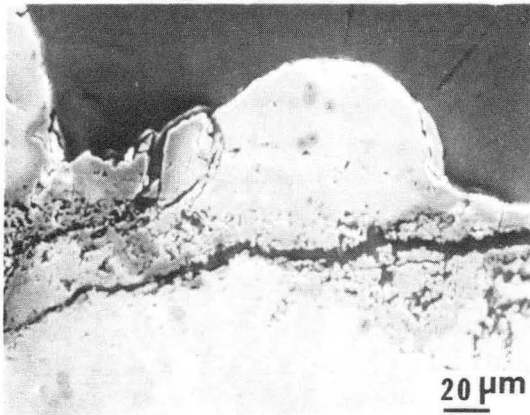
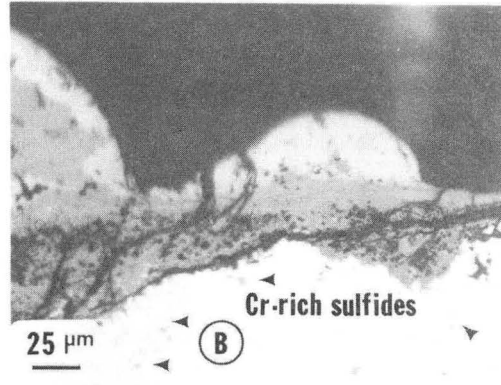
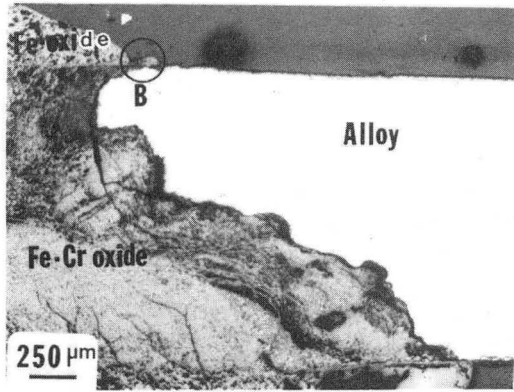
XBL 856-10031



XBB 857-5662

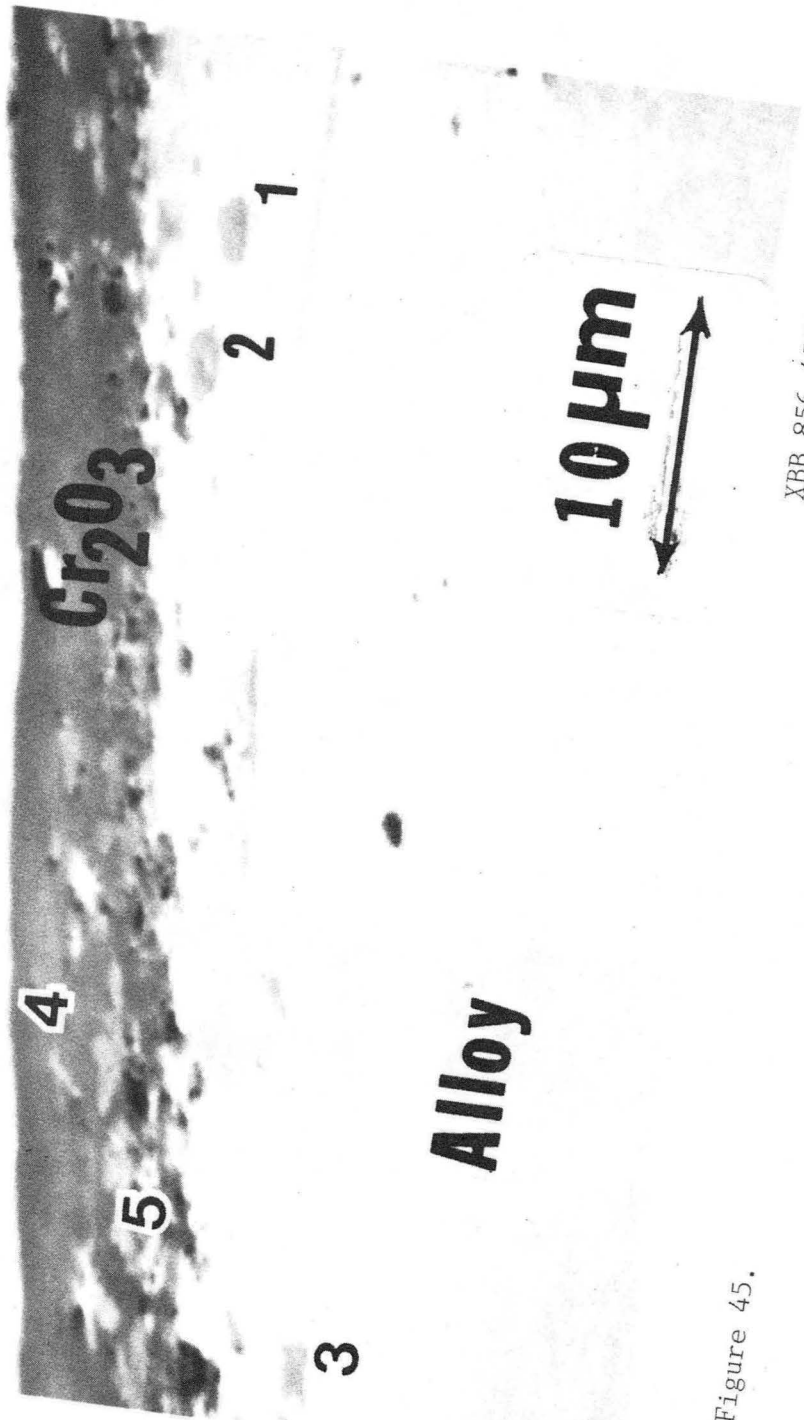
Figure 43.





XBB 856-4580

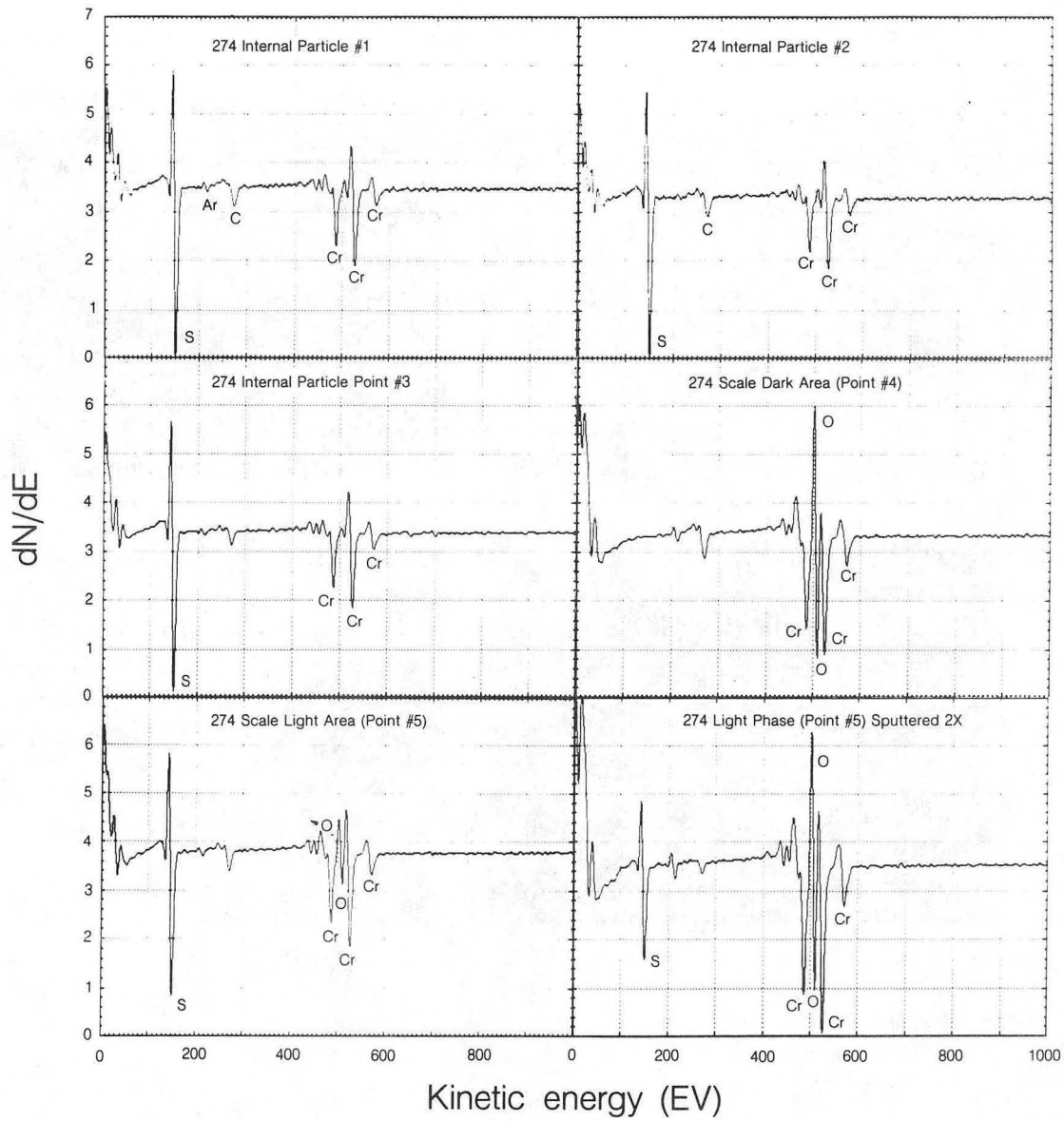
Figure 44.



XBB 856-4554

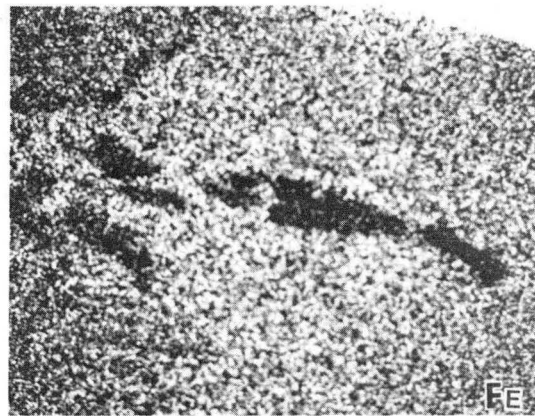
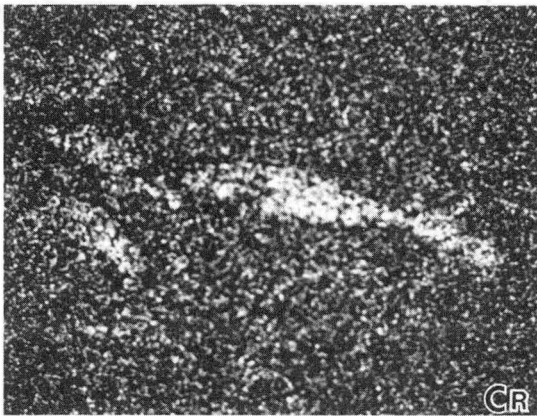
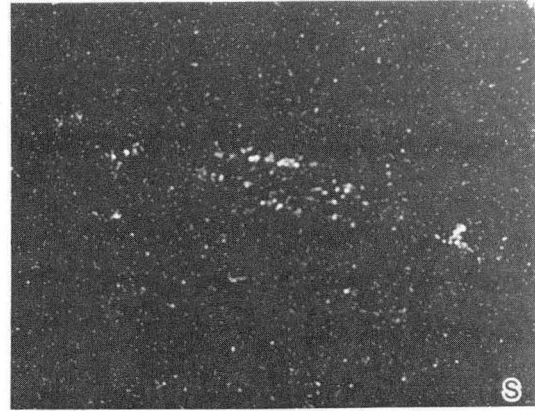
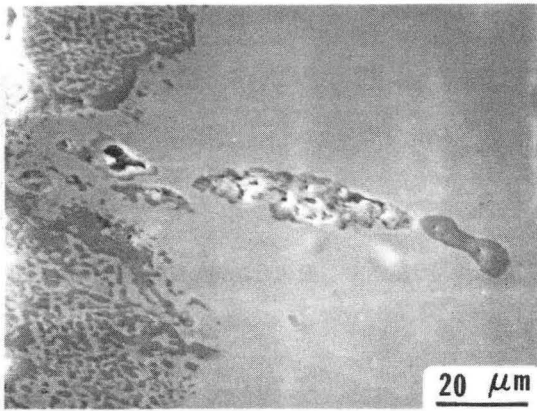
Figure 45.

.....



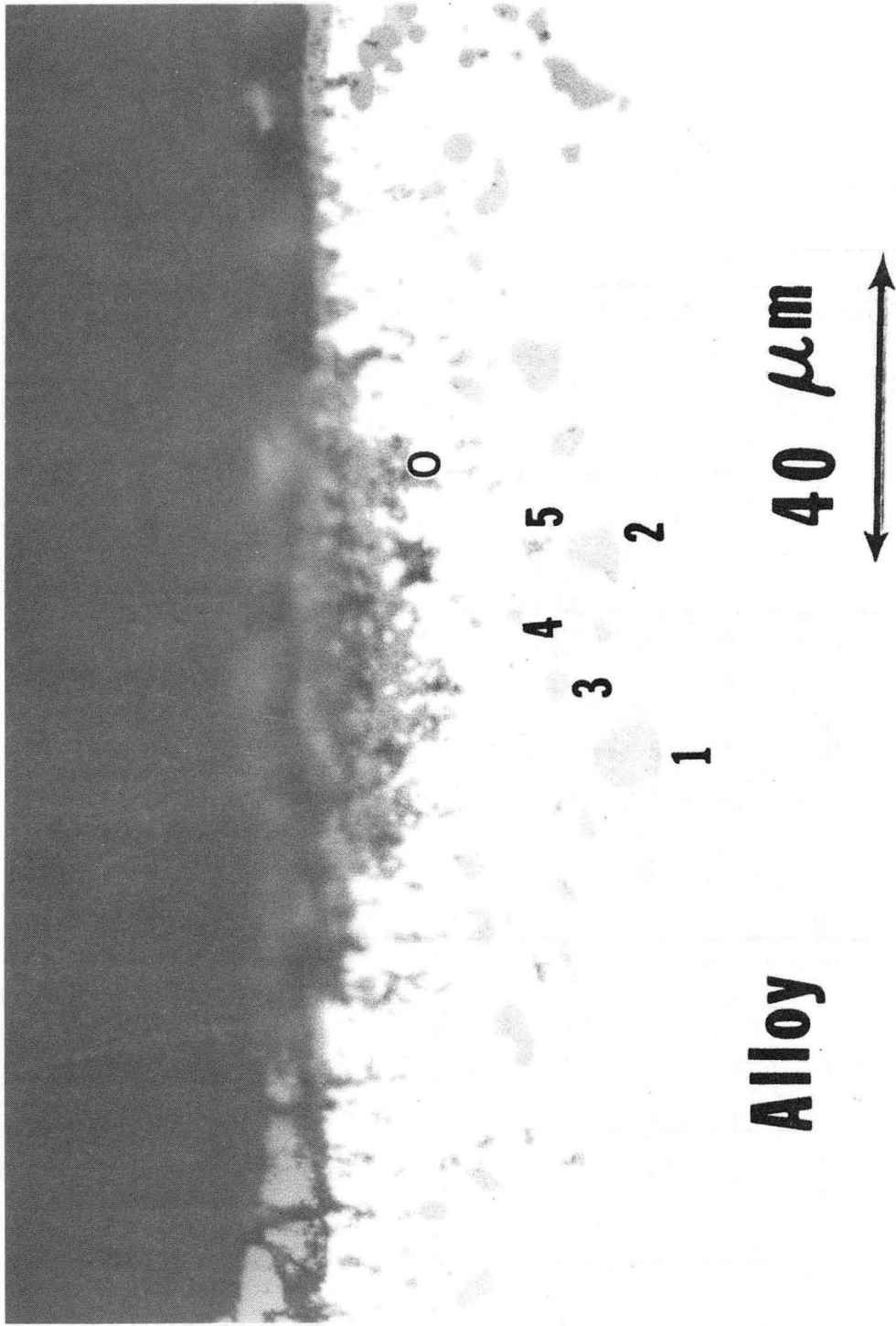
XBL 856-10004

Figure 45b.



XBB 856-4558

Figure 46.



XBB 856-4552

Figure 47a.

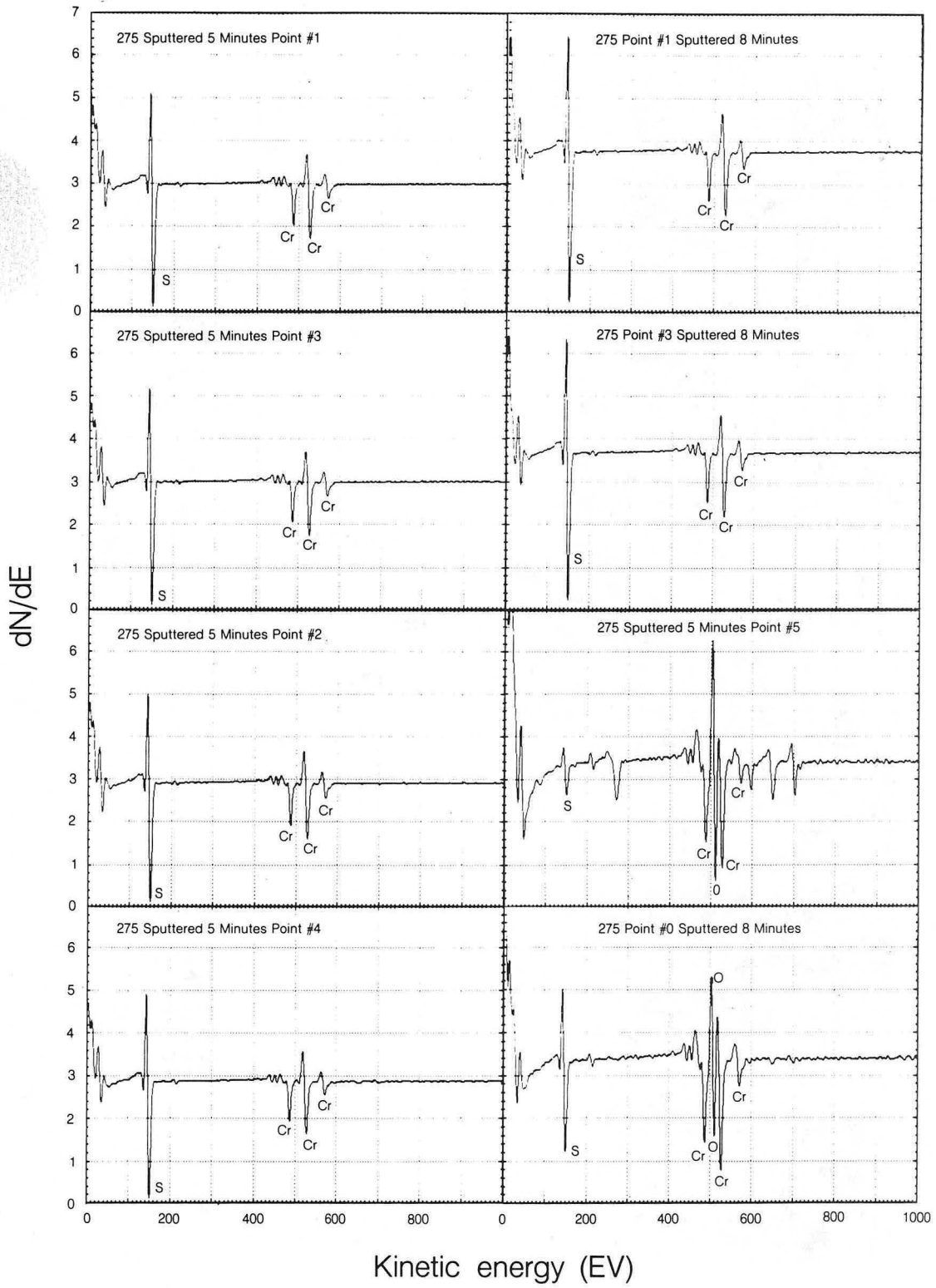


Figure 47b.

XBL 856-10005

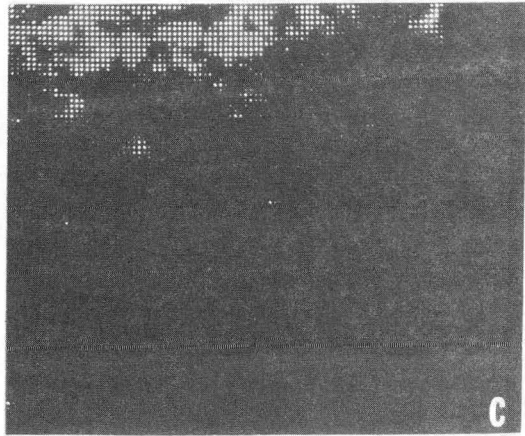
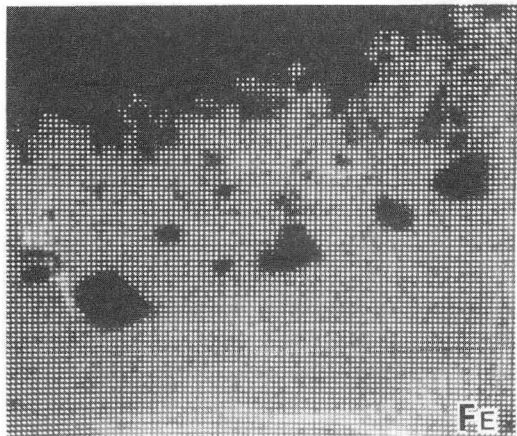
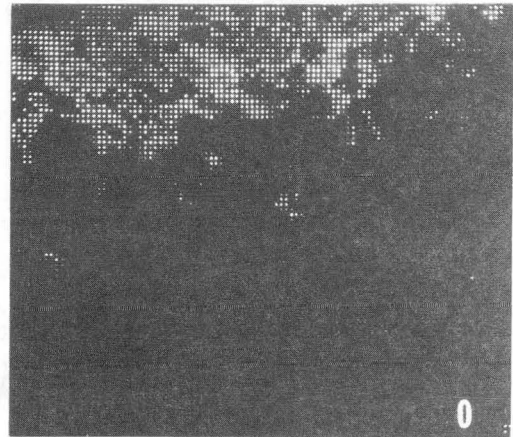
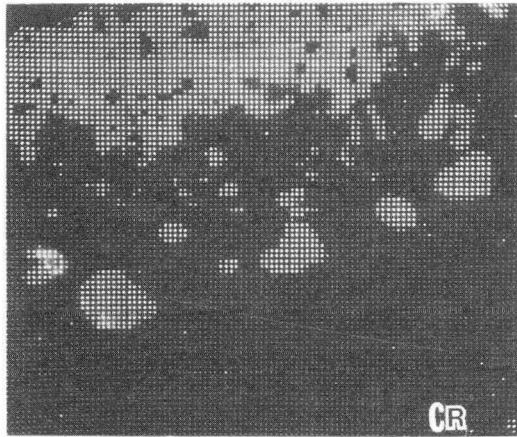
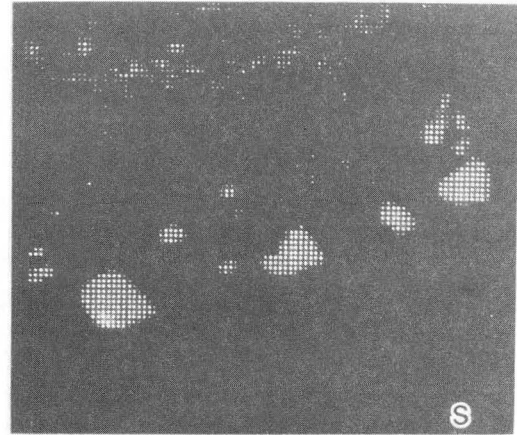
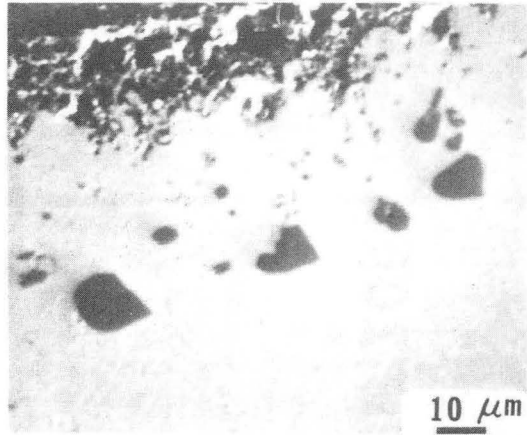
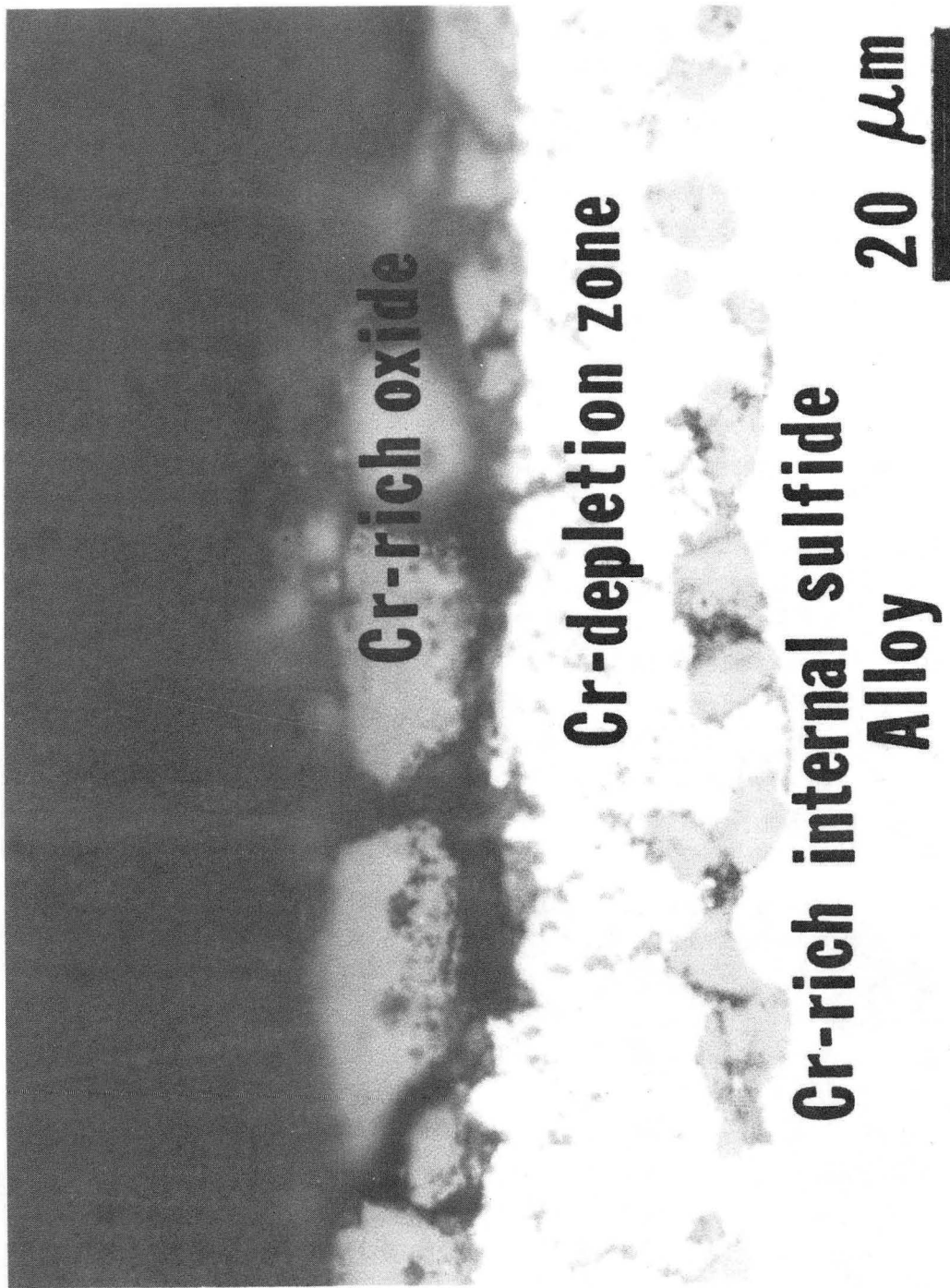


Figure 47c.

XBE 856-4579



XBB 856-4553

Figure 48.



1. Transport of sulfur in the protective chromium oxide.

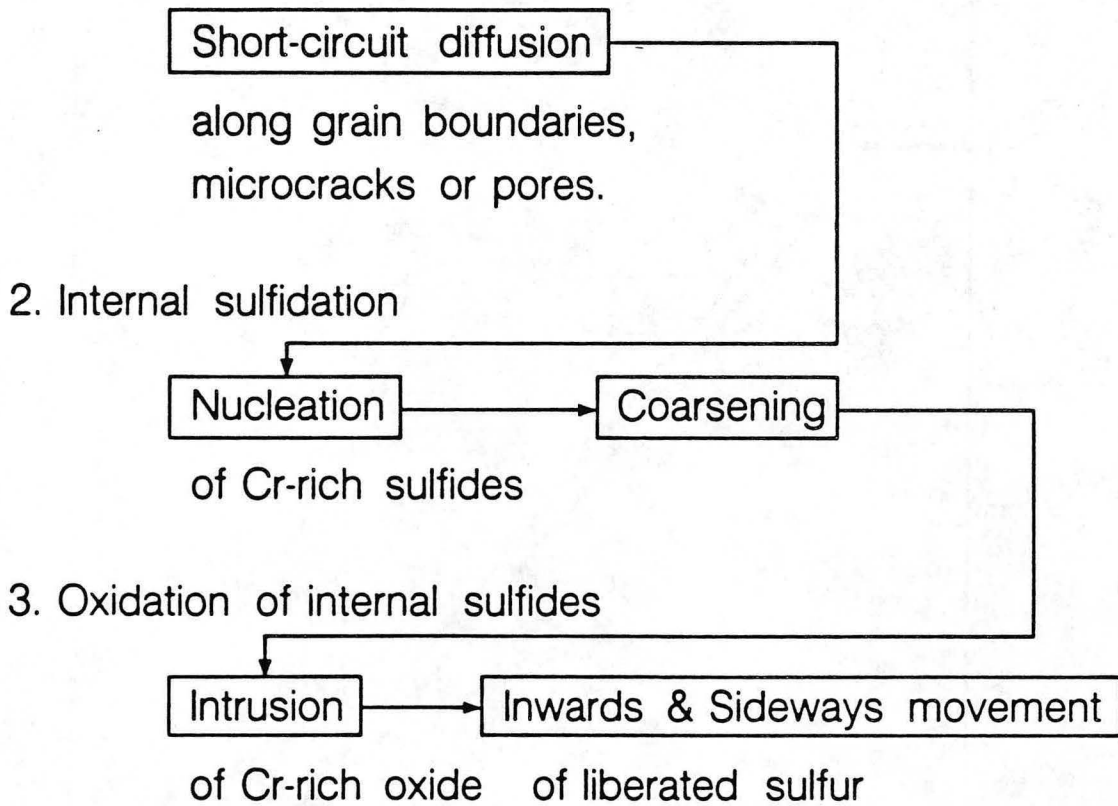
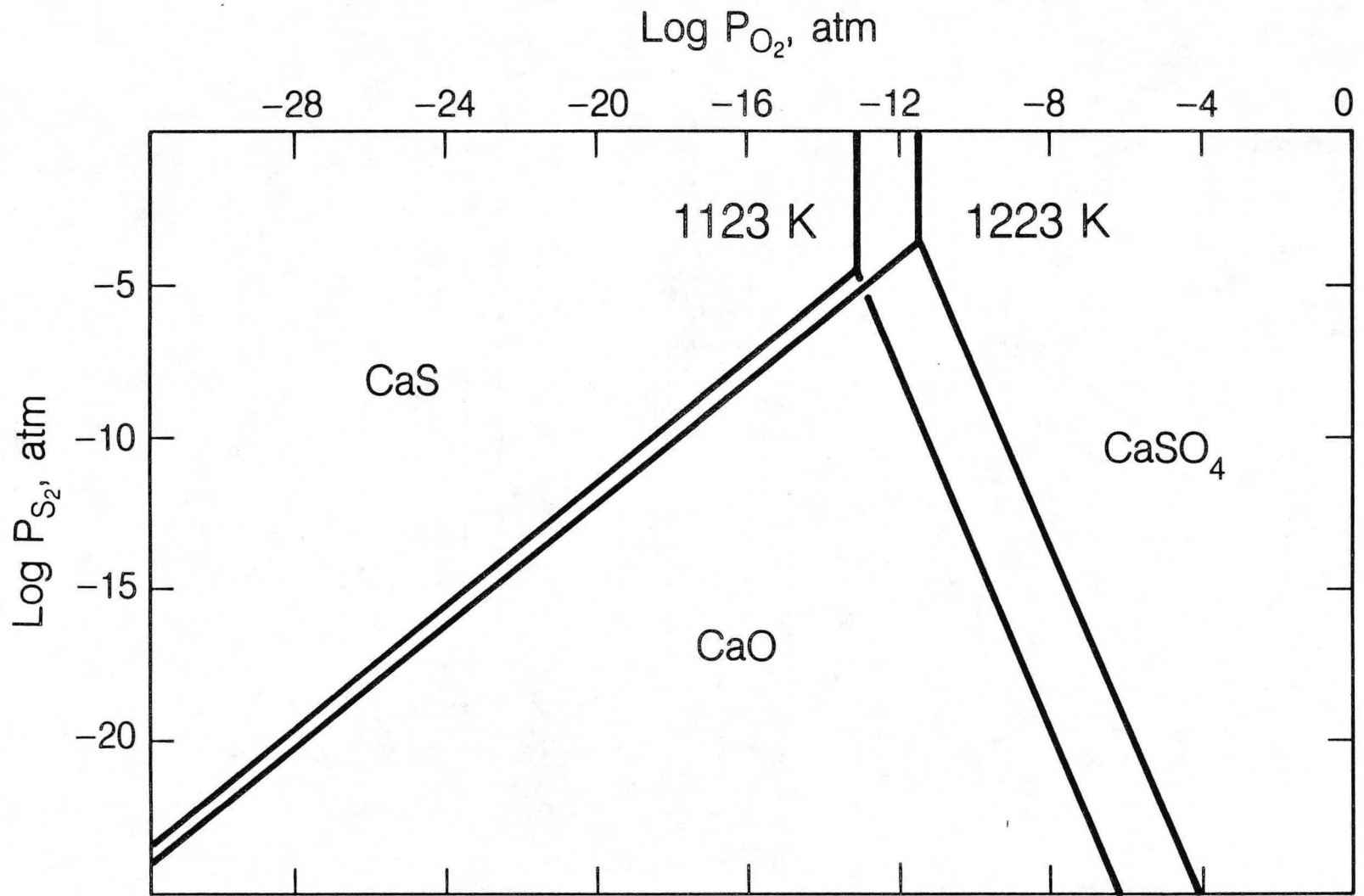


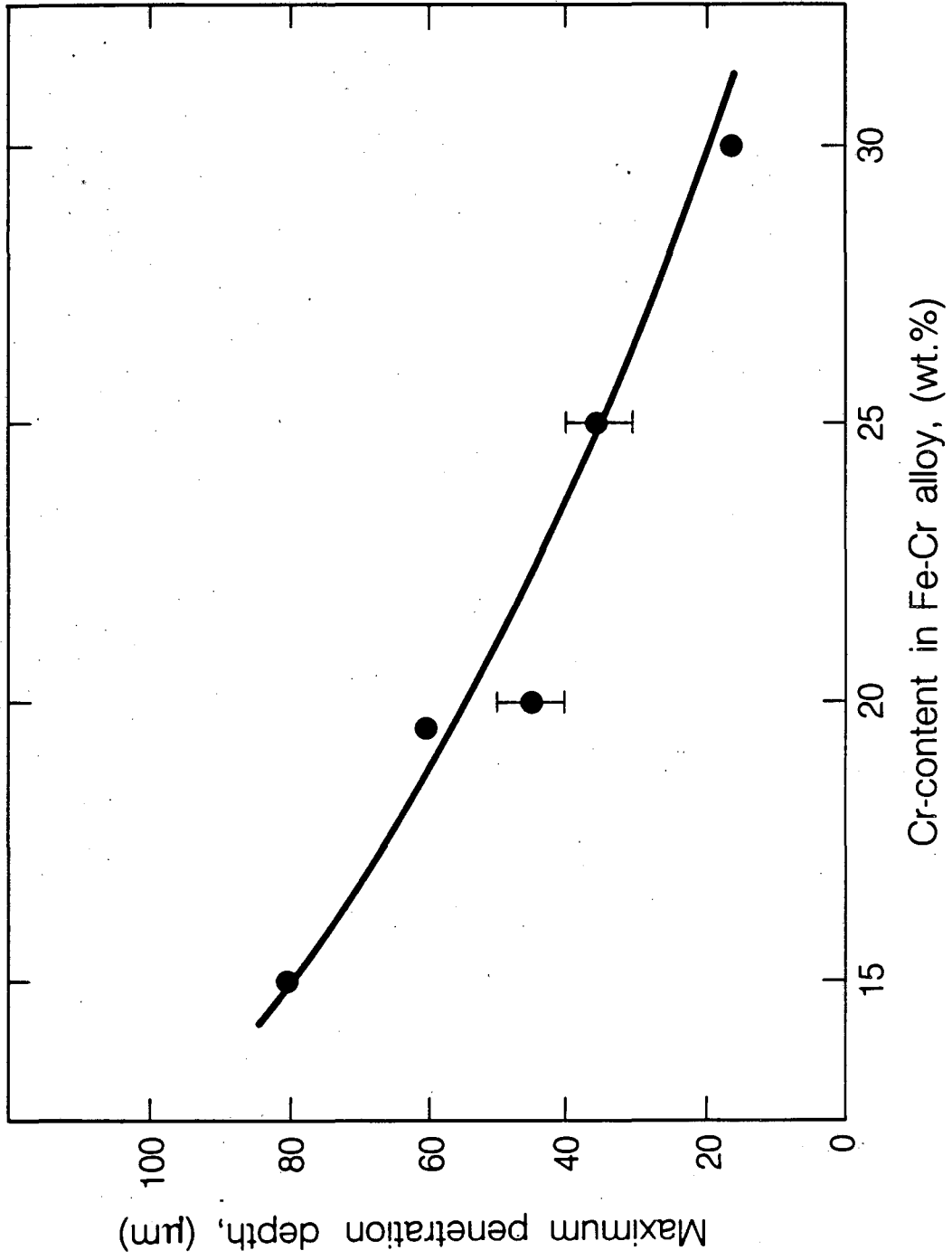
Figure 49.



-160-

Figure 50.

XBL 856-10010



XBL 856-10011

Figure 51.

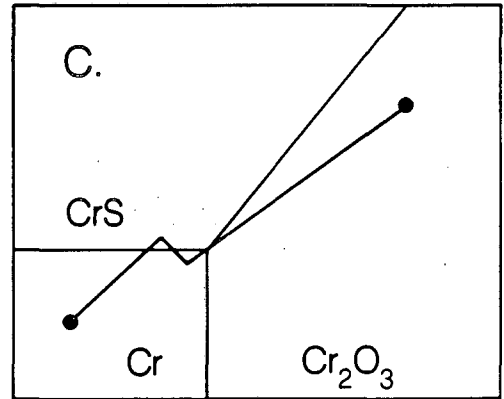
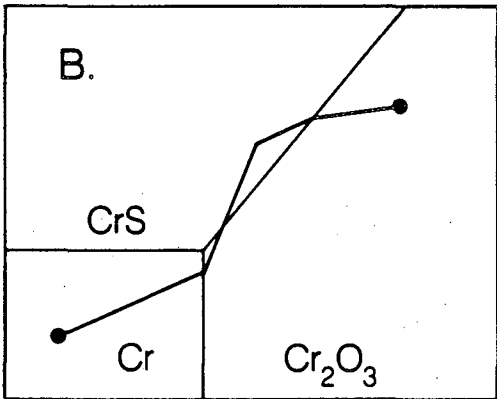
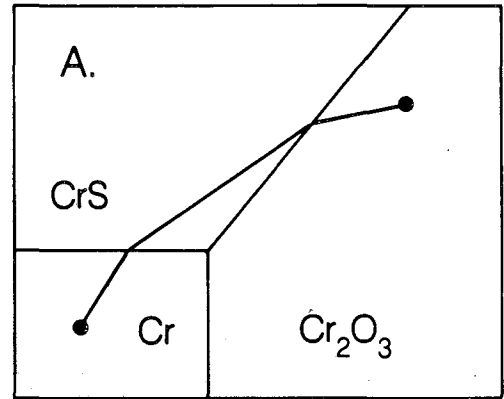
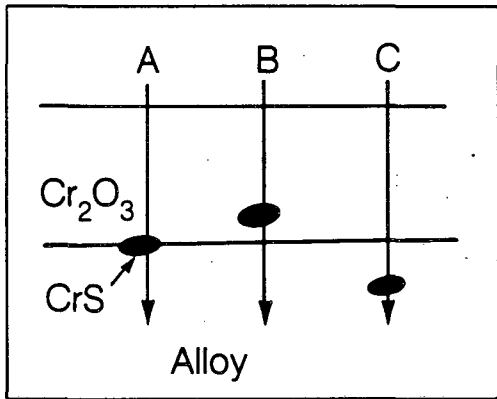
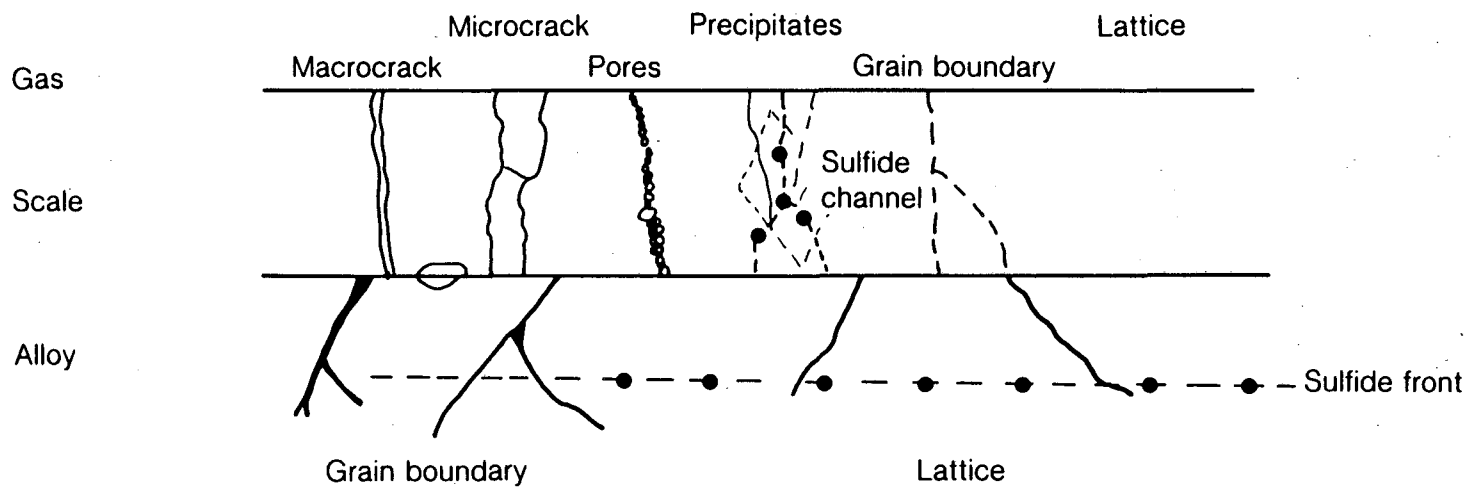


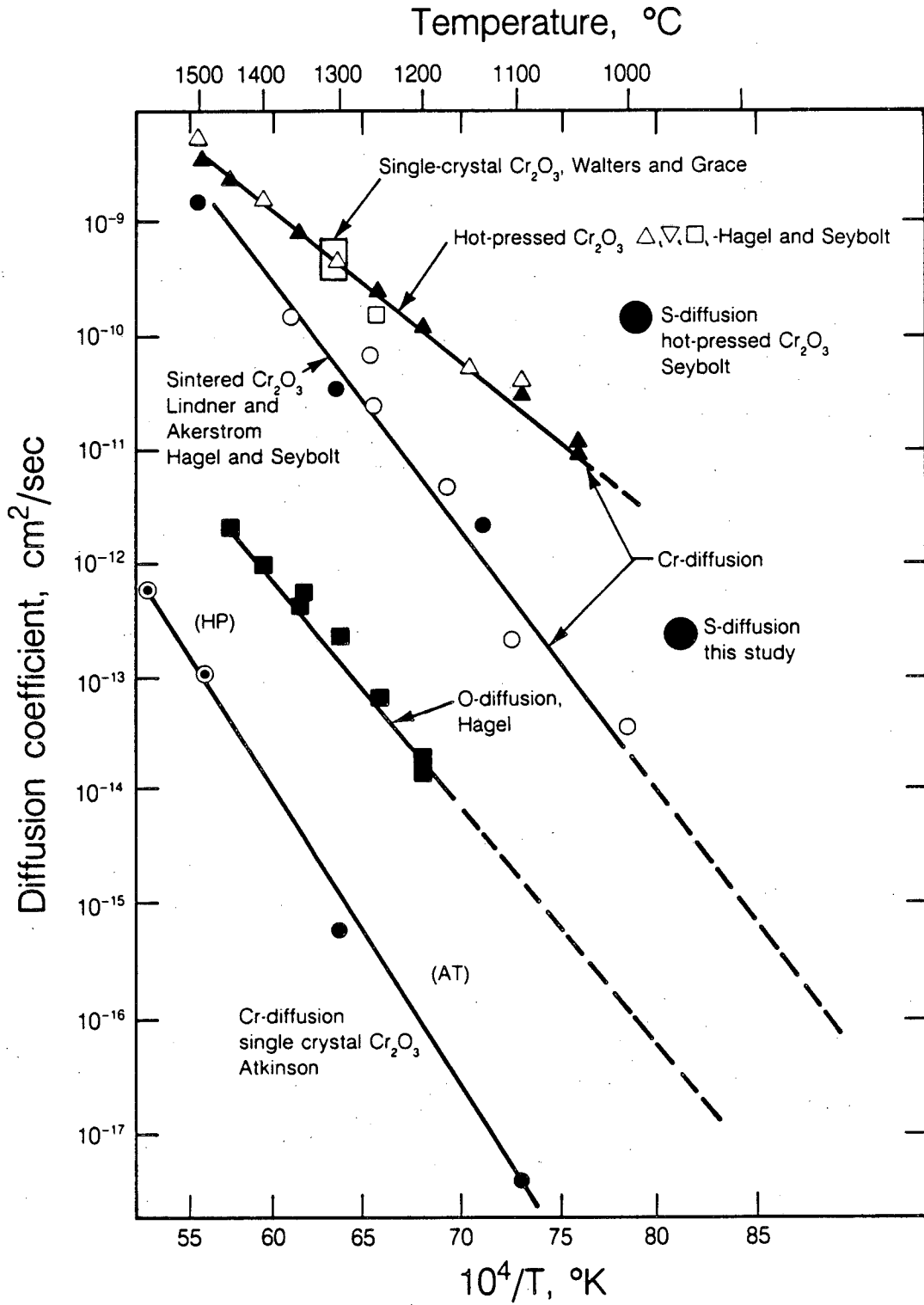
Figure 52.

XBL 856-10027



XBL 856-10029

Figure 53.



XBL 856-10025

Figure 54.

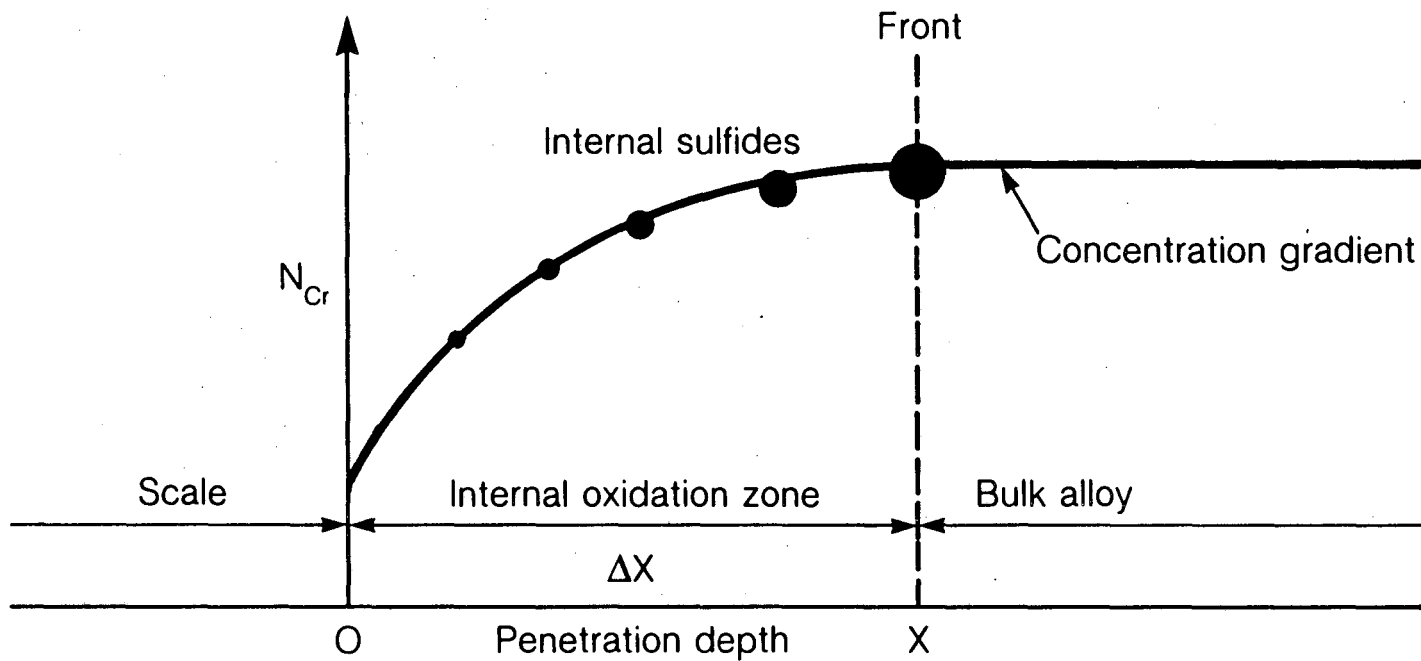
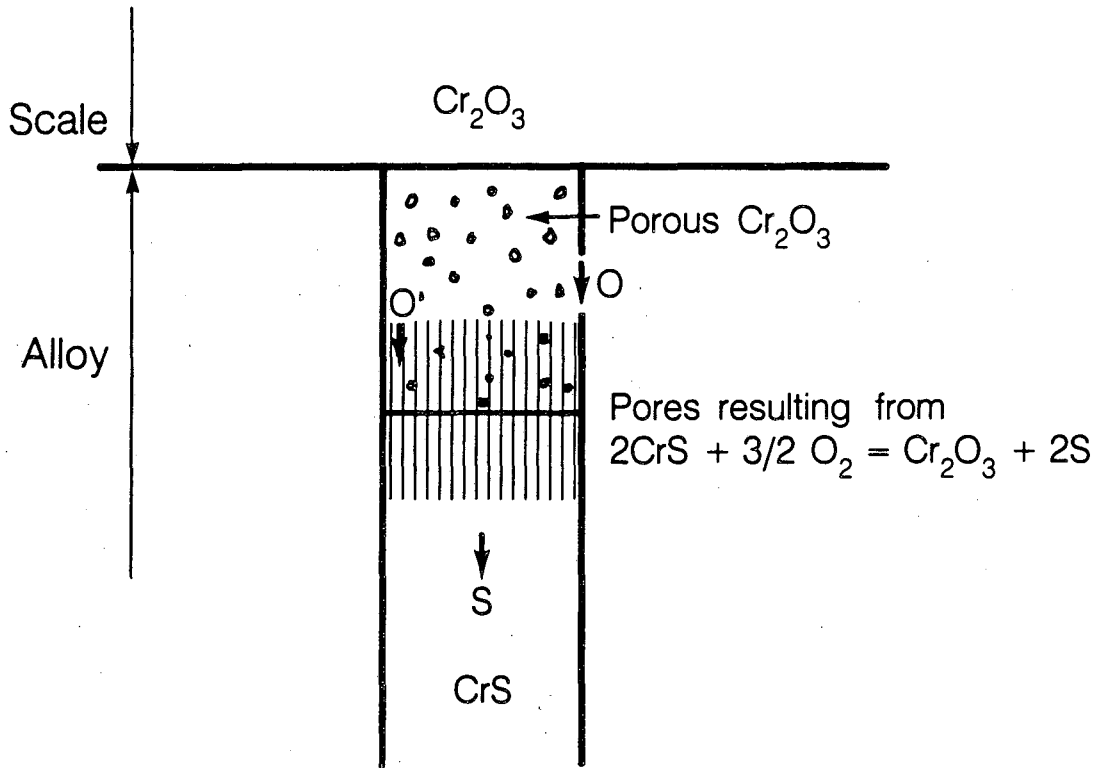


Figure 55.

XBL 856-10009

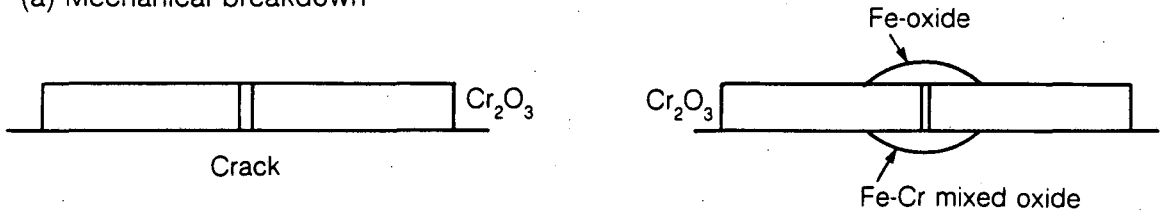


XBL 856-10030

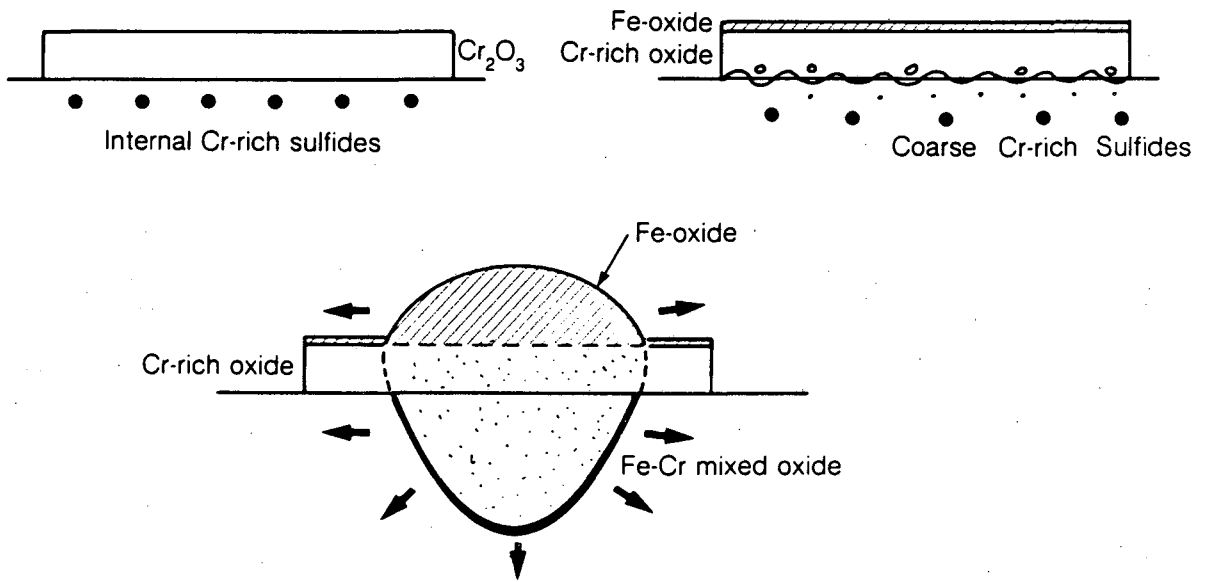
Figure 56.



(a) Mechanical breakdown



(b) Chemical breakdown



XBL 856-10028

Figure 57.

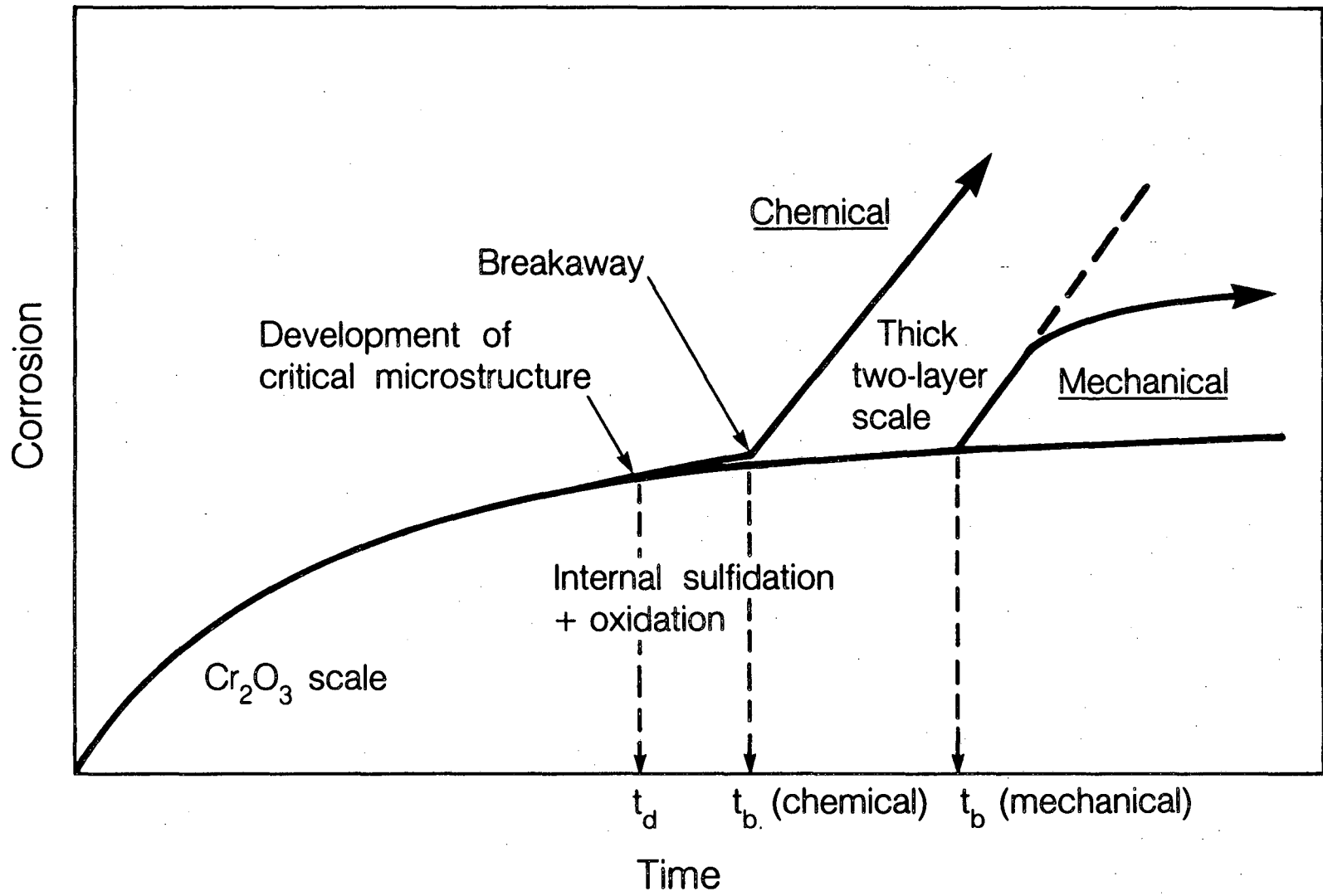


Figure 58a.

XBL 856-10008

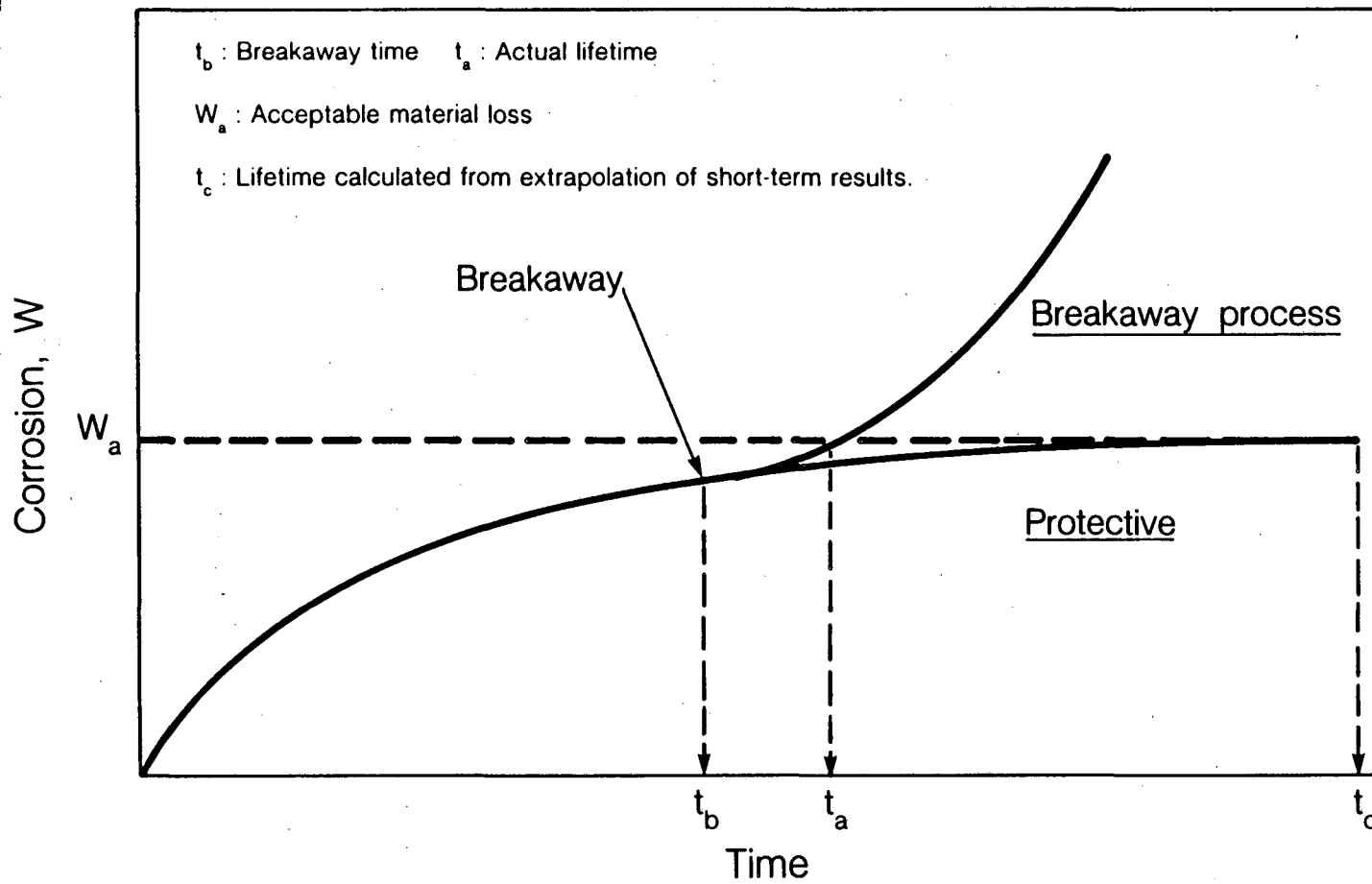


Figure 58b.

XBL 856-10007

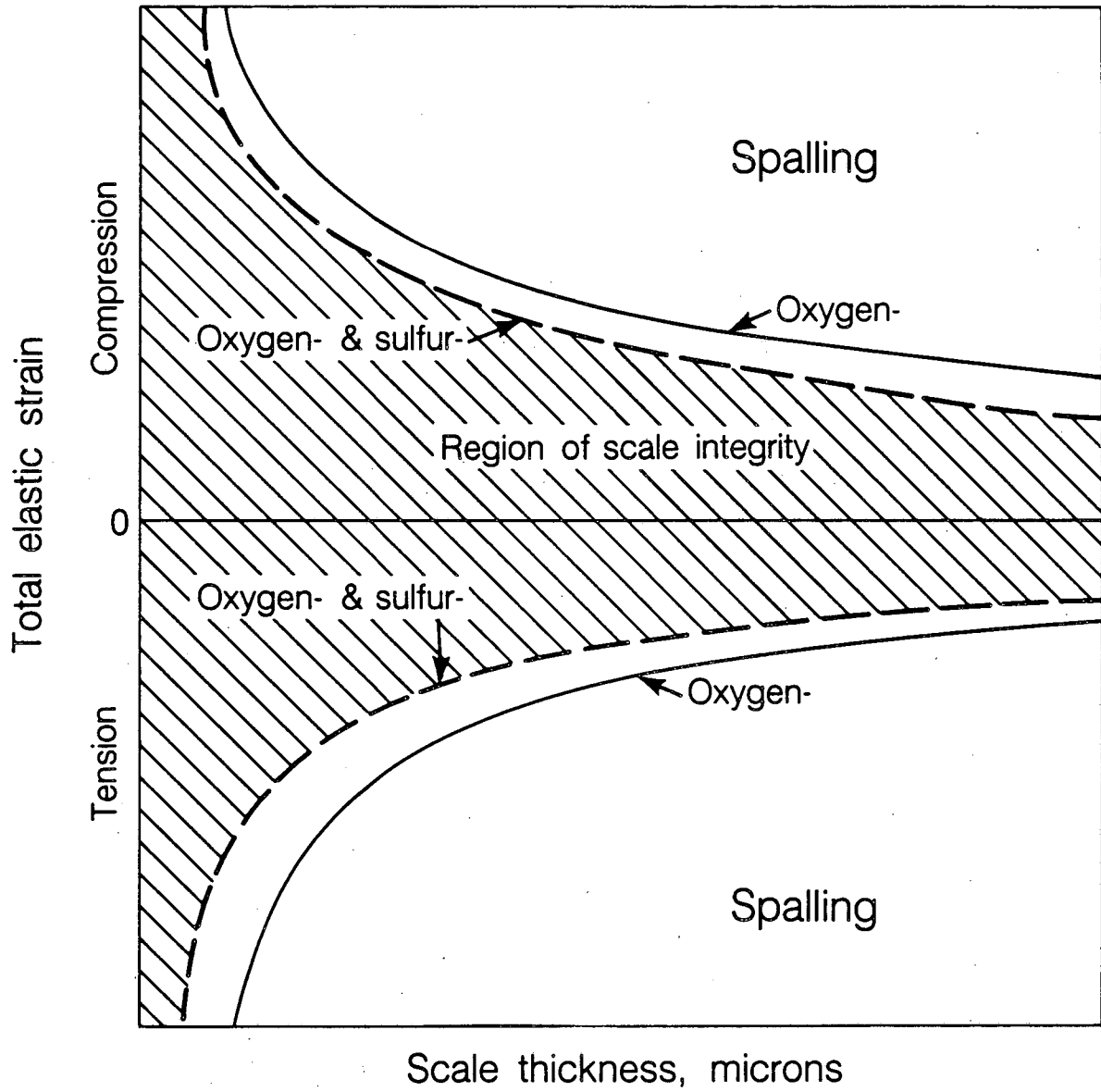


Figure 59.

XBL 856-10026

This report was done with support from the Department of Energy. Any conclusions or opinions expressed in this report represent solely those of the author(s) and not necessarily those of The Regents of the University of California, the Lawrence Berkeley Laboratory or the Department of Energy.

Reference to a company or product name does not imply approval or recommendation of the product by the University of California or the U.S. Department of Energy to the exclusion of others that may be suitable.

*LAWRENCE BERKELEY LABORATORY  
TECHNICAL INFORMATION DEPARTMENT  
UNIVERSITY OF CALIFORNIA  
BERKELEY, CALIFORNIA 94720*